Scholars' Mine

Masters Theses

Student Theses and Dissertations

Fall 2011

Calcium wire ladle treatment to improve cleanliness of centrifugal cast steel

Edith Yolanda Martinez Silva

Follow this and additional works at: https://scholarsmine.mst.edu/masters_theses

Part of the Metallurgy Commons

Department:

Recommended Citation

Martinez Silva, Edith Yolanda, "Calcium wire ladle treatment to improve cleanliness of centrifugal cast steel" (2011). *Masters Theses*. 5125.
https://scholarsmine.mst.edu/masters_theses/5125

This thesis is brought to you by Scholars' Mine, a service of the Missouri S&T Library and Learning Resources. This work is protected by U. S. Copyright Law. Unauthorized use including reproduction for redistribution requires the permission of the copyright holder. For more information, please contact scholarsmine@mst.edu.

CALCIUM WIRE LADLE TREATMENT TO IMPROVE CLEANLINESS OF CENTRIFUGAL CAST STEEL

by

EDITH YOLANDA MARTINEZ SILVA

A THESIS

Presented to the Graduate Faculty of the

MISSOURI UNIVERSITY OF SCIENCE AND TECHNOLOGY

In Partial Fulfillment of the Requirements for the Degree

MASTER OF SCIENCE IN METALLURGICAL ENGINEERING

2011

Approved by

Kent D. Peaslee, Advisor
Von L. Richards
Simon Lekakh

© 2011

EDITH YOLANDA MARTINEZ SILVA

ALL RIGHTS RESERVED

ABSTRACT

Centrifugal casting provides the opportunity of combining large centrifugal forces and directional solidification to reduce non-metallic inclusions in the cast steel product. Calcium treatment in the ladle has the potential of reducing and modifying non-metallic inclusions to achieve better machinability and mechanical properties. The objective of this research is to analyze the combined effects of calcium wire ladle treatment and centrifugal casting on the number, size, composition and morphology of non-metallic inclusions in centrifugally cast steel products.

All experiments were completed at an industrial foundry. The experiments involved feeding calcium wire into the ladle after argon oxygen decarburization (AOD) and prior to centrifugal casting. Samples were collected throughout the ladle treatment process and from the centrifugally cast products. Inclusions analysis was performed using an ASPEX automated inclusion analyzer. Charpy impact testing was performed after heat treatment to evaluate the relationship between toughness and non-metallic inclusions on the centrifugally cast products.

It was found that the efficiency of calcium wire fed just prior to casting was slightly higher than calcium fed at earlier stages of the ladle treatment (just after AOD), providing better *Ca*- reactions with the melt. Alumina (Al_2O_3) inclusions were transformed into low melting point calcium aluminates ($12CaO{\bullet}7Al_2O_3$ and $CaO{\bullet}Al_2O_3$), but the cleanliness of the centrifugally cast products depended more on the centrifugal forces applied to the system than on the calcium wire ladle treatment.

ACKNOWLEDGMENTS

I would like to express my immense gratitude to Dr. Kent Peaslee who provided me with the privilege of pursuing my master’s degree in Metallurgical Engineering at Missouri University of Science and Technology. Dr. Kent Peaslee was very helpful and offered invaluable assistance to develop a full understanding of the subject. I would also like to thank my committee members, Dr. Simon Lekakh and Dr. Von Richards for sharing their knowledge and expertise in this research.

I am also deeply grateful to Dr. Lifeng Zhang for his own simulation study of centrifugal casting, which helped me gain a better understanding of this project. I would also like to show my sincere gratitude to Dr. Luis Trueba for his encouragement and support from the initial level of my career.

I acknowledge the support and funding of the U.S. Army Benet Labs, the Steel Founders Society of America and the industrial foundry that participated in this research. I would also like to thank my lab mates Andrew O’ Loughlin, Arpana Murthy, Carlos Castano, Vivek Thapliyal, Wes Everhart, Meghan McGrath, Scott Pisarik, Vintee Singh and many other personnel who made this thesis possible.

Last but not least, I would like to thank my family, especially my parents and siblings, for their endless love, guidance and support throughout the duration of my studies and personal life.

TABLE OF CONTENTS

Page

ABSTRACT ….. iii

ACKNOWLEDGEMENTS ….. iv

LIST OF ILLUSTRATIONS…………………………………………………...... ix

LIST OF TABLES………………………………….……………….……...... xv

SECTION

1. LITERATURE SURVEY………………………..………..……..…........… 1

  1.1. CENTRIFUGAL CASTING TECHNIQUE ……….……….......... 1

  1.2. CASTING DEFECTS IN CENTRIFUGAL CASTING …..............… 5

    1.2.1 Non-metallic Inclusions …... 5

      1.2.1.1. Non-metallic inclusion distribution in centrifugally cast products……………………...…………... 6

      1.2.1.2. Types of non-metallic inclusions ……....……………. 9

      1.2.1.3. Experimental analysis on non-metallic inclusion distribution in centrifugally cast products …............... 11

    1.2.2. Porosity ……………………………………….............. 13

      1.2.2.1. Gas porosity ....…..... 13

      1.2.2.2. Microporosity in cast alloys …................................... 16

      1.2.2.3. Shrinkage porosity in centrifugally cast products 17

  1.3. CALCIUM WIRE INJECTION IN MOLTEN STEEL …..…........... 17

    1.3.1. Method of *Ca*- Addition ….. 17

    1.3.2. Calcium Wire Ladle Treatment ………………..……......... 18

    1.3.3. Effect of Calcium Treatment on Non-metallic Inclusions…..... 19

1.3.4. Effect of Calcium Treatment on Mechanical Properties……..... 21

1.4. EFFECTIVENESS OF INCLUSION MODIFICATION BY CALCIUM WIRE LADLE TREATMENT ……………….……...... 23

1.4.1. Inclusion Modification with Respect to Time………........... 23

1.4.2. Inclusion Modification with Different *Ca* Amounts and Injection Speeds……………………………………………....... 24

1.5. OUTLINE OF THE PROJECT...…..... 25

2. EXPERIMENTAL PROCEDURE…..…..………………..….....................… 27

2.1. MELTING PROCEDURE...… 27

2.1.1. Regular Practice...…..... 28

2.1.2. Calcium Wire Ladle Treatment……………...…...……...….. 28

2.1.2.1. Calcium wire ladle treatment prior to casting……....... 30

2.1.2.2. Calcium wire ladle treatment after AOD…..................30

2.2. SAMPLING AND OXYGEN MEASUREMENT.............................. 30

2.3. INCLUSION ANALYSIS.. 32

2.3.1. Background of ASPEX Analysis…... 32

2.3.2. User-Defined Rules for Inclusion Statistical Analysis…….… 32

2.3.3. User-Defined Rules for Micro-defect Identification…............ 34

2.4. CHARPY IMPACT TESTING AND FRACTOGRAPHY ANALYSIS…………………………………………………….…... 36

3. EXPERIMENTAL RESULTS……………………………………..…..... 37

3.1. NON-METALLIC INCLUSION ANALYSIS FROM AOD TO CENTRIFUGAL CASTING……………………………………...... 37

3.2. NON-METALLIC INCLUSION DISTRIBUTION IN CENTRIFUGALLY CAST STEEL PRODUCTS…..........................40

3.2.1. Oxide and Sulfide Distribution in Centrifugally Cast Steel Products……………………………..............................43

3.2.2. Distribution of Inclusions Containing Nitrogen in Centrifugally Cast Steel Products …………….….……..…. 47

3.3. NON-METALLIC INCLUSION SPACING IN CENTRIFUGALLY CAST STEEL PRODUCTS………................. 49

3.4. POROSITY IN CENTRIFUGALLY CAST STEEL SAMPLES…... 51

3.4.1. Interdendritic Porosity in Centrifugally Cast Steel Products..... 51

3.4.2. Shrinkage Porosity in Centrifugally Cast Steel Products…...... 53

3.5. MICROSTRUCTURES IN CENTRIFUGALLY CAST STEEL PRODUCTS………………………..…………………….….. 57

3.6. CHARPY IMPACT TESTING……………………………....... 58

3.7. FRACTOGRAPHY…………………….….……………...... 59

4. DISCUSSION…………………………………………….………….…........... 66

4.1. EFFECTIVENESS OF CALCIUM RETENTION IN LIQUID STEEL……………………………………………………….... 66

4.2. THERMODYNAMICS OF CALCIUM WIRE LADLE TREATMENT...…69

4.3. THERMODYNAMICS OF γ-ALUMINUM OXYNITRIDE (Al_7O_9N AND $Al_{23}O_{27}N_5$)….. 70

4.4. NON-METALLIC INCLUSION FLOTATION AND ENTRAPMENT USING DIFFERENT MODELS FOR CENTRIFUGAL CASTING ………………………….……......…73

4.5. COMPARISON OF NON-METALLIC INCLUSION DISTRIBUTION IN STATIC AND CENTRIFUGAL CASTING.... 78

5. CONCLUSIONS…………………………..……………….………..… 82

APPENDIX……………………………………………………….…...…….… 83

BIBLIOGRAPHY…………………….……………………………….……….... 84

VITA………………………………….……………………………………...….. 88

LIST OF ILLUSTRATIONS

Figure Page

1.1. A schematic illustration of a horizontal centrifugal casting machine………………… 2

1.2. Water model experiments of mold filling indicating a) liquid dropping from the top to the bottom of the mold at low rotation speed (305 rpm) and b) a thin and uniform liquid film that is picked up by the mold surface friction at high rotation speeds (600 rpm) during horizontal centrifugal casting…………………………...... 3

1.3. Schematic diagram illustrating the theoretical change in variable speed during centrifugal casting, especially for centrifugally cast steel products ………….......... 4

1.4. Schematic force diagram showing the centrifugal and gravitational forces in the centrifugal cast product…......……………………………………….………....... 6

1.5. A schematic illustration showing a) the inclusion flotation towards the ID at the early stages of the solidification process and b) the particle pushing effect after the formation of a coherent solidification front ………..……………….……..... 9

1.6. Comparison and classification of inclusion distribution (>10μm) in low alloy steel castings using a total sample of 500 inclusions from 14 foundries in the U.S.. 10

1.7. Average inclusion area (μm^2) in the radial direction of the centrifugally cast *CrMo* steel pipe showing inclusion distribution from the outside (3 mm) to the inside region (40.5 mm)…………………………………………….………...... 11

1.8. a) Fine precipitates are irregular in shape and size in a matrix of ferrite and pearlite at the outside diameter (1-3 mm) of the centrifugally cast tube, b) A more disperse microstructure is observed in a matrix of ferrite and pearlite at the inside diameter (17-23 mm) of the centrifugally cast tube……………………….....… 12

1.9. Area covered (S_{ni}) by non-metallic inclusions from the outside (*h*=0 mm) to the inside diameter (*h*=45 mm) of the centrifugally cast 15kh1M1F steel product ...… 13

1.10. Non-metallic inclusion distribution along the length of the centrifugally cast steel product (Z=0 m= pouring end; Z=5 m= opposite pouring end) based on the standard scale of inclusion analysis (GOST 1778-70)…......…………….……..….. 13

1.11. Relationship between the contact angle of a bubble against a solid substrate and critical pressure showing the changes of a solid substrate from wetting (θ= 0) to non-wetting (θ= 180)...……………..…...……………………………..... 15

1.12. Schematic illustration of the typical calcium injection method……......………..... 18

1.13. The binary phase diagram of CaO- Al_2O_3 ………….……………...……..…….... 20

1.14. Percentage reduction area, percentage elongation and izod impact of 0.20% *C* steel castings after aluminum deoxidation (a, b and c)….……………………........ 22

1.15. Comparison of mechanical properties of 0.20 %*C* cast steel treated with *Al* followed by CaSiBaAl wire injection…..…………..……..…………………....… 22

1.16. SEM-mappings showing a combination of a high melting point inclusion (*MgO*) in the center and a low melting point inclusion with high calcium content at the outer surface…………………………………………………...... 23

1.17. The base case heat with no calcium treatment showing re-oxidation from tapping after aluminum and *Fe70Ti* additions to the final casting……………...… 25

1.18. Calcium injection experiments with different additions and injection speeds showing better inclusion modification with increased *CaSi*-addition…..……..…. 25

2.1. P.C. Campana micro-wire feeder used in heats B, C, D and E during the calcium wire ladle treatment…………………...………………………...……………… 29

2.2. Schematic representation of the cast tube sample taken from the end of the finished tube showing the location from the inside to the outside of the cast product…...… 31

2.3. Identification of an inclusion by the BSED detector followed by the centering and drawing of chords to determine the size and shape of an inclusion…..……....... 33

2.4. Automated feature analysis (AFA) showing the sub-division of the left SEM image into fields, as well as the identification of a bright particle and its elemental composition by x-ray spectroscopy……..……………………….……..... 33

3.1. Comparison of the a) percentage area covered by inclusions and b) the total oxygen measured in samples collected from the AOD to the final product for each experimental heat……………………………………...…..…………….…….…38

3.2. Percentage area covered by inclusions at different locations in the cast tube samples taken from the opposite pouring end of the finished tubes for each experimental heat…….……………………………………………………….... 41

3.3. Average a) percentage area covered by inclusions and b) total oxygen from the OD to the ID of the centrifugally cast products for each experimental heat……....... 43

3.4. Average a) percentage area covered by oxides and sulfides and b) total oxygen from the OD to the ID of the centrifugally cast products for the five heats............…44

3.5. Average inclusion size distribution including the ID, OD and the final product for each experimental heat………………………………......…....……..…….. 45

3.6. Average inclusion diameter of a) oxides and b) sulfides in the centrifugally cast products for each experimental heat………………...…………...…………..... 45

3.7. Average inclusion aspect ratio using different inclusion compositions from the OD towards the ID of the centrifugally cast products for each experimental heat……….………………………………………………………………...…… 47

3.8. Average inclusion aspect ratio from the OD towards the ID of the centrifugally cast products for each experimental heat……………..……………...……………… 47

3.9. Total nitrogen measured in samples collected from the AOD to the final product for each experimental heat……...……………………………………………………48

3.10. Percentage area covered by inclusions containing nitrogen and others in the final product of the centrifugally cast products for each experimental heat………..…… 49

3.11. Average inclusion diameter of complex inclusions containing nitrogen (oxynitrides) in the centrifugally cast products for each experimental heat…......... 49

3.12. Average inclusion spacing in the centrifugally cast steel products for each experimental heat……………………………………….……………….....….. 50

3.13. Comparison of a) the average percentage area covered by inclusions and b) the average inclusion spacing in the centrifugally cast steel products for each experimental heat……………………………………….………….……........ 51

3.14. Aspex/ SEM image showing the typical morphology of porosity at x=0.25 in the final product of the centrifugally cast samples ……….………….…….…..... 52

3.15. Average percentage area covered by porosity in the centrifugally cast products for each experimental heat…………………….……….....……….…....... 53

3.16. Average porosity diameter in the centrifugally cast products for each experimental heat……………………………………….………………........ 53

3.17. Average aspect ratio of porosity in the centrifugally cast products for each experimental heat……...…………………………….….…………….…… 54

3.18. Stereographs of the ID (X=0) of the centrifugally cast products showing visible porosity for a) the base heat A and calcium treated heats b) B, c) C, d) D and E in the un-etched condition…………………………...……….. 54

3.19. Micrographs of the ID (X=0) in the centrifugally cast products showing visible porosity for the calcium treated heats a) D and b) E…………………...…. 55

3.20. Aspex SEM image of the ID (X=0) in the centrifugally cast products revealing shrinkage porosity for a) the base heat A (2500X) and calcium treated heats b) B (100X), c) C (75X), d) D (100X) and e) E (220X) ………...… 56

3.21. Micrographs of the OD (X=1) in the centrifugally cast steel for heats a) B and b) C showing lath martensite.…………………………………….....……….. 57

3.22. Micrographs of the OD (X=1) in the centrifugally cast products for heats a) A and b) D showing tempered martensite after heat treatment………..…………….…. 57

3.23. Charpy impact energy absorbed at room temperature for the base heat A and calcium treated heats B, C, D and E…………………...…………………......… 58

3.24. Fracture surface of the final product (X=0.5) of the centrifugally cast steel tube from Heat B (0.014 %Ca) revealing that the fracture in this alloy occurs almost completely by microvoid coalescence, but close examination shows a few areas of intergranular fracture and complex inclusions (Al_2O_3-AlN, MnO-Al_2O_3, CaO-Al_2O_3-AlN) a) 45X b) 9500X ……………………………………………..…..... 60

3.25. Fracture surface of the final product (X=0.5) of the centrifugally cast steel tube from Heat B (0.014 *%Ca*) showing Al_2O_3 and Al_2O_3-MnS clusters at 4000X…..… 61

3.26. Fracture surface of the final product (X=0.5) of the centrifugally cast steel tube from Heat B (0.014 *%Ca*) showing inclusions in a ductile dimple fracture a) 1500X b) 3000X……………………………………………………….……... 61

3.27. Fracture surface of the final product (X=0.5) of the centrifugally cast steel tube from Heat B (0.014 *%Ca*) revealing the chemical composition of inclusions (MnO, MnS and Al_2O_3) in a ductile dimple fracture at 3000X…………….….….. 62

3.28. Fracture surface of the final product (X=0.5) of the centrifugally cast steel tube from Heat B (0.014 *%Ca*) exhibiting porosity and equiaxed dimples at 300X..…. 62

3.29. Centrifugally cast steel sample from the final product (X=0.5) of Heat E (0.139 *%Ca*) revealing the chemical composition of non-metallic inclusions (Al_2O_3-MnS, Al_2O_3) in a steel matrix……………….…………………….…...… 63

3.30. Centrifugally cast steel sample from the final product (X=0.5) of Heat E (0.139 *%Ca*) showing inclusion clusters in a steel matrix………………...……... 63

3.31. Centrifugally cast steel sample from the final product (X=0.5) of Heat E (0.139 *%Ca*) revealing MgO-Al_2O_3 and Al_2O_3-MnS inclusions in a steel matrix... 64

3.32. Centrifugally cast steel sample from the final product (X=0.5) of Heat E (0.139 %*Ca*) exhibiting a ring of $MgO\text{-}Al_2O_3$ inclusions in the former boundary of a bubble- shaped cavity……………………..……………….……... 64

3.33. Centrifugally cast steel sample from the final product (X=0.5) of Heat E (0.139 %*Ca*) revealing $MgO\text{-}Al_2O_3$ and Al_2O_3 inclusions around the boundaries of a cavity in a steel matrix……………………………..……….………….... 65

4.1. The variation of the boiling point of calcium with a) the external pressure and b) the depth of the wire in the molten steel…….……....…………………………….…… 68

4.2. Thermodynamic analysis showing the relationship between %*Ca* and the calcium-modified inclusions (Liquid *Ca-Al-O-S*, *CaO* and *CaS*) under different boundary conditions (open and isolated top) at 2912° F (1600° C) ………………. 70

4.3. Equilibrium ($[O]=[O]_{eq.}$) and unsaturated ($[O] < [O]_{eq.}$) relations between [%*Al*] and [%*N*] at which *AlN* and Alon (Al_7O_9N and $Al_{23}O_{27}N_5$) are formed at 1873 ºK.... 72

4.4. Equilibrium ($[O]=[O]_{eq.}$) and unsaturated ($[O] < [O]_{eq.}$) relations between [%*Al*] and [%*N*] at which Alon (Al_7O_9N and $Al_{23}O_{27}N_5$) is formed at 1873 ºK …….……. 73

4.5. Solidification kinetics in a centrifugally cast tube using a wall thickness of 4 in (0.1 m)…………………………….…………..…………………………...….. 74

4.6. Effect of the apparent viscosity (μ=0.005 kg/m*s without solid fraction; μ_{ap}=0.05 kg/m*s with 25-30% solid fraction) on flotation dynamics using an inclusion diameter of 5µm at 100*G*….……………………………………………….……….. 75

4.7. Comparison of a) the air-steel interface during pouring and b) the temperature distribution at 19 s after pouring, using the three-dimensional CFD computation.... 78

4.8. Comparison of inclusion final entrapment using particle size diameters between a) 5 µm and b) 50 µm in the solidified centrifugal tube at a rotation speed of 850 rpm, using the two-dimensional CFD computation …………………………... 78

4.9. Comparison of the area covered by inclusions in samples taken from the cast keel blocks in sand casting and the final product of the centrifugally cast steel products with different amounts and speeds of calcium wire injection in the ladle... 79

4.10. Comparison of the inclusion spacing in samples taken from the cast keel blocks in sand casting and the final product of the centrifugally cast steel products with different amounts and speeds of calcium wire injection in the ladle……....... 80

4.11. Comparison of porosity in samples taken from both the cast and HIPed Eglin steel (ES-1) in static casting, as well as the final product of the centrifugally cast steel products with different amounts and speeds of calcium wire injection in the ladle…………………………………………………………..…. 81

LIST OF TABLES

Table Page

1.1 Chemical composition of steel held for 30, 60, 90 and 180 minutes with no stirring at 2910°F (1600°C)……….. 24

1.2 Modification of inclusion morphology with respect to calcium reaction time…....… 24

2.1 Chemical composition after final additions in AOD for each heat in wt%................ 28

2.2 Calcium injection parameters for each experimental heat……………….………....… 29

2.3 Centrifugal casting parameters for each experimental heat, as provided by the participating industry foundry ……………………………………………….......... 30

2.4 Classification rule for oxide, sulfide and micro-defect (porosity) analysis on the lollipops and centrifugally cast steel specimens ……………………….….….…….... 35

2.5 Zero rules for oxide, sulfide and micro-defect (porosity) analysis on the lollipops and centrifugally cast steel specimens ………………….……...…...……...… 35

2.6. Classification rule for oxide, sulfide, porosity and oxynitride analysis on the centrifugally cast steel specimens.. 35

2.7. Zero rules for oxide, sulfide, porosity and oxynitride analysis on the centrifugally cast steel specimens... 36

4.1 Temperature prior to *Ca*-wire ladle treatment and efficiency factor (E_r) of calcium retention for each experimental heat…………………………………………….….....68

4.2. Thermodynamic parameters of aluminum and nitrogen in liquid iron at 1873 ºK.….72

4.3. Dimensions and parameters for CFD modeling…………………………......…... 76

1. LITERATURE SURVEY

New applications for centrifugally cast low alloy steels have been proposed due to the improved steel cleanliness and superior mechanical properties from the centrifugal casting process. Centrifugally cast near net shape preforms that are sufficiently free from defects have the potential of replacing forged preforms for applications such as cannons, reducing the manufacturing cost by eliminating many steps to produce the near net shaped product. However, centrifugally cast preforms would need to be equivalent or better in properties to the forged product. One primary defect reducing properties of steel castings is non-metallic inclusions formed during steelmaking, ladle treatment, pouring and solidification. Non-metallic inclusions degrade the quality or “cleanliness” of the cast steel based on the volume, size and distribution in the casting, as well as shape and type of morphology. Therefore, for centrifugally cast low alloy steels to be accepted in more critical applications, micro-defects such as inclusions and micro-porosity must be controlled and minimized to result in the required quality for the final product. The purpose of this thesis is to investigate the effects of calcium treatment on the cleanliness of centrifugally cast products.

1.1. CENTRIFUGAL CASTING TECHNIQUE

Centrifugal casting is used to manufacture highly engineering castings, turbine blades, dental parts, fittings, mass production pipes and tubes [1]. The critical step in centrifugal casting involves pouring liquid metal into a rotating mold and continuing rotation until solidification is achieved [2]. The rotating mold tends to deform under high temperatures and mechanical stresses during the casting process. In order to minimize mold deformation, a ceramic mold material is centrifugally applied to the permanent mold (metal flask) and preheated to reduce thermal damage [2], [3]. Molten metal is then poured into the mold and an antioxidant flux is used to reduce re-oxidation and promote unidirectional solidification from the outside towards the inside diameter. The heat flux from the inside diameter to the air is very low, producing little heat loss at this location [4]. These conditions along with large centrifugal forces reduce significantly the inclusion and shrinkage formation in the centrifugally cast products [1], [3], [5].

Low alloy steels are typically suitable for horizontal centrifugal casting. Horizontal centrifugal casting is preferred when the length is at least double the inside diameter of the centrifugally cast product [1]. In Figure 1.1, the mold and molten metal rotate rapidly about their central axis along the horizontal plane. Water sprays are typically applied to the outside surface of the mold to cool down the casting during solidification [3].

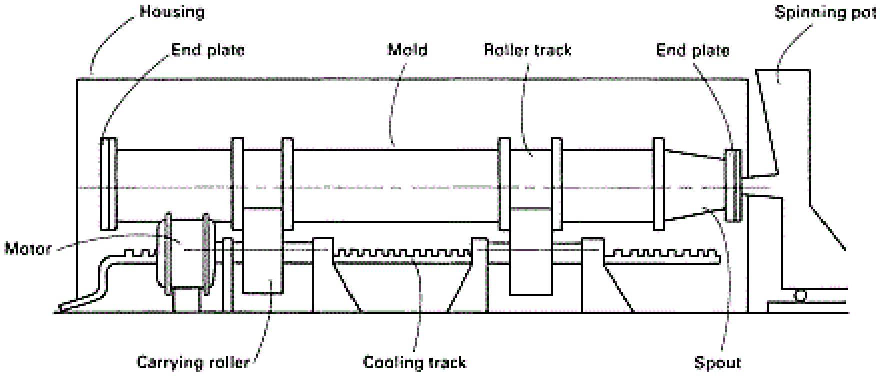

Figure 1.1. A schematic illustration of a horizontal centrifugal casting machine [3]

The quality of the centrifugally cast product is influenced by the pouring temperature, pouring rate, heat transfer coefficient (*h*), and mold rotational speed [5]. A low pouring temperature and rate produce large heat losses in the first molten metal delivered against the mold surface, minimizing the solidification temperature and time of the casting. The first molten metal delivered against the mold circumference during the first revolution may solidify midway, restraining its flow to the end of the mold. The succeeding molten metal will then cover the solidified layer. In the interface of these two layers, inclusions and gasses are trapped in the centrifugally cast product, which can result in hot cracks at these locations. A hot crack is formed in alloys with a large solidification interval that are prone to shrinkage [5]. Hot cracks are reduced by faster pouring rates and a uniform pre-heating of the mold to avoid different cooling rates in centrifugal casting [1], [5].

The heat transfer coefficient (*h*) at the outside diameter is typically larger than at the inside diameter of the centrifugally cast product. When the rate of heat transfer from the outside of the casting to the mold is insufficient, hot cracks are formed due to a coarse solidification structure in the centrifugally cast product. A high mold temperature also leads to longer solidification time, multidirectional solidification and more intense segregation. Segregation degrades the mechanical properties and wear resistance of the cast product [2]. In order to improve heat dissipation, rapid cooling of the mold is required by spraying water on the mold [4].

The mold rotational speed needs to be maintained below a critical point to prevent high tensile stresses at the outside diameter that may produce longitudinal layer cracking. Taylor vortices are produced through a wavy and disturbed flow (Ekmann flow) caused by an extremely high rotational speed and a low viscosity fluid [6]. These vortices create an irregular surface in the centrifugally cast product. The effect of the Ekmann flow can be reduced through larger mold diameters or with an increased length with respect to the mold diameter. In either the small diameter or decreased length case, the rotational speed must be high enough to form a uniform cylindrical layer in the rotating mold [6]. In contrast, a low and inappropriate mold rotational speed causes liquid to drop from the top to the bottom of the mold during the filling process as illustrated in Figure 1.2, creating casting defects in the final product [7].

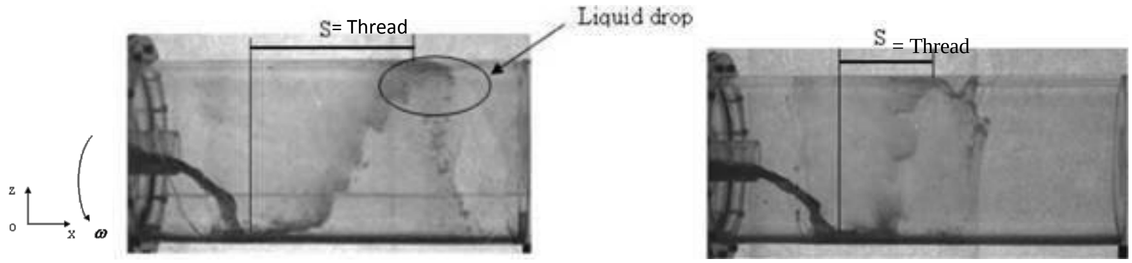

a) b)

Figure 1.2. Water model experiments of mold filling indicating a) liquid dropping from the top to the bottom of the mold at low rotation speed (305 rpm) and b) a thin and uniform liquid film that is picked up by the mold surface friction at high rotation speeds (600 rpm) during horizontal centrifugal casting [7]

The process of varying the rotational speed is often used in centrifugal casting in order to increase the service life of the mold and equipment, as well as to reduce the power consumption and crack formation in the centrifugally cast product. Figure 1.3 shows how a typical centrifugal casting operation would change the rotational speed (n)

and time (t) during casting, with $n_1 > n_3 > n_2 > n_4$ and $t_4 > t >_3 > t_2 > t_1$. The rotational speed at the beginning of the centrifugal casting process, n_1 (960-980 rpm), is high enough to spread the molten metal over the entire mold length to prevent double-skin and cold shut defects [1], [5]. The rotation speed n_1 will lead to a uniform thin layer in the mold [6], [7]. The uniform thin layer is subjected to high pressure, leading to quick solidification of the outside diameter of the centrifugally cast product [7]. However, time t_1 cannot be too long with the mold rotation speed at n_1 due to the fact that a large concentration of centrifugal forces will form cracks in the centrifugally cast product. The rotation speed is then dropped to n_2 (800-820 rpm) to minimize the pressure on the thin solidified casting. Once the solidified thickness is sufficient, the rotation speed is increased to n_3 (800-900 rpm), to improve the formation of the casting and encourage a compact structure. The time t_3 at $n_3$will depend on the strength of the centrifugally cast product to withstand large centrifugal forces without cracking. The final rotation speed, n_4 (720-740 rpm), is reduced to prevent crack formation due to large internal stresses produced by rapid cooling of the casting. After n_4 and t_4, the centrifugal casting machine is stopped. The centrifugally cast product is then removed from the mold to allow further cooling of the casting at a lower rate, reducing the residual stresses in the casting.

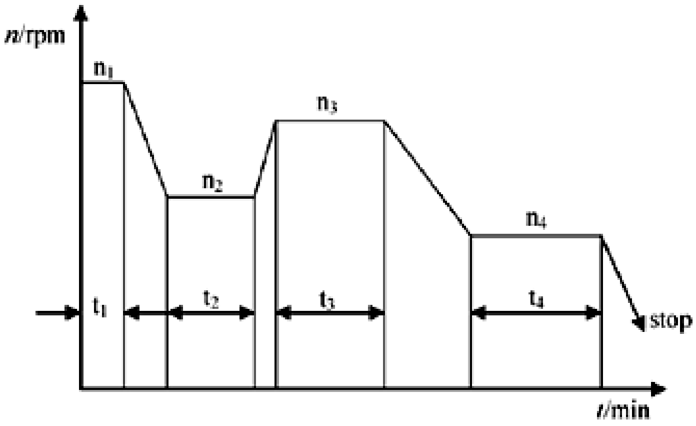

Figure 1.3. Schematic diagram illustrating the theoretical change in variable speed during centrifugal casting, especially for centrifugally cast steel products [5]

Casting removal proceeds after the centrifugal casting process is completed. Some of the methods that are typically used for casting removal involve either pulling the casting out of the mold and later removing the refractory from the mold, or pushing the casting and refractory out of the mold at the same time. Generally, the casting can be easily removed from the mold, but as the life of the mold reaches its end, the casting removal will be progressively more difficult to perform. This is due to the deterioration of the mold surface caused by cracks and localized burned layers, which can be minimized by welding and re-grinding the mold surface [1].

1.2. CASTING DEFECTS IN CENTRIFUGAL CASTING

1.2.1. Non-metallic Inclusions. Non-metallic inclusions have a significant influence on the mechanical properties due to the fact that their thermal expansion coefficients are different in comparison to the surrounding metal, inducing stresses and void nucleation during solidification. Crack propagation is then produced due to the low bond energy of inclusions with the steel matrix [8]. The volume fraction of non-metallic inclusions (v_f) and the spacing between them are related to the fracture toughness of steel (K_{IC}). K_{IC} is the ability of a material to withstand an applied load in the presence of flaws or inclusions as described in Eq. 1 [9],

$$K_{IC} = v_f^{-1/6} \sqrt{2\left(\frac{\pi}{6}\right)^{1/3} \sigma_{yield} E d} \tag{1}$$

where, v_f is the volume fraction of inclusions, σ_{yield} is the applied stress, E is the Young's modulus and d is the inclusion diameter [9].

By using Eq. 1, Hahn et al. determined that the fracture toughness is indirectly proportional to the volume fraction of inclusions in steel [9]. The relationship between fracture toughness and inclusion spacing is given by Eq. 2,

$$K_{IC} = \left(2\sigma_{yield} E s\right)^{1/2} \tag{2}$$

where, s is the average spacing between non-metallic inclusions [9].

V. Singh et al. confirmed that fracture toughness of steel is enhanced by decreasing the volume fraction of inclusions and increasing the spacing between non-metallic inclusions in steel [9].

1.2.1.1. Non-metallic inclusion distribution in centrifugally cast products. The centrifugal forces in the mold are influenced by the gravitational coefficient, *G*, which is typically 75 to 120 times greater than gravity, *g*, forcing molten metal against the spinning surface (Eq. 3) [1].

$$G = \omega^2 r / g \tag{3}$$

where, ω is the angular velocity and *r* is the distance between the rotation axis and a given position in the centrifugally cast product [10].

The movement of a particle, *M*, in centrifugal casting is influenced by two forces, the gravity force (*mg*) and centrifugal force, F_C, as illustrated in Figure 1.4 (Eq. 4) [10],

$$F_C = m\omega^2 r \tag{4}$$

where, *m* is the mass of the particle *M* [10].

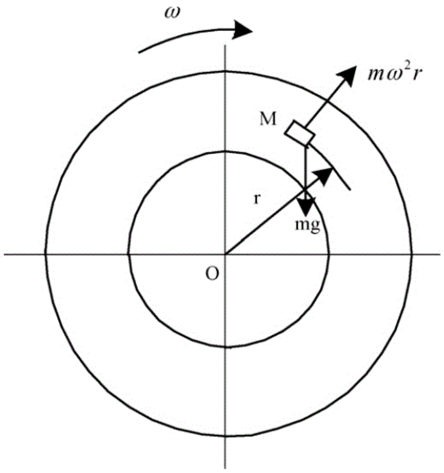

Figure 1.4. Schematic force diagram showing the centrifugal and gravitational forces in the centrifugal cast product [10]

The centrifugal force ($\omega^2 r$) is far greater than the gravitational force, *g*, neglecting the influence of *g* on the particle distribution in the centrifugally cast product. The centrifugal force ($\omega^2 r$) replaces *g* in Stokes law, and the velocity v_M is then expressed by Eq. 5 [11].

$$v_M = \frac{d_M^2(\rho_M - \rho_L)\omega^2 r}{18\eta_L} \tag{5}$$

where, d_M is the diameter of a spherical particle, ρ_M is the particle density, ρ_L is the liquid density and η_L is its dynamic viscosity.

The position *r* influences the motion of each single spherical particle, resulting in different velocities [2], [11]. If $v_M<0$ because $\rho_M<\rho_L$, the particle will move to the inside diameter of the centrifugally cast product. If $v_M>0$ because $\rho_M>\rho_L$, the particle will move to the outside diameter of the centrifugally cast product [10].

Equation 5 is based on Stokes law, implying that the particle Reynolds number (Re_M) must be less than one ($Re_M<1$), usually known as creeping flow. The particle Reynolds number (Re_M) is calculated using the particle velocity (v_M) and its diameter (d_M), as well as the velocity (v_L) and viscosity (η_L) of molten steel (Eq. 6) [12].

$$\mathrm{Re}_M = \frac{\rho_L d_M (v_L - v_M)}{\eta_L} \tag{6}$$

The molten steel in creeping flows ($Re_M<1$) tends to wrap a spherical particle smoothly [13]. However, the motion of a particle in centrifugal casting is turbulent, leading to the development of new models to improve the prediction of particle segregation in the centrifugally cast product [11].

Gao and Wang developed a model based on Eq. 5, assuming that there is only heat transfer throughout the outside of the casting. Three different balances are established and combined in the Gao and Wang model: mass balances for particles, molten metal and the solidified matrix; momentum balances for particles and the molten metal; and a thermal balance, including the heat contribution of each constituent phase, like gas, molten metal, and solid, within the system [10], [11]. The combination of balances leads to the velocity of particles, v_M, in the molten metal in the centrifugally cast product, shown in Eq. 7,

$$v_M = \frac{(\rho_M - \rho_L) f_M \gamma d_M^2}{4\eta_L \beta^2 (f_M + f_L)^2} \tag{7}$$

where, f_M is the volume fraction of the particles and f_L is the volume fraction of the molten steel. β is given by Eqs. 8 and 9,

$$\beta = \sqrt{\frac{9(1-f_L)C}{2}} \tag{8}$$

$$C = (1 - f_M)^{-4.65} \qquad (9)$$

where, C is the sedimentation rate that takes into account the inter-particle collisions, impeding particle motion to some extent, while the rest of the particles move through the molten metal according to the ideal Stokes formula (Eq. 5), assuming single spherical particles within the system [11].

The Gao and Wang model also indicates that the particle motion is influenced by two opposing forces; the centrifugal force and a viscous drag force. A centrifugal force drives particles towards the inside diameter of the centrifugally cast product. A viscous drag force tends to reduce and oppose the particle motion as the melt viscosity increases. Gao and Wang show the relationship between the viscous force by unit volume ($M_M{}^D$) and the contribution of a particle in the intrinsic viscosity (η_L) of the melt and volume fraction (f_L) in Eq. 10.

$$M_M^D = \frac{18(1 - f_L)\eta_L C}{d_M^2} f_L^2 (v_L - v_M) \qquad (10)$$

The study of the flow and melt deformation due to the particle motion can also be studied using the apparent viscosity, η_{app}. The apparent viscosity (η_{app}) depends significantly on the volume fraction of particles (f_M), as well as the melt or liquid phase viscosity (η_L) [14]. The apparent viscosity of the melt (η_{app}) can be determined using Eq. 11 [11].

$$\eta_{app} = \eta_L \left(1 + 2.5 f_M + 10.05 f_M^2\right) \qquad (11)$$

The inclusion motion and viscosity of the molten metal are also influenced by the melt temperature. The melt temperature continuously decreases during the centrifugal casting process, increasing the solid volume fraction, f_s, referred to as solidification front, from the outside towards the inside diameter of the centrifugally cast product. At the beginning of the solidification process, the solid volume fraction is present in small quantities and is surrounded by a continuous liquid film. As the solidification proceeds, the solid volume fraction increases and the dendritic coherency is finally reached when a continuous solid skeleton is formed [11].

The advancement of particles by their size in the solid skeleton relies on the time taken to reach the maximum acceleration in the centrifugally cast mold, $t_{\gamma \mathrm{max}}$. If $t_{\gamma \mathrm{max}}$ is short, large particles are prone to attain great velocities and be concentrated at the inside diameter of the centrifugally cast product due to the fact that the solidification front is not too dense at the beginning of the casting process. If $t_{\gamma \mathrm{max}}$ is long, a well defined and coherent solidification front pushes the large particles towards the inside diameter, suggesting the particle pushing effect [11]. In both cases, small particles in the melt are eventually captured between the secondary dendrite arms of the solid skeleton (Figure 1.5) [11].

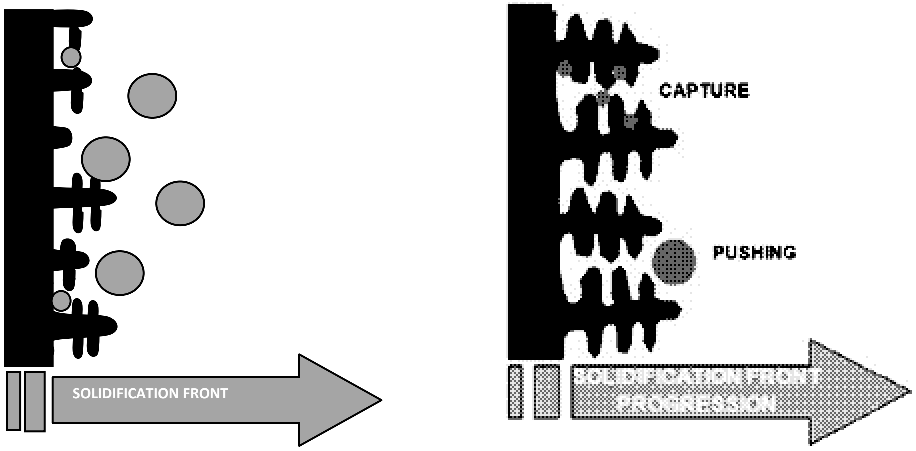

a) b)

Figure 1.5. A schematic illustration showing a) the inclusion flotation towards the ID at the early stages of the solidification process and b) the particle pushing effect after the formation of a coherent solidification front [11]

1.2.1.2. Types of non-metallic inclusions. There are two classifications for non-metallic inclusions:

a) Exogenous Inclusions. Exogenous inclusions are large and irregularly shaped particles that are macroscopically visible either at or beneath the external casting surface. These types of inclusions easily float out, but they can be trapped in regions that solidify rapidly or where their flotation is hindered due to insufficient flotation time [15]. Exogenous inclusions are primarily derived from external causes, including, re-oxidation, entrained slag and lining erosion [8], [15].

Svoboda et al. performed a research project to analyze 500 macro-inclusions from carbon and low alloy steel samples collected in 14 U.S foundries (Figure 1.6) [16]. It was shown that the majority of exogenous inclusions come from re-oxidation, representing 83 % of the total macro-inclusions. This means, the free radicals in the melt are extremely reactive with their environment [16]. The entrainment of air and slag is due to the turbulent mixing of the molten steel during the transfer between vessels. Furthermore, the lining erosion may be caused either by the chemical reactions between the refractory and melt or by the high steel volume that impacts the refractory lining during pouring [15].

b) Indigenous Inclusions. Indigenous inclusions are formed either during de-oxidation or solidification [8], [14], [15]. The majority of indigenous inclusions are formed by the thermodynamic affinity of reactive components with the remaining impurities (oxygen and sulfur) in the melt. Inclusions nucleate and grow shortly after adding the de-oxidizer to the melt. Large indigenous inclusions typically float to the slag surface. In contrast, small indigenous inclusions are trapped in the melt and passed to the next casting process. Indigenous inclusions are also formed and trapped near the liquidus temperature inside the mushy zone during solidification. The solubility of the remaining impurities (oxygen, nitrogen and sulfur) decreases as their concentration becomes larger in steel, inducing inclusion precipitation during dendrite solidification [14], [15].

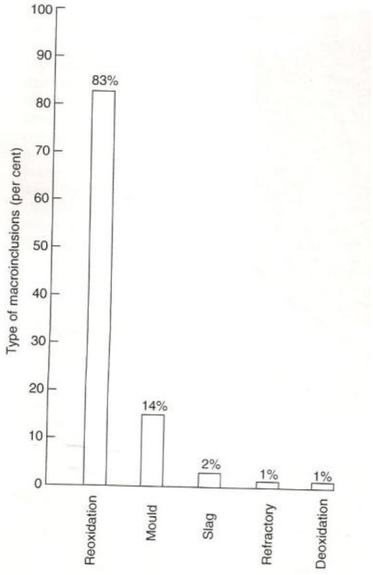

Figure 1.6. Comparison and classification of inclusion distribution (>10μm) in low alloy steel castings using a total sample of 500 inclusions from 14 foundries in the U.S. [16]

1.2.1.3. Experimental analysis on non-metallic inclusion distribution in centrifugally cast products. There are few researchers that have studied the non-metallic inclusion distribution in centrifugally cast products or the complex effects of centrifugal forces within the system. Katavić and Odanović studied centrifugally cast *CrMo* steel pipes (0.3*%C*, 0.08%*Al*, 0.025%*S*, 0.44%*Si* and 0.60% *Mn)* to analyze the inclusion distribution from the outside to inside diameter of the cast product. It was observed that the maximum size of inclusions in the *CrMo* cast steel pipe was less than 15 μm. The largest amount of inclusions was concentrated at the outside diameter (Figure 1.7). Katavić and Odanović stated that the outside diameter of the cast tube solidifies first and the microstructure in this zone differs from the inside diameter. This means, fine precipitates are observed in ferrite grains at the outside diameter and a more dispersed microstructure is shown at the inside diameter of the *CrMo* steel pipe (Figure 1.8). The radial segregation of non-metallic inclusions is also influenced by high mold rotational speeds and the ratio of the mold wall thicknesses (δ_k) and tube wall thickness (δ). If the $\delta_k / \delta > 1$, a higher cooling rate is achieved, producing a finer grained structure at the outside diameter (bainite and martensite) [17].

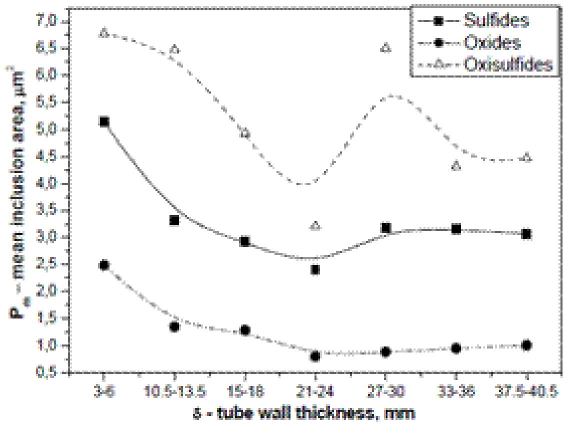

Figure 1.7. Average inclusion area (μm^2) in the radial direction of the centrifugally cast *CrMo* steel pipe showing inclusion distribution from the outside (3 mm) to the inside region (40.5 mm) [17]

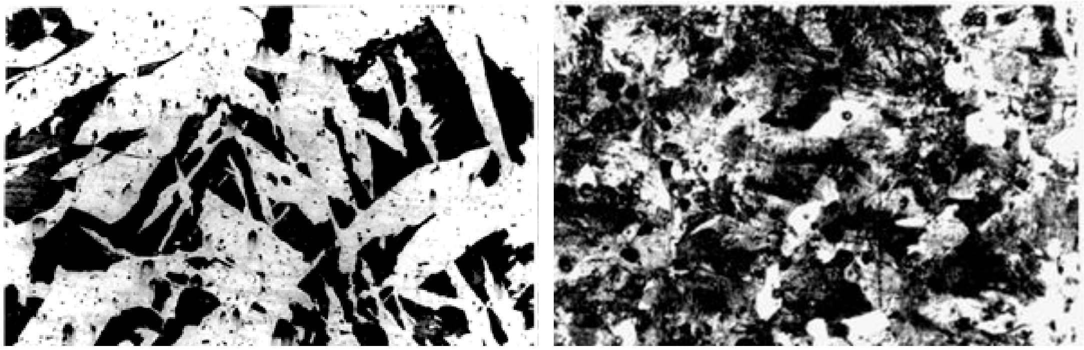

a) b)

Figure 1.8. a) Fine precipitates are irregular in shape and size in a matrix of ferrite and pearlite at the outside diameter (1-3 mm) of the centrifugally cast tube, b) A more disperse microstructure is observed in a matrix of ferrite and pearlite at the inside diameter (17-23 mm) of the centrifugally cast tube [17]

The inclusion distribution analysis made by Katavić and Odanović requires further examination because neither stock removal from the inside diameter (if applicable), nor the location of the centrifugally cast steel samples were specified in their study. Mirzoyan and Pavperova analyzed the inclusion distribution in centrifugal casting using several cross sections around semi-finished 15kh1M1F steel products (Figure 1.9). Mirzoyan and Pavperova revealed that the inside diameter of the centrifugally cast 15kh1M1F steel product showed the largest amount of non-metallic inclusions, especially coarse slag inclusions up to 120µm and porosity. The outside diameter consisted of macro-inclusions due to the interaction of the molten steel and refractory during the pouring process. The center of the centrifugally cast 15kh1M1F steel product was characterized by an extremely low content of both individual and agglomerated non-metallic inclusions that were distributed almost uniformly throughout [18].

Mirzoyan and Pavperova also studied the inclusion distribution along the length of the centrifugally cast 15kh1M1F steel product (Figure 1.10). Figure 1.10 shows that the amount of non-metallic inclusions increased towards the non-pouring end of the casting. This means, the metal temperature at the pouring end is usually 104-140 ºF (40-60 ºC) higher than the opposite end, reducing significantly the movement of inclusions at the non-pouring end [18].

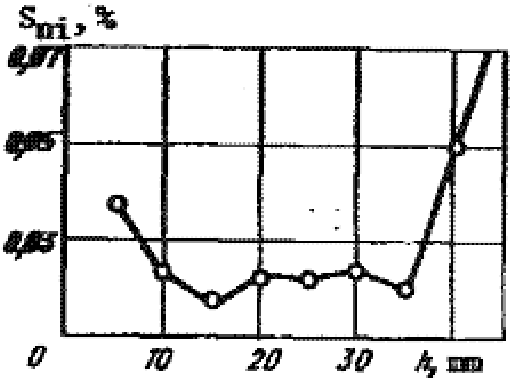

Figure 1.9. Area covered (S_{ni}) by non-metallic inclusions from the outside (*h*=0 mm) to the inside diameter (*h*=45 mm) of the centrifugally cast 15kh1M1F steel product [18]

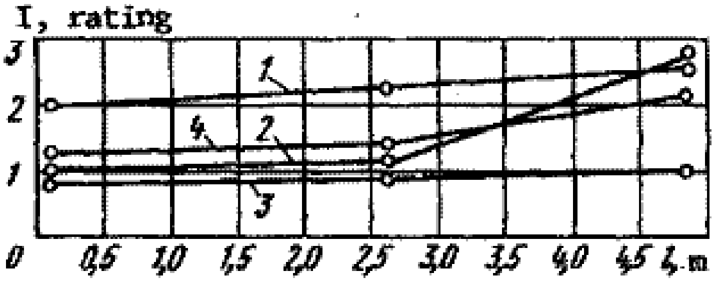

Figure 1.10. Non-metallic inclusion distribution along the length of the centrifugally cast steel product (Z=0 m= pouring end; Z=5 m= opposite pouring end) based on the standard scale of inclusion analysis (GOST 1778-70) [18]

1.2.2. Porosity. There are different types of porosity that may be detrimental to the mechanical properties of the cast product. The extent of the impact is based on the use and type of the final casting.

1.2.2.1. Gas porosity. Gas porosity is influenced by the gas dissolved in liquid steel, which is non-soluble in solid product and nucleates and grows as entrapped gas porosity during solidification. Pore nucleation theories involve homogeneous and heterogeneous nucleation.

Homogeneous nucleation of a bubble in the interior of a liquid is associated with the pressure P_e and the amount of work P_eV to repel the liquid far enough to produce a bubble of volume V. The new liquid-gas interface of area A requires work equals to γA, where γ is the interfacial energy per unit area. In order to fill the bubble with vapor or gas, the work must be equal to – P_iV. The negative sign is due to the pressure inside the bubble, allowing the formation of the bubble. The total work for the bubble formation is described in Eq. 12,

$$\Delta G = \gamma A + P_e - P_i V \tag{12}$$

where, the pressure difference between the exterior and the interior of the bubble (P_e-P_i) is now designated as ΔP.

ΔG is also associated with the bubble radius r. This relationship is the dense phase nucleation in which a maximum value or critical radius is achieved, resulting in an energy barrier to nucleation. The critical radius r^* is given by Eq. 13,

$$r^* = -2\gamma / \Delta P^* \tag{13}$$

where, ΔP^* is the critical pressure difference and γ is the interfacial energy per unit area at which nucleation occurs. Small bubbles with radii less that r^* will disappear from the liquid. If the critical radius r^* is exceeded, the bubble will tend to grow to an observable size in the liquid [16].

Eq. 13 along with experimental values of interfacial energy (γ) and atomic sizes (nm) were used by J. Campbell to estimate an interfacial energy (γ) of 1.9 N/m and a ΔP^* of 76,000 atm for liquid iron. This means that homogeneous nucleation is extremely difficult because the required pressure for nucleation is so high. However, the nucleation problem may be reduced by the presence of surface active impurities in the molten steel. Impurities, such as non-metals O, P and S, react in liquid iron, reducing the interfacial energy and pressure required for nucleation ($\gamma_{\text{liquid iron at 0.2 wt\% O}} \cong 1.0$ N/m). The non-metals can also precipitate as liquid inclusions during solidification or at the solidification front. Liquid FeO inclusions at the solidification front decrease the interfacial energy to 0.6-0.5 N/m and the critical pressure to approximately 17,000 atm. However, the critical pressure of 17,000 atm is still unattainable, impeding gas pore nucleation [16].

Heterogeneous nucleation considers that a good nucleation site for porosity entails solid substrates like non-metals. Non-metals like O, P and S, can precipitate as inclusions and make an angle θ with the liquid iron. If the angle between the solid substrate and the liquid iron is $\theta=0^{\circ}$, complete wetting occurs in which the cohesion energy of the solid and the liquid is high. In complete wetting, the bubble is out of contact with the solid, displacing itself to a more favored position in the liquid iron. If the angle between the solid substrate and the liquid iron is θ=180º, complete non-wetting occurs in which easy decohesion of the liquid from the solid substrate is attained. In complete non-wetting, the bubble is in direct contact with the solid substrate and the liquid, promoting the void nucleation in the liquid iron. Figure 1.11 indicates that there is no difficulty for heterogeneous nucleation in the presence of complete non-wetting substrates. Nevertheless, many researches like Livingston and Swingley were not able to observe a contact angle greater than 160 degrees. Instead, Figure 1.11 establishes that the optimum nucleation occurs when the contact angle θ exceeds 60 or 70 degrees [16]. If this assumption is correct, the non-wetted solid substrates only requires about one-twentieth of the critical pressure for heterogeneous nucleation in the liquid. If a highly non-wetting solid substrate or inclusion were present inside the liquid *FeO* inclusion, the critical lowest pressure of this complex inclusion can be reduced further to 850 atm (17,000 atm/20= 850 atm) [16].

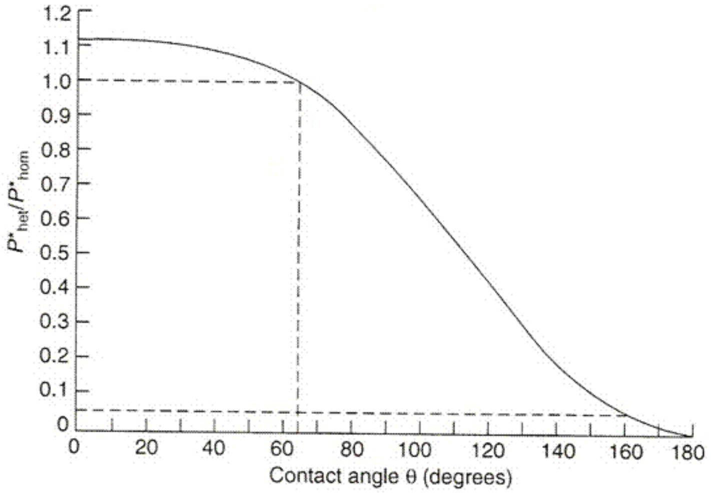

Figure 1.11. - Relationship between the contact angle of a bubble against a solid substrate and critical pressure showing the changes of a solid substrate from wetting (θ= 0) to non-wetting (θ= 180) [16]

The critical pressure, $\Delta P*$, also depends on the relationship between pressure, velocity and elevation within castings, provided by the Bernoulli equation. The Bernoulli equation cannot be applied everywhere in the fluid flow, but rather in regions where the frictional forces are negligibly small compared to other forces acting on the system. This implies that the Bernoulli equation does not apply on regions that are very close to solid walls (boundary walls) and directly downstream of particles (wakes). The Bernoulli equation is then used in regions in which the fluid motion depends on the combined effects of pressure and centrifugal forces (Eq. 14) [13], [19].

$$P = P_O - \rho g z + \frac{1}{2}\rho \varpi^2 r^2 \tag{14}$$

where, P is the total pressure along the streamline, P_O is the initial pressure, ρ is the fluid density, g is gravity, z is the differential height, ω is the angular velocity and r is the distance between the rotation axis and a given position in the centrifugally cast product. Each term of this equation represents different pressures within the system: P_O is the static pressure; ρgz is the hydrostatic pressure, taking into account the elevation effects of fluid weight on pressure; and $½\rho\omega^2r^2$ is the dynamic pressure, considering the pressure rise when the fluid motion is stopped within the system [13].

The total pressure, P, in centrifugally casting is typically higher than gravity casting due to the effect of centrifugal forces on the dynamic pressure, creating pressure far in excess within the system. The critical pressure, ΔP^*, for porosity nucleation in centrifugal casting is so high that the probability of gas pore formation either by homogeneous or heterogeneous is minimized significantly in comparison to gravity casting.

1.2.2.2. Microposity in cast alloys. Microporosity is composed of very small voids that are formed in the interdentritc residual liquid of the casting. Nucleation of bubbles may be either homogeneous or heterogeneous, but in some cases, there is no need of nucleation to grow pre-existing stable micro-bubbles. Pre-existing micro-bubbles grow by the pressure drop of a liquid in the mushy zone during solidification. Over a longer period of time, the bubble may interact with the solutes in the liquid, like hydrogen, resulting in growth of gaseous pores. The growth of pre-existing micro-bubbles is also influenced by the dendrite arm spacing (DAS) and cooling rate of the casting. If the DAS size is decreased, the growth of the bubble and the probability of microporosity formation are limited at high cooling rates [20].

Pre-existing bubbles may also originate cracks that are formed along a continuous array of fine solid particles in the grain boundary. These cracks are hot tears that can lead to embrittlement of the solid by the presence of solid inclusions. Pore formation will occur inside hot tears during the end of the solidification process [20].

1.2.2.3. Shrinkage porosity in centrifugally cast products. A better thermal conductivity and interfacial heat transfer coefficient (h) between the molten steel and the centrifugally cast mold result in points of increased pressure and a higher solidification rate [11]. However, there are void spaces in the centrifugally cast tube formed by contraction and thermal expansion during the solidification process. Entrapped gasses are usually found at void spaces, reducing the conductivity and pressure of the casting [2], [21]. A low pressure portion, especially near the hollow surface of the centrifugally cast tube (inside diameter), solidifies last, producing macro-porosity due to insufficient liquid feeding to accommodate the shrinkage of the casting [21].

1.3. CALCIUM WIRE INJECTION IN MOLTEN STEEL

The calcium treatment of liquid steel has proven to be an effective method of non-metallic inclusion modification and improvement of steel cleanliness.

1.3.1. Method of *Ca*-Addition. The challenges and limitations of several techniques for calcium alloy treatment in the ladle have been analyzed since the late 1960s. The Thyssen Group in Germany was one of the first companies to develop the Thyssen Niederrhein (TN) process for steel desulfurization. In the TN process, pulverized solid particles of calcium alloys were contained in a pressure vessel that was mounted to a swing arm. The vessel was connected to an immersion lance over a piping system. The swing arm, pressure vessel and the immersion lance were lowered to inject the solid particles through an inert gas carrier into the molten steel. The TN process produced acceptable steel products due to the calcium ladle treatment, but the clogging of the lance outlet tended to occur at low gas pressures, interrupting the calcium ladle treatment of the steel. Oscillation of the lance also produced breakage of the ladle lining, as well as the destruction of the lance [22].

Addition of calcium alloys to the tap stream was performed by Washburn Wire Co, but this technique was unacceptable due to the severe metal splashing. The plunging technique was then developed in which a calcium cylinder was placed over the bottom end of a refractory covered rod. The calcium cylinder and the rod were lowered to the bottom ladle, producing uncontrolled re-oxidation and metal splashing in all directions of the slag surface [23]. By late 1979, the cored wire injection technique was performed and improved by AFFIVAL (Figure 1.12) [24], [25]. AFFIVAL deformed the calcium cored filler into a rectangular tube, and later, into a round shape. The purpose of deformation of the calcium core filler was to produce a compact powder, resulting in better calcium reaction with the melt [25]. Typically, the rate of the reaction is more controlled, increasing the amount of calcium dissolved into liquid steel. The amount of impurities and metal splashing in the molten steel are also reduced in the calcium wire ladle treatment [23].

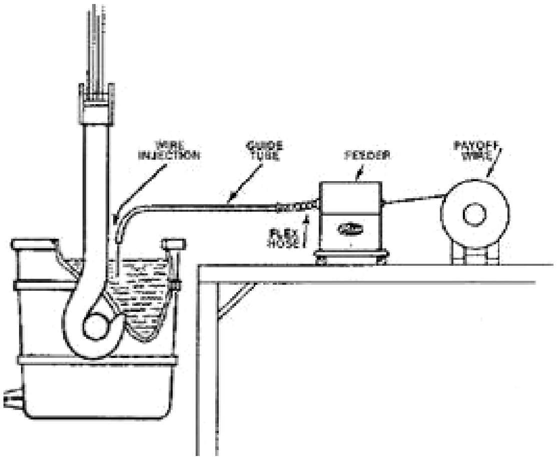

Figure 1.12. Schematic illustration of the typical calcium wire injection method [24]

1.3.2. Calcium Wire Ladle Treatment. Calcium cored fillers like $CaSi30$ (30% Ca and 60% Si), $FeCa$, $CaSiBa$, and $CaSiBaAl$ are commonly used for treating molten steel after de-oxidation. The sequence of reactions regardless of the type of calcium filler composition is the same [26]:

$$Ca_{(s)} \rightarrow Ca_{(l)} \rightarrow Ca_{(g)} \tag{15}$$

$$Ca_{(g)} \rightarrow [Ca] \tag{16}$$

$$[Ca] + [O] \rightarrow CaO \tag{17}$$

$$[Ca] + [S] \rightarrow CaS \tag{18}$$

$$[Ca] + (x + 1/3)\ Al_2O_3 \rightarrow CaO \bullet x\ Al_2O_3 + 2/3[Al] \qquad (19)$$

Some of the calcium from the cored filler is combusted with air, causing the emission of fumes during the calcium treatment. Typically, the emission of CaO vapors is decreased for aluminum killed steels with relatively low sulfur content (10ppm $<S$ <40ppm), in which the calcium retained in the molten steel modifies most of the alumina inclusions to low melting point calcium aluminates [23], [26].

The calcium retained in the molten steel after ladle wire injection and prior to casting often forms calcium aluminates that float to the ladle surface, reducing the calcium yield in the molten steel [26]. The calcium yield is the ratio between the dissolved (Ca_{Total}- $Ca_{Non\text{-}metallic\ Inclusions}$) and injected calcium in the post-tap treatment. In low melting point, pure calcium wire fillers ($FeCa$~ 1472 °F, 800°C), the calcium yield is minimized due to the prompt calcium powder evaporation and combustion with air at molten steel temperatures (2910°F, 1600°C). Calcium wire fillers containing Si, Al, Ni or Cu (melting point~ 2012 °F, 1100 °C) increase the calcium yield in the residual melt, improving the calcium absorption in the molten steel [27]. The calcium yield in $CaSi$40 is reported to be greater than $CaSi$30 due to the fact the calcium content in $CaSi$40 is around 10% greater than $CaSi$30, minimizing the wire consumption, production cost and injection time [28].

A guide tube is usually used to introduce the calcium cored fillers into the melt vertically. The guide tube exit is 12-16 in (300-400 mm) above the molten steel leading to almost complete immersion without hitting the bottom of the ladle and reaction of the cored wire with the melt. The wire injection rate is also important to assure the melting of both cladding and filler. An effective injection rate avoids the cluster of supersaturated local regions of steel. Supersaturated regions can be carried up to the slag and the calcium yield decreases significantly in the molten steel [28].

1.3.3. Effect of Calcium Treatment on Non-metallic Inclusions. One of the elements that is used for de-oxidation due to its greater affinity for oxygen than carbon is aluminum [29]. After aluminum de-oxidation, the aluminum oxide rich inclusions are formed at a very low nucleation rate. A low nucleation rate results from high interfacial energy between the aluminum oxide rich inclusions and molten steel ($\gamma_{Al_2O_3}$=2290 erg*cm^2), increasing the inclusion size distribution [30]. In industrial practice, a broad inclusion size distribution minimizes the cleanliness of the molten steel, but the size distribution can be enhanced by the calcium wire ladle treatment. The calcium activity in the molten steel gradually increases to form low melting point calcium aluminates with low interfacial energy ($\gamma_{CaO\text{-}Al_2O_3}$=1300 erg*cm^2), decreasing the inclusion size distribution in steel [30], [31].

Low melting point calcium aluminates, consisting of $3CaO \bullet Al_2O_3$, $12CaO \bullet 7Al_2O_3$ and $CaO \bullet Al_2O_3$, are liquid at steel casting temperatures [32]. These type of calcium aluminates usually melt in the temperature range of 2543- 2921 °F (1395-1605°C) (Figure 1.13) [24]. The melting temperature for calcium aluminates is significantly lower than the alumina inclusions (3762°F, 2072°C) [31]. Low melting point calcium aluminates are easier to remove from the molten steel because of their rapid coagulation to form round aggregates with Al_2O_3 and other inclusions that easily float to the ladle surface [22]. The *Ca* wire ladle treatment reduces the tendency for the modified inclusions to attach to the refractory surface, preventing nozzle blockage during teeming and continuous casting.

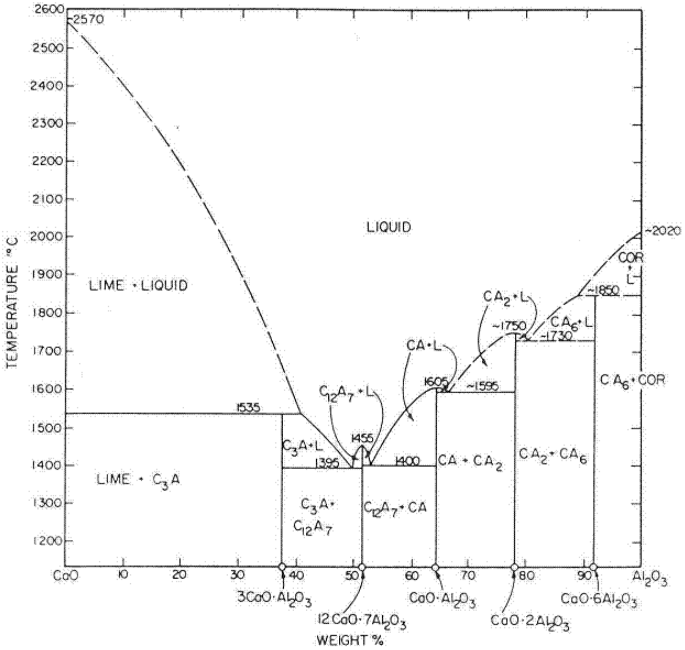

Figure 1.13. The binary phase diagram of CaO- Al_2O_3 [14]

1.3.4. Effect of Calcium Treatment on Mechanical Properties. The improvement of ductility and mechanical properties is influenced by the suppression of manganese sulfide and brittle inclusions like Al_2O_3 in steel [33]. Brittle inclusions like Al_2O_3 are typically angular in nature that becomes fragmented during rolling, promoting void nucleation in the steel [33]. *Mn* and *S* are ejected from the solidifying dendrites to the remaining liquid. Their concentration in the remaining liquid tends to precipitate *MnS* in the interdendritic spaces towards the end of the solidification process [34], [35]. The manganese sulfides produce *MnS* stringers that cause stress concentrations at the steel/ inclusion interface, reducing the ductility of the cast steel product [31].Theoretically, sulfides are classified into three categories: globular sulfides that are randomly distributed in the metal matrix (Type I); thin films that embrittle the cast steel due to the chainlike formation along the grain boundaries (Type II); Sulfides that have angular or irregular geometric shape, which are less harmful than type II, but are more harmful than type I (Type III) (Figure 1.14) [16], [36].

Multiphase inclusions involve manganese and calcium sulfides ((*Mn, Ca*) *S*) around low melting point $CaO \bullet Al_2O_3$, known as bi-phase inclusions. A bi-phase inclusion is composed of an oxide prime phase surrounded by a sulfide secondary phase, lowering the oxygen and sulfur contents in the melt. The oxisulfide inclusions containing calcium form non-deformable round inclusions that prevent cracking and deformation during rolling, providing better mechanical properties when compared to other types of inclusions (Figure 1.15) [26], [31], [33], [36], [37].

The activity of calcium in the molten steel will increase gradually and form low melting point calcium aluminates that will surround the outer layers of oxide inclusions in the melt. An oxide inclusion does not require to be transformed completely into low melting point inclusions, as long as the liquid inclusion at the outside layer is thick enough to prevent crack formation and voids at the inclusion-steel matrix during rolling (Figure 1.16) [31].

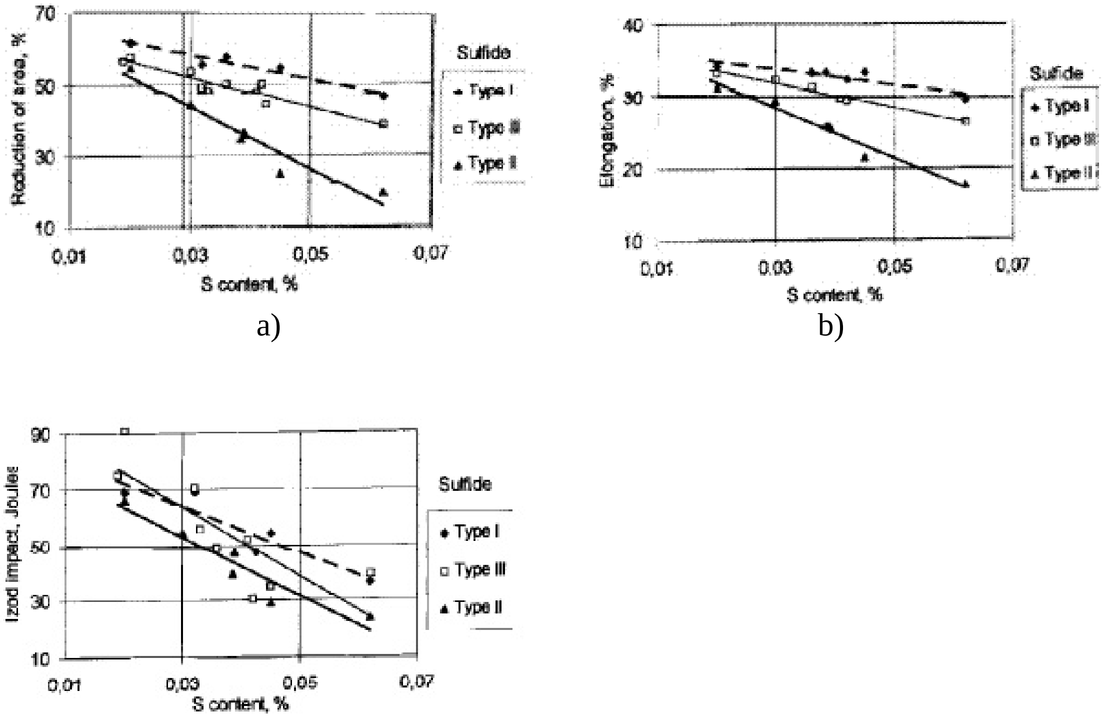

a)

b)

c)

Figure 1.14. Percentage reduction area, percentage elongation and izod impact of 0.20% *C* steel castings after aluminum deoxidation (a, b and c) [36]

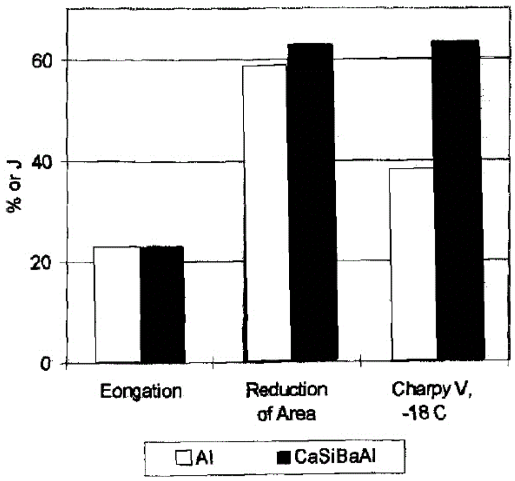

Figure 1.15. Comparison of mechanical properties of 0.20 %*C* cast steel treated with *Al* followed by CaSiBaAl wire injection [36]

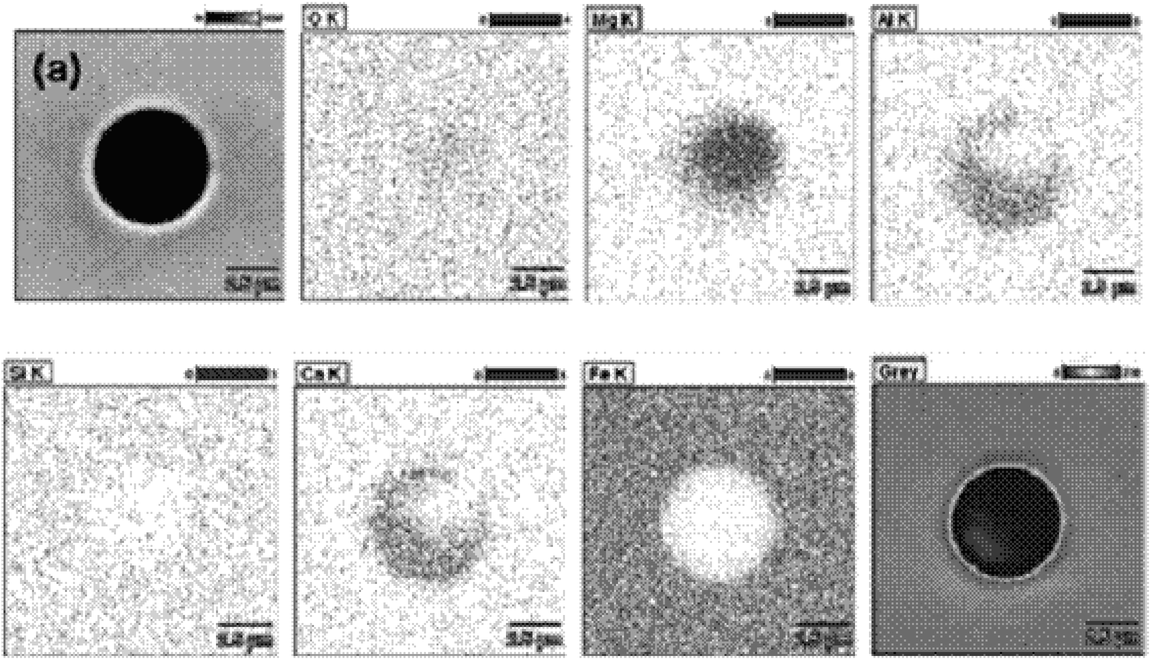

Figure 1.16. SEM-mappings showing a combination of a high melting point inclusion (MgO) in the center and a low melting point inclusion with high calcium content at the outer surface [31]

1.4. EFFECTIVENESS OF INCLUSION MODIFICATION BY CALCIUM WIRE LADLE TREATMENT

1.4.1. Inclusion Modification with Respect to Time. The interaction of a high basicity slag (42-45 %CaO and 6-7% SiO_2) with the molten steel has also shown to modify angular oxide inclusions to low melting point calcium aluminates. M. Jiang *et al* performed experiments to analyze the steel/ high basicity slag reaction in steel melts held from 30 to 80 minutes without stirring at 2910 °F (1600°C). The total oxygen (T.O) decreased significantly after 90 minutes and the sulfur content was quiet low throughout the metal holding time in the ladle, enhancing the cleanliness of steel (Table 1.1). Table 1.2 shows that spherical inclusions are formed with increased calcium reaction time. It reveals that most of the angular oxide inclusions decreased and are transformed into low melting point inclusions containing calcium with longer time, especially after 180 minutes [31].

Table 1.1 Chemical composition of steel held for 30, 60, 90 and 180 minutes with no stirring at 2910°F (1600°C) [31]

CHEMICAL COMPOSITION OF MOLTEN STEEL

Time (min)	%C	%Si	%Mn	%Al	%Ca	%S	T.O.
30	0.46	1.52	0.84	0.038	0.0003	0.0005	0.0014
60	0.37	1.52	0.84	0.041	0.0002	0.0006	0.0012
90	0.46	1.50	0.84	0.042	0.0005	0.0008	0.0008
180	0.41	1.46	0.84	0.036	0.0010	0.0005	0.0007

Table 1.2 Modification of inclusion morphology with respect to calcium reaction time [31]

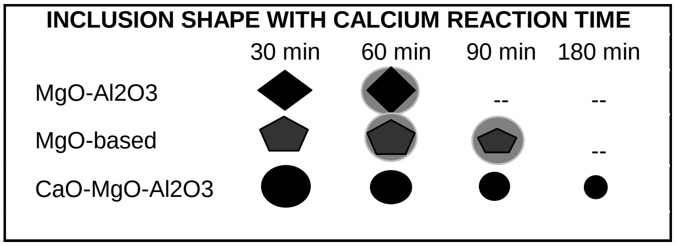

INCLUSION SHAPE WITH CALCIUM REACTION TIME

	30 min	60 min	90 min	180 min
MgO-Al2O3	◆	◆	--	--
MgO-based	⬟	⬟	⬟	--
CaO-MgO-Al2O3	●	●	●	●

1.4.2. Inclusion Modification with Different *Ca* Amounts and Injection Speeds. V. Singh et al. performed calcium injection experiments in static casting. The steel was melted in a 2,200 lb (998 kg) medium frequency induction furnace (IF) followed by the post-tap treatment. In the post-tap treatment, five heats were calcium treated using different calcium additions and injection speeds in a 1,100 lb (499 kg) ladle. One of the heats was the base case with no calcium added in the ladle. Figure 1.17 illustrates that the amount of oxide inclusions increases after aluminum and *FeTi* additions in the ladle. This indicates that re-oxidation occurs during pouring and from the transfer ladle to the gating system. Similarly, re-oxidation is also observed in the calcium treated heats, but the amount and type of alumina inclusions changed after *CaSi* wire injection, especially with increased calcium and higher injection speeds. A high injection speed improves the *Ca*-reaction due to more *Ca* addition in less time and deeper penetration of the wire into the melt to form calcium aluminates. However, the silicon content in the *CaSi* wire promotes $MnSiO_3$ inclusions in the steel (Figure 1.18) [32].

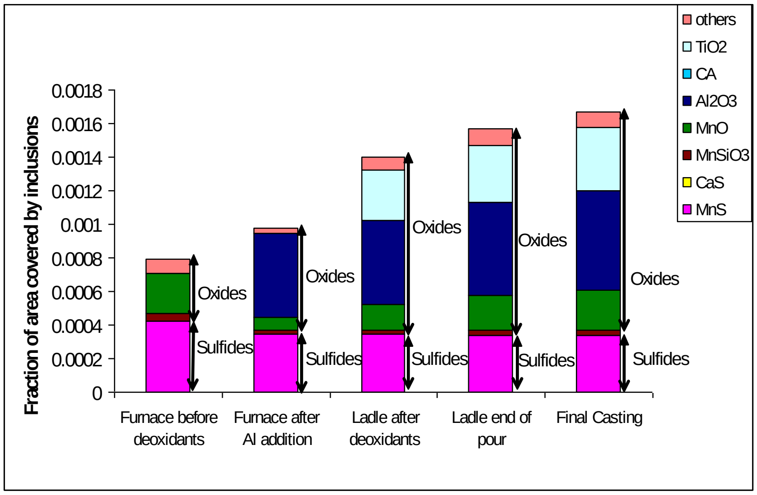

Figure 1.17. The base case heat with no calcium treatment showing re-oxidation from tapping after aluminum and *Fe70Ti* additions to the final casting [32]

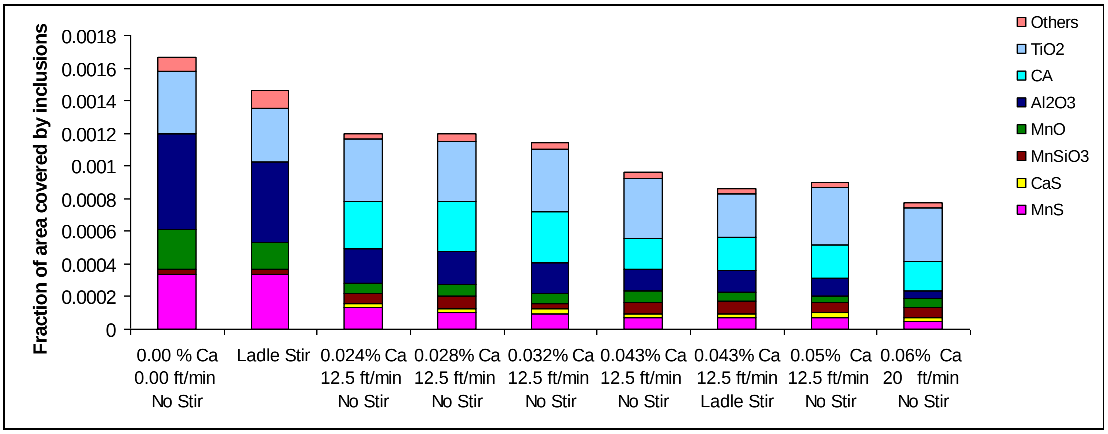

Figure 1.18. Calcium injection experiments with different additions and injection speeds showing better inclusion modification with increased *CaSi*-addition [32]

1.5 OUTLINE OF THE PROJECT

The literature review indicates that centrifugal casting process is suitable for production of steel components for critical applications, in particular, for pressure service. At the same time, non-metallic inclusions tend to be formed during the steelmaking and centrifugal casting processes. These defects reduce the mechanical properties of the low alloy steel. In order to improve the mechanical properties, the “cleanliness” of the molten steel after aluminum de-oxidation needs to be improved. Calcium wire ladle treatment has the potential of modifying the chemical composition of non-metallic inclusions, forming well dispersed spherical inclusions, reducing type II sulfide inclusions, and increasing the fracture toughness of the centrifugally cast products.

In this research, calcium wire injection was performed using a 12,000 lb ladle in order to minimize casting defects. Non-metallic inclusions and porosity in centrifugally cast tubes were evaluated through an automated particle identification and characterization analyzer, ASPEX PICA 1020, scanning electron microscopy (SEM) and optical microscopy. The ASPEX PICA 1020 utilizes a backscattered detector (BSED) and energy dispersive spectroscopy (EDS) system for a rapid analysis of the distribution, type and morphology of non-metallic inclusions and porosity present in the steel. SEM examination was used to determine the fracture mode after impact testing of the centrifugally cast tubes. Finally, the optical microscopy was used to analyze the effects of calcium treatment on porosity of castings.

2. EXPERIMENTAL PROCEDURE

A total of five heats, denoted as heats A (Base Case- no *Ca* treatment), B, C, D and E were conducted in a participating industrial foundry to analyze the combined effects of centrifugal casting and calcium wire ladle treatment on the cleanliness and mechanical properties of the centrifugally cast steel products. Medium carbon, low alloy cast steel was melted in an electric arc furnace (EAF) followed by argon oxygen decarburization (AOD) treatment. Calcium-bearing wire was fed into the ladle either early in the process (just after AOD) or just prior to centrifugal casting. Heats B and C were calcium wire fed just prior to casting due to better accessibility of the calcium wire feeder to the 12,000 lb capacity slidegate ladle. Heats D and E were calcium wire fed just after AOD treatment to avoid temperature losses in the ladle during experiments.

2.1. MELTING PROCEDURE

The melting procedure involved EAF followed by AOD treatment. Both EAF and AOD were basic refractory and basic slag practices. Table 2.1 provides the chemical analysis of all heats after AOD final additions, as provided by the participating industrial foundry.

Between 10,000 and 14,000 lbs of metal charge were melted in the EAF. After the charge was melted, oxygen blowing was performed for de-carburization and preliminary refining. After tap, the molten metal was transferred to the AOD for further refining using gas injection from wall-mounted tuyeres. Typically, a more efficient carbon removal is attained by bottom blowing of a diluting gas (argon and nitrogen) to reduce the partial pressure of carbon monoxide, favoring its formation at a lower temperature in the AOD (Eq. 20).

$$C_{(s)} + 1/2O_{2\,(g)} \rightarrow CO_{(g)} \qquad (20)$$

De-oxidation was achieved with aluminum additions in the AOD vessel, increasing the temperature due to the release of energy during the exothermic chemical reactions in the melt. Alloy additions in the AOD were made to fulfill the chemical requirements of the centrifugally cast steel products.

Table 2.1 Chemical composition after final additions in AOD for each heat in wt%

CHEMICAL COMPOSITION AFTER AOD REFINING													
Heat	%C	%S	%Si	%Mn	%Cr	%Mo	%Ni	%Cu	%V	%Ti	%Al	%P	%W
A	0.207	0.001	0.247	0.647	2.524	0.892	0.106	0.094	0.052	0.004	0.067	0.014	0.015
B	0.220	0.000	0.237	0.632	2.600	0.711	0.164	0.134	0.049	0.004	0.070	0.010	0.015
C	0.203	0.001	0.157	0.628	2.702	0.759	0.103	0.128	0.053	0.004	0.062	0.013	0.015
D	0.215	0.001	0.261	0.672	2.926	0.936	0.081	0.117	0.052	0.005	0.051	0.013	0.014
E	0.220	0.001	0.230	0.618	2.561	0.914	0.075	0.102	0.054	0.004	0.042	--	--

2.1.1. Regular Practice. The regular practice with no calcium wire addition in the ladle was denoted as heat A (Base Case-No *Ca* Treatment). After final additions in the AOD vessel, the molten steel was tapped into a slidegate ladle equipped with one bottom porous plug for ladle stirring. The argon flow rates were not measured during the calcium experiments, but argon was purged until it broke through the slag on top of the ladle. The ladle was argon stirred for approximately 15 minutes before casting. A centrifugally cast tube (14” to 20” outside diameter (OD) and 22’ long) was poured in the casting machine. The rotation speed at the beginning of the casting process, which was the maximum rotation speed, was high enough to spread the molten steel over the entire mold (95-160 *G*’s) and was reduced at a constant rate until solidification was completed (~30 *G*’s). The casting machine was stopped 134 minutes after pouring.

2.1.2. Calcium Wire Ladle Treatment. In all of the heats, aluminum was used as a reducing agent and as a fuel. If excessive amounts of aluminum are present in the molten steel, a large amount of alumina inclusions will be formed in the ladle. The larger inclusions are prone to float to the slag, but smaller inclusions could end up as non-metallic inclusions containing aluminum in the steel casting. In order to reduce the amount of these types of inclusions in steel, calcium wire ladle treatment was performed to analyze its effect on the number, size, composition and morphology of non-metallic inclusions in centrifugally cast steel products.

Calcium wire ladle treatment was carried out in a 12,000 lb (5,443 kg) capacity slidegate ladle in which heats B, C, D and E were *Ar*-stirred throughout the 10 minute post-tap treatment and ladle transfer to the casting platform. The calcium wire was fed using 10 ft. long feeding tubes attached to a P.C. Campana micro wire-feeder, providing a safe distance between the wire-feeder and molten steel (Figure 2.1). A constant injection rate of 17 ft/ min (0.09 m/s) was used for the steel clad pure calcium wire (98.5 *%Ca*, 0.5 *%Al* and 0.5 %Mg), commonly referred to as *FeCa*, for all heats. The *FeCa* wire diameter was 9 mm. *FeCa*-wire was the only type of wire addition in all heats due to its higher calcium content (0.034 lb/ft- 0.050 kg/m), 38 percent greater than the commonly used calcium silicon wire (0.021 lb/ft- 0.031 kg/m), reducing significantly the injection time in the post-tap treatment.

Tables 2.2 and 2.3 describe the post-tap treatment and casting parameters for each heat.

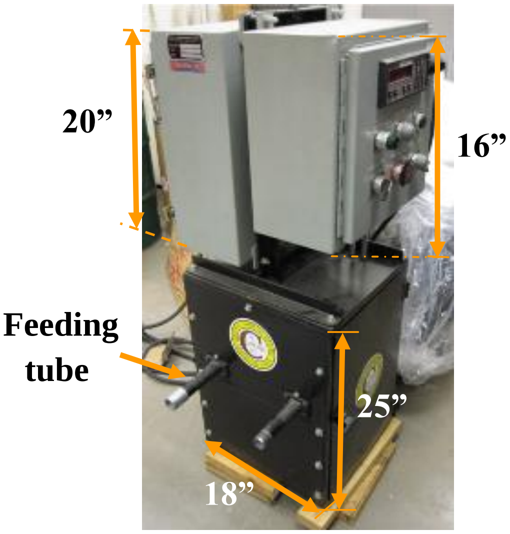

Figure 2.1. P.C. Campana micro-wire feeder used in heats B, C, D and E during the calcium wire ladle treatment

Table 2.2 Calcium injection parameters for each experimental heat

CALCIUM INJECTION PARAMETERS

Heat	Aim %*Ca* added	Wire Type	Calcium Weight Content (lb/ft)	No. of Feeding Tubes	Calcium Injection Speed (ft/ min)	Wire Length (ft)	Ca (lb)	Injection Time (min)
A	N/A		Base Case (No *Ca* Treatment)					
B	0.014	*FeCa*	0.034	1	17	34	1	2.1
C	0.077	*FeCa*	0.034	1	17	154	5	9.3
D	0.096	*FeCa*	0.034	2	17	239	8	10
E	0.139	*FeCa*	0.034	2	17	333	11	10

Table 2.3 Centrifugal casting parameters for each experimental heat, as provided by the participating industry foundry

CALCIUM WIRE LADLE TREATMENT AND CASTING PARAMETERS											
							Tube Dimensions				
Heat	Aim %*Ca* added	Ladle Weight (lb)	Pouring Temperature (°F)	Final Tube Temperature (°F)	Tube Weight (lb)	*Rotation Speed (rpm)	OD (in)	ID (in)	Wall Thickness (in)	Length (ft)	*G*
A	N/A	14,264	2847	1725	10,935	858	20	15	2.60	22	158
B	0.014	11,582	2840	1866	8,130	836	16	11	2.53	22	110
C	0.077	8,835	2860	1798	6,785	860	14	9	2.46	22	95
D	0.096	11,868	2870	1700	8,472	792	16	11	2.53	22	98
E	0.139	11,279	2808	1701	8,150	792	16	11	2.53	22	98

*Maximum rotation speed during centrifugal casting

2.1.2.1. Calcium wire ladle treatment prior to casting. Heats B and C were calcium treated at the casting platform due to better accessibility of the wire feeder to the ladle. The calcium treatment was performed using one feeding tube in the P.C. Campana micro wire feeder because of the low levels of calcium added in the ladle (B- 0.014 *%Ca* and C- 0.077 *%Ca*). The total injection time was around two minutes in heat B and nine minutes in heat C. The injection time in heat B was planned to be longer but was shortened due to the rapid thermal losses in the ladle during the calcium treatment.

2.1.2.2. Calcium wire ladle treatment after AOD. Heats D and E were calcium treated at the AOD deck due to higher tapping temperatures that allowed feeding of the needed calcium without temperature concerns in the ladle. The calcium treatment in both experiments was performed using two feeding tubes in the micro wire feeder due to the large amount of calcium added in the ladle (D- 0.096 *%Ca* and E- 0.139 *%Ca*). The average calcium injection time in both heats was around ten minutes. The transfer ladle was then moved to the casting platform after six minutes.

2.2. SAMPLING AND OXYGEN MEASUREMENT

Lollipop samples were collected throughout the process starting at the AOD, transfer ladle, casting ladle and during the time when the calcium wire ladle treatments were done. Lollipops samples were collected using a submerged chemistry sampler (SaF 400-QS 3012 from Heraeus Electro-Nite). However, lollipop samples were not collected at exactly the same time and place due to severe metal splashing in the ladle. Similarly, the Lab Datacast-2000 was not used for dissolved oxygen measurements in heats B, D and E due to the violent reaction of the Celox oxygen probes with the melt. The dissolved oxygen in heats A (just prior to casting) and C (middle of the *Ca* treatment) was 2 and 3 ppm, respectively, agreeing with the equilibrium levels expected for aluminum killed and calcium treated steels. The total oxygen content ($[O]_{\text{Dissolved}} + [O]_{\text{Inclusions}}$) was measured from all samples, using the Leco TC 500 nitrogen-oxygen analyzer.

Centrifugally cast samples were taken from the tube end opposite to the pouring end of the finished tube for inclusion analysis and impact testing. The samples were taken from the end opposite of pouring because this area reflects the worst case quality likely to be encountered in industrial conditions. It was previously shown in the literature that the amount of non-metallic inclusions increased towards the non-pouring end of the casting due to lower molten steel temperatures, reducing the inclusion motion and cleanliness of the casting [18]. A schematic representation of the cast tube samples showing the location from the inside to the outside of the cast product is given in Figure 2.2. The inclusion analysis of each cast tube was divided into five regions (OD, 0.25, 0.50, 0.75 and ID). The final product region was designated as the average of three samples at x=0.25, x=0.50 and x=0.75 because the inside diameter (ID) at x=0 and the outside diameter (OD) at x=1 are typically removed through secondary machining and not incorporated in the final product. However, no stock removal was performed in the centrifugally cast samples collected.

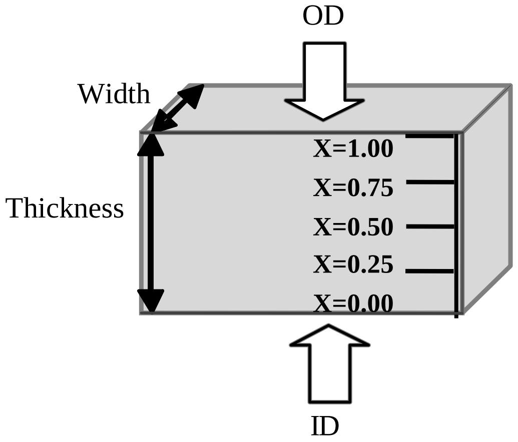

Figure 2.2. Schematic representation of the cast tube sample taken from the end of the finished tube showing the location from the inside to the outside of the cast product

2.3. INCLUSION ANALYSIS

Microscopic specimens from each lollipop and centrifugally cast sample were prepared to analyze inclusions using the automated inclusion analyzer, Aspex PICA 1020. The instrument settings entailed acceleration voltage of 20 KV, initial emission current of 38.5μA and magnification of 500X. Duplication of results was performed by taking the average value of three tests performed in the same location of the specimen.

2.3.1. Background of Aspex Analysis. The automated inclusion analyzer, Aspex PICA 1020, is designed to identify precisely the composition, size, number and distribution of inclusions in a short period of time. The Aspex/ SEM system consists of an electron gun and a backscattered electron detector (BSED) that is sensitive to the atomic number (Z). The BSED detector provides different contrast between areas with different chemical compositions. This means, the light elements with low atomic number appear dark and heavy elements with high atomic number appear bright in the SEM image.

The area of analysis in the specimen is sub-divided into small fields to produce a coarse image at low magnifications (<250*X*). A coarse image increases the spot size of the sample, which means many electrons hit successfully in the area of analysis. The electron beam moves across each individual field using the automated feature analysis (AFA). In the AFA, an inclusion is determined by the thresholds of the Aspex software, resulting in a bright particle in the SEM image. Once the bright inclusion is identified, the software initiates a particle-sizing sequence. The particle-sizing sequence utilizes a rotating chord algorithm, in which the center of the inclusion is identified followed by the drawing of chords with the beam. The chords are used to determine the size and shape of the inclusion (Figure 2.3). The energy dispersive spectroscopy (EDS) spectrum is then acquired to identify the elemental composition of each inclusion. Finally, the data is stored and is evaluated offline in the AFA system (Figure 2.4) [38].

2.3.2 User-Defined Rules for Inclusion Statistical Analysis. The classification rule for the lollipops and centrifugally low alloy cast steel specimens included a vector file based on the reference standards for each element to quantify the EDS spectra. The

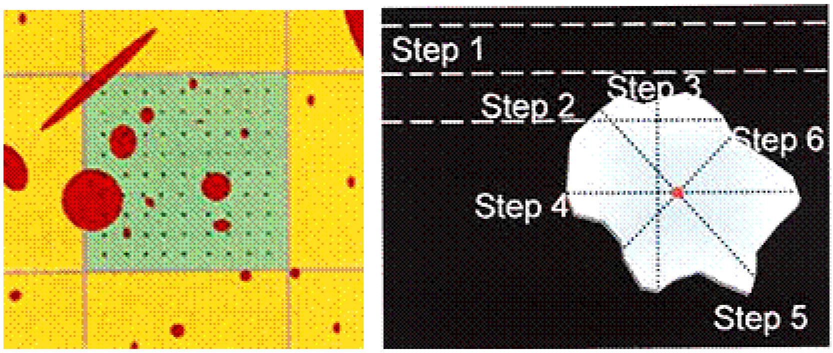
Step 1
Step 2
Step 3
Step 6
Step 4
Step 5

a) b)

Figure 2.3. Identification of an inclusion by the BSED detector followed by the centering and drawing of chords to determine the size and shape of an inclusion [38]

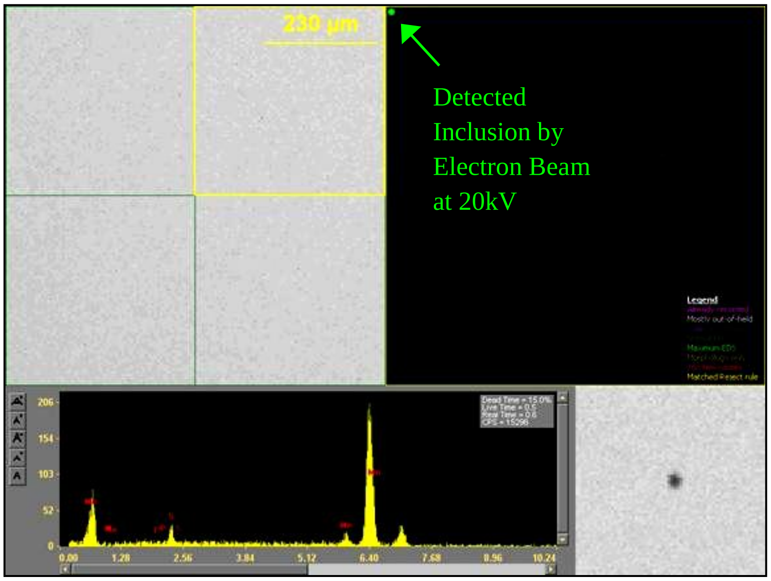
230 µm
Detected
Inclusion by
Electron Beam
at 20kV
Legend
206
154
103
52
0
0.00
1.28
2.56
3.84
5.12
6.40
7.68
8.96
10.24

Figure 2.4. Automated feature analysis (AFA) showing the sub-division of the left SEM image into fields, as well as the identification of a bright particle and its elemental composition by x-ray spectroscopy

vector file was generated using the chemical composition in Table 2.1. This vector file was used to classify an inclusion into broad categories defined by the user-defined rules.

The user-defined rules were divided into classification and zero elements. In the classification category, an inclusion was categorized using the first rule that was evaluated as true, starting with the first rule in the list during the AFA. For example, if *Ca*>10% and *Al*>10% and S<10% (in weight percent) were true for an inclusion, it could be then classified as a low melting point calcium aluminate (*Ca-Al-O*). Images along with the EDS analysis were also acquired during the AFA [39].

The zero element rules were used to distinguish actual inclusions from contamination particles formed during the sample preparation process. Otherwise, the software might misclassify a contamination particle as an inclusion. This contamination usually contained a high percentage of carbon, which were mostly obtained from the polishing media. A more computationally efficient mechanism to quantify the EDS spectra was achieved by producing a zero rule for chromium and iron. Chromium usually overlaps with manganese and vanadium, avoiding an accurate EDS analysis ($Cr_{K\alpha}$= 5.414 keV, $Mn_{K\alpha}$= 5.898 keV, $Cr_{L\alpha}$= 0.571 keV and $V_{L\alpha}$= 0.510 keV) [40]. Iron x-rays were also emitted from inclusions, but did not contribute as part of the elemental composition of these particles.

The inclusion analysis for the lollipops and centrifugally low alloy cast steel specimens was as follows:

a) Oxides and sulfides. The area of inclusion analysis for oxides and sulfides was around 9.8 mm^2. The vector file included *C, O, Cr, Al, Si, P, S, Ca, Ti* and *Mn*. The AFA data was used to evaluate the elemental composition of each non-metallic inclusion to create the classification and zero rules (Tables 2.4 and 2.5).

b) Oxynitrides. Oxynitrides analysis was required after the Leco TC 500 nitrogen-oxygen results due to the large nitrogen pickup in the centrifugally cast samples. The area of inclusion analysis for oxynitrides was around 0.819 mm^2. The vector file included nitrogen and the elements that were used previously in the oxide and sulfide analysis. The AFA data was used to evaluate the elemental composition of each non-metallic inclusion to create the classification and zero rules (Tables 2.6 and 2.7). Unlike the previous oxide and sulfide analysis, a zero rule for oxygen was not created because of the complexity of inclusions containing both oxygen and nitrogen.

2.3.3. User-Defined Rules for Micro-defect Identification. The micro-defects or porosity rule was true when the weight percent iron was equal to or greater than 92 %. This means, the electron beam moves across the micro-defect or porosity, indicating that the total weight percent sum of the main elemental composition of the low alloy steel was less than eight percent ($(Al+ Si+ Mn+ P+ Ca+ S+ Ti+ C)<8$).

Table 2.4. Classification rule for oxide, sulfide and micro-defect (porosity) analysis on the lollipops and centrifugally cast steel specimens

Classification Rule	
Class	Rule Definition
Carbon	C>5
FeO Stains	Fe>=30 and O>=5
Microdefects	Fe>=92 and O<5
MnS	Mn>30 and S>20
CaS	Ca>30 and S>20
Ca-Mn-S	Ca>10 and Mn>10 and S>20
Other Sulfides	S>20
Al_2O_3	Al>20 and Mn<20 and Ca<10 and Si<20 and S<20
CaO	Ca>20 and S<20 and Al<10 and Si<20 and Mn<20
SiO_2	Si>30 and Mn<20 and S<20 and Al<10 and Ca<10
Ca-Al-O	Ca>10 and Al>10 and S<20
MnO	Mn>20 and S<20 and Al<20 and Si<20
Mn-Si-O	Mn>20 and Si>10 and Al<10 and S<20
Mn-Al-O	Mn>20 and Al>10 and S<20

Table 2.5. Zero rules for oxide, sulfide and micro-defect (porosity) analysis on the lollipops and centrifugally cast steel specimens

Zero Rule	
Class	Rule Definition
O=0 if..	Al>=2.5 or Mn>=2.5 or Ca>=2.5 or Si>=2.5
Cr=0 if..	Cr>=0.1
Fe=0 if..	Al>=2.5 or Mn>=2.5 or Ca>=2.5 or C>=2.5 or Si>=2.5
C=0 if..	Al>=2.5 or Mn>=2.5 or Ca>=2.5 or Si>=2.5

Table 2.6. Classification rule for oxide, sulfide, porosity and oxynitride analysis on the centrifugally cast steel specimens

Classification Rule	
Class	Rule Definition
Carbon	C>5
FeO Stains	Fe>=30 and O>=5
Microdefects	Fe>=92 and O<5
MnS	Mn>30 and S>20
CaS	Ca>30 and S>20
Ca-Mn-S	Ca>10 and Mn>10 and S>20
MnS-AlO	Mn>=20 and S>20 and Al>15 and Ca<10
Other Sulfides	S>20
Al-O-N	Al>=20 and N>22 and Mn<10 Ca<5 and S<20
Al-N-Mn-O	Mn>10 and Al>20 and N>22 and S<20
Ca-O-Al-N	Ca>5 and Al>20 and N>22 and S<20
Al_2O_3	Al>20 and Mn<20 and Ca<10 and Si<20 and S<20 and N<22
CaO	Ca>5 and S<20 and Al<10 and Si<20 and Mn<20 and N<22
SiO_2	Si>30 and Mn<20 and S<20 and Al<10 and Ca<10 and N<22
Ca-Al-O	Ca>5 and Al>10 and S<20 and N<22
MnO	Mn>20 and S<20 and Al<20 and Si<20 and N<22
Mn-Si-O	Mn>20 and Si>10 and Al<10 and S<20 and N<22
Mn-Al-O	Mn>20 and Al>10 and S<20 and N<22

Table 2.7. Zero rules for oxide, sulfide, porosity and oxynitride analysis on the centrifugally cast steel specimens

Zero Rule	
Class	Rule Definition
Cr=0 if..	Cr>=0.1
Fe=0 if..	Al>=2.5 or Mn>=2.5 or Ca>=2.5 or C>=2.5 or Si>=2.5
C=0 if..	Al>=2.5 or Mn>=2.5 or Ca>=2.5 or Si>=2.5

2.4 CHARPY IMPACT TESTING AND FRACTOGRAPHY ANALYSIS

Centrifugally cast tube samples from heats A (base case), B (0.014 %*Ca*), C (0.077 %*Ca*), D (0.096 %*Ca*) and E (0.139 %*Ca*) were heat treated prior to mechanical testing. The heat treatment was based on the standard specification for steel castings suitable for pressure service (ASTM A-487). The centrifugally cast samples were austenitized at 954°C (1750 °F), water quenched followed by tempering at 613°C (1135 °F) and furnace cooling to below 316°C (600 °F). The impact test was performed using a Tinius Olsen testing machine with a standard potential energy (PE) of 301.54 ft* lb at room temperature. Charpy impact tests at room temperature were performed using three specimens for each test. The Charpy specimen dimensions for each test were 2 $^{1}/_{6}$” (55 mm) X $^{2}/_{5}$” (10 mm) X $^{2}/_{5}$” (10 mm).

Fractography analysis was performed after impact testing using the JEOL 6060 LV and Hitachi S-570. The composition of each Charpy specimen was analyzed using the energy dispersive spectroscopy (EDS) with an acceleration voltage of 15 kV. Furthermore, Charpy impact specimens were sectioned in the transverse direction near the fracture surface for inclusion analysis using the Helios Nano Lab 600 (SEM FIB/EDS). The specimen preparation entailed the Delta abrasive cutter followed by the SimpliMet 1000 mounting press. Specimens were then polished using the Abramin auto-polishing machine. The acceleration voltage and initial electron beam current for the SEM FIB were 15kV and 1.4 nA, respectively.

3. EXPERIMENTAL RESULTS

The effects of the centrifugal forces and calcium wire ladle treatment on the amount, type, size, aspect ratio and particle spacing in non-metallic inclusions and porosity for the samples, corresponding to heats A (Base Case- no *Ca* treatment), B, C, D and E, were performed using an automated inclusion analyzer, Apex PICA 1020. Microstructural characterization by light optical microscopy and scanning electron microscopy illustrated microstructures (including porosity), as well as the morphology and composition of non-metallic inclusions prior to mechanical testing. The fracture surface after impact testing was also analyzed.

3.1. NON-METALLIC INCLUSION ANALYSIS FROM AOD TO CENTRIFUGAL CASTING

Figure 3.1 compares the a) percentage area covered by inclusions and b) the total oxygen from the AOD to the final product (average of the three samples at x=0.25, x=0.50 and x=0.75) of the centrifugally cast steel products for the base heat A with no calcium addition, and calcium treated heats B, C, D and E. Note that there are only limited samples for some of the locations, but missing samples indicate neither an absence of inclusions nor an absence of oxygen in the steel during the casting process. The inclusion analysis at all stages of the calcium wire ladle treatment was only possible for heats B, D and E.

The area covered by oxides in the final product followed a similar trend to the total oxygen values. The total oxygen and inclusions were the highest in the AOD, dropped slightly after tap in the ladle and dropped further after calcium treatment. After the calcium wire ladle treatment, the total oxygen and inclusions were the lowest and remained lower in the final centrifugally cast product. However, the inclusion analysis in the lollipop samples reveals some deviation between the area covered by oxides and the oxygen levels collected at various stages of the melting procedure. The deviation is most likely a result of inconsistencies in inclusion distribution within the sampler mold influenced by turbulent filling and the solidification shrinkage, modifying the inclusion distribution in the lollipops [41].

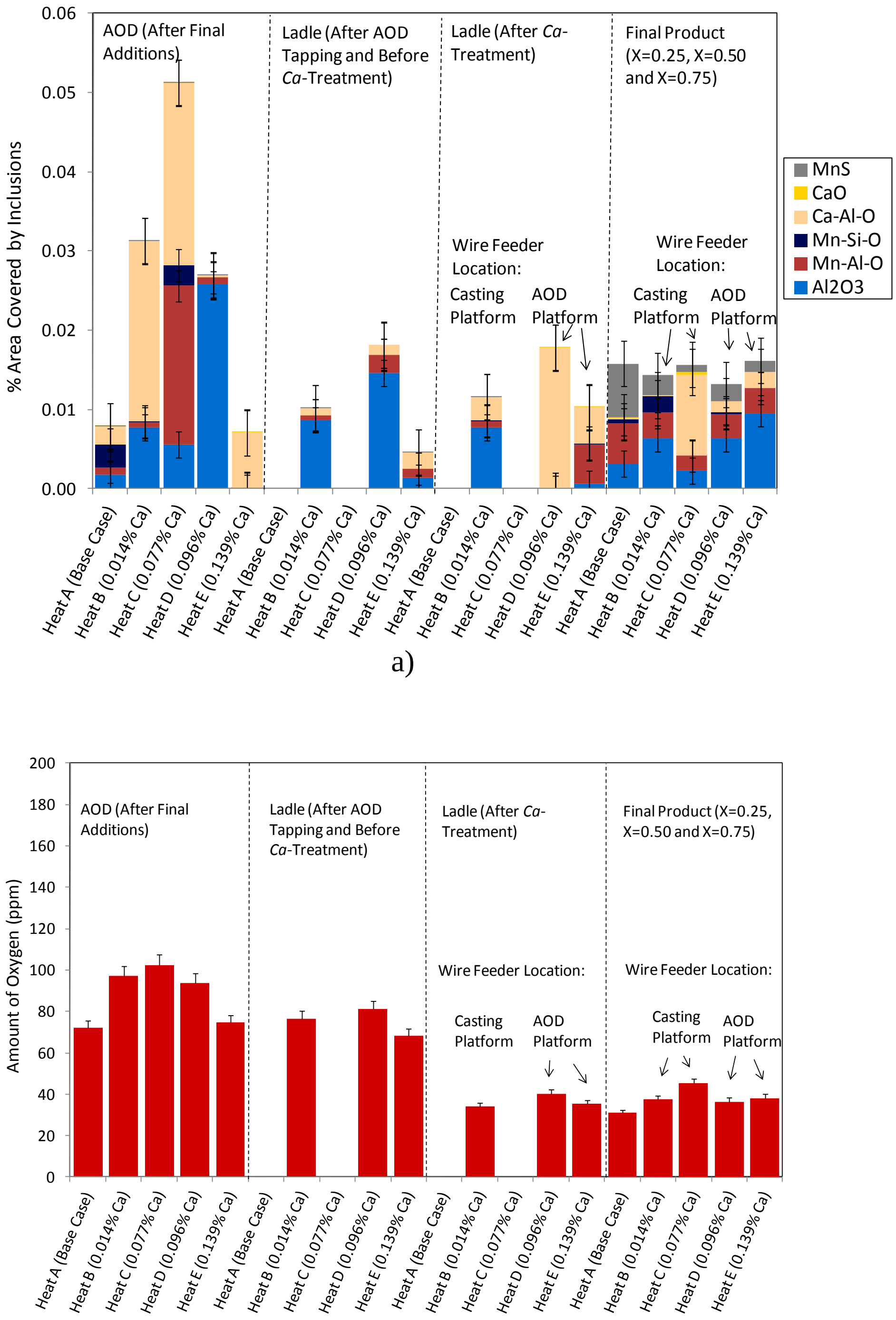

b)

Figure 3.1. Comparison of the a) percentage area covered by inclusions and b) the total oxygen measured in samples collected from the AOD to the final product for each experimental heat

The amount of oxides, especially the aluminum containing oxides, and the total oxygen regardless of calcium addition decreased from the AOD to the final product due to the natural inclusion flotation to the slag layer during the transfer ladle to the casting platform. The amount of oxides and the total oxygen in the final product for the base heat A is slightly less than the calcium treated heats B, C, D and E. This could be a combination of a larger ladle size for heat A (14,264 lb), the largest during the experiments, improving inclusion flotation, and the highest G forces in the experiments [9]. However, the calcium treated heats B, C, D and E show few Mn-rich inclusions in comparison to the base heat A, indicating that the calcium treatment improved the desulfurization process in the molten steel. The reaction of calcium sulfide formation is given by Eq. 21.

$$3S + 3CaO + 2Al \rightarrow 3CaS + Al_2O_3 \tag{21}$$

Heats B (0.014 $\%Ca$) and C (0.077 $\%Ca$) were calcium fed just prior to casting. Heat B reveals that the low amount of calcium added in the ladle had a minor effect on the inclusion composition in the final casting. Heat C exhibits a different inclusion trend in comparison to the no Ca treated heat A. The inclusion modification in heat C shows that even though there was a significant amount of non-metallic inclusions after the final additions in AOD, Al_2O_3 and Mn-Al-O inclusions in the final product were reduced by a factor of five in comparison to heat A. However, heat C demonstrates that there was a large amount of calcium aluminates in the final product due to insufficient time for inclusion flotation after calcium treatment (total time after calcium treatment and prior to pouring into a flask mold= 2 min 38 s).

Heats D (0.096 $\%Ca$) and E (0.139 $\%Ca$) were calcium fed just after AOD tapping. Low melting point calcium aluminates were the main type of inclusions after the calcium wire ladle treatment in heats D and E. Heat D shows that the oxide inclusion distribution in the final product was similar to heat B and slightly higher than heat A. The amount of oxide inclusions in heat E in the final product was similar to heat C and higher than the base heat A and calcium treated heats B and E. This implies that the Al_2O_3 and Mn-Al-O inclusions in the centrifugally cast tube samples were not significantly modified by the calcium wire ladle treatment, suggesting that its effectiveness was reduced due to re-oxidation during the pouring and melt transport through the pouring basin.

The area of MnS inclusions in the earlier stages of the casting process regardless of calcium addition is significantly less than the final centrifugally cast products. The probability of MnS formation during the melting process was reduced for all heats due to the low sulfur content after final additions in the AOD (0.001%S). Furthermore, the inclusion analysis may underestimate the MnS inclusions in the melting procedure due to their small size, suggesting that the molten steel solidifies immediately after it comes in contact with the walls of the lollipop-shaped samples and reduces the growth of MnS at high cooling rates. MnS inclusions in the centrifugally cast products were formed during solidification because Mn and S are typically rejected from the solidifying dendrites, increasing their concentration in the remaining liquid. The concentration of Mn and S leads to the precipitation of MnS towards the end of the solidification process.

3.2 NON-METALLIC INCLUSION DISTRIBUTION IN CENTRIFUGALLY CAST STEEL PRODUCTS

Theoretically, non-metallic inclusions, which are lower density than molten steel, should be pushed to the inside diameter by centrifugal force. However, Figure 3.2 indicates that the inclusion volume at the inside diameter of the test heats was not greater than the other areas of the tube. These samples were taken from the opposite end of the tube from pouring, an area that Mirzoyan and Pavperova had found in their research resulted in less flotation of inclusions because the temperature was 104- 140 °F lower than the pouring end, producing solidification entrapment of inclusions (Figure 1.10 in Section 1.2.1.3) [18].

The large amount of non-metallic inclusions at the OD may be due to the presence of exogenous inclusions from both re-oxidation and refractory erosion. The initial metal filling of the mold is highly turbulent and violently exposed to air as it travels the length of the mold, forming massive re-oxidation inclusions. Inclusions are also formed when an uneven refractory lining is eroded and infiltrated by the molten steel, re-oxidizing pre-existing particles that form new inclusions [1], [14]. Both of these types of inclusions are pushed to the end of the mold opposite pouring and may be trapped due to lower temperatures and rapid freezing of the mold. Once new metal enters, it does not have those two sources of inclusions in the first metal filling the mold.

Figure 3.2 also reveals that the area of Al_2O_3 and $Mn\text{-}Al\text{-}O$ inclusions in the final product remained almost constant for all heats, indicating that these types of inclusions were not significantly modified by the calcium wire ladle treatment. The effectiveness of the calcium treatment may be reduced by re-oxidation during the pouring and melt transport through the pouring basin.

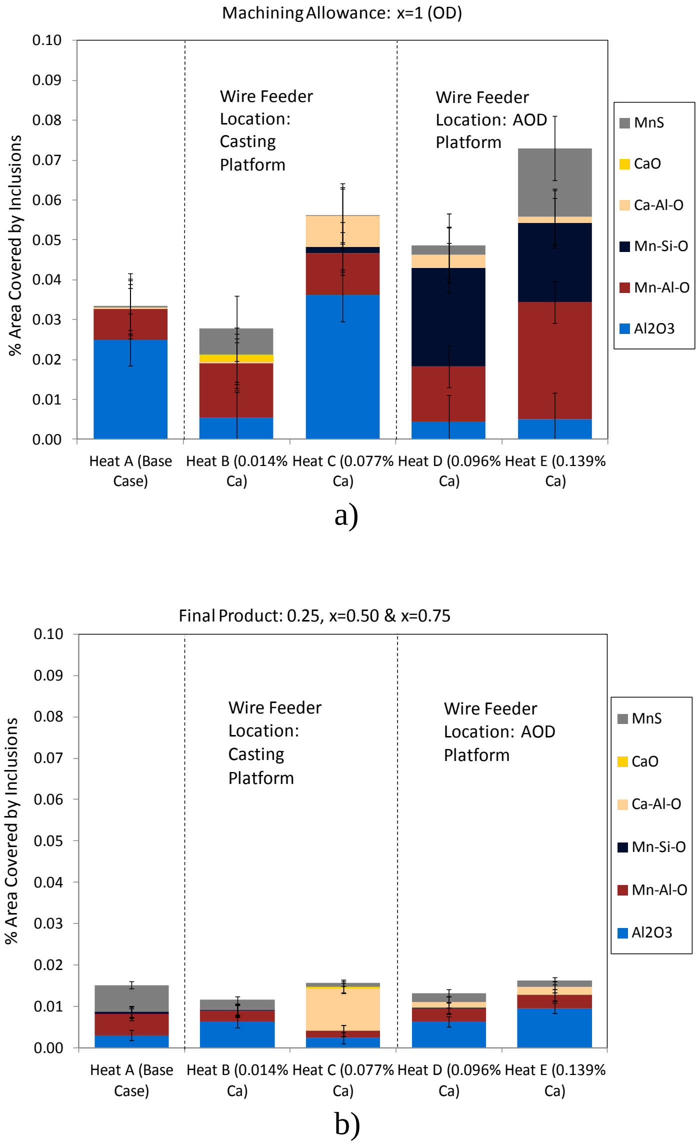

Figure 3.2. Percentage area covered by inclusions at different locations in the cast tube samples taken from the opposite pouring end of the finished tubes for each experimental heat

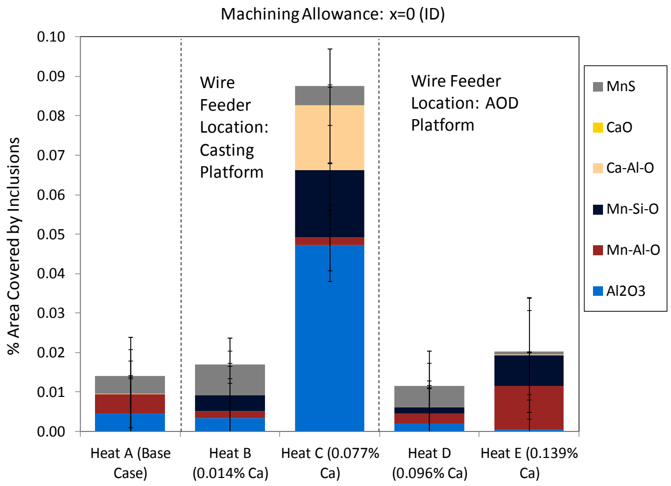

c)

Figure 3.2. Percentage area covered by inclusions at different locations in the cast tube samples taken from the opposite pouring end of the finished tubes for each experimental heat (cont.)

Figure 3.3a compares the amount of non-metallic inclusions in the centrifugally cast products for all heats. Generally, the amount of non-metallic inclusions in the final product was significantly less than the OD and slightly less than the ID. It was also observed that the inclusion distribution was practically uniform in the final product of the casting. Figure 3.3b verifies the inclusion results in Figure 3.3a. The total oxygen in the centrifugally cast steel products agreed with the volume of inclusions, implying that both inclusions and total oxygen content were mainly concentrated at the OD for all heats, except for heat C. In heat C, the calcium wire ladle treatment produced low melting point calcium aluminate inclusions, but since the wire was fed just prior to casting, there was insufficient time for inclusion flotation at the casting platform, resulting in a large amount of inclusions at different locations of the casting. Furthermore, the ladle size for heat C (8,835 lb, 4,007 kg) was the smallest in comparison to the rest of the heats (12,248 lb, 5,556 kg), reducing the effectiveness of inclusion flotation in the ladle [9].

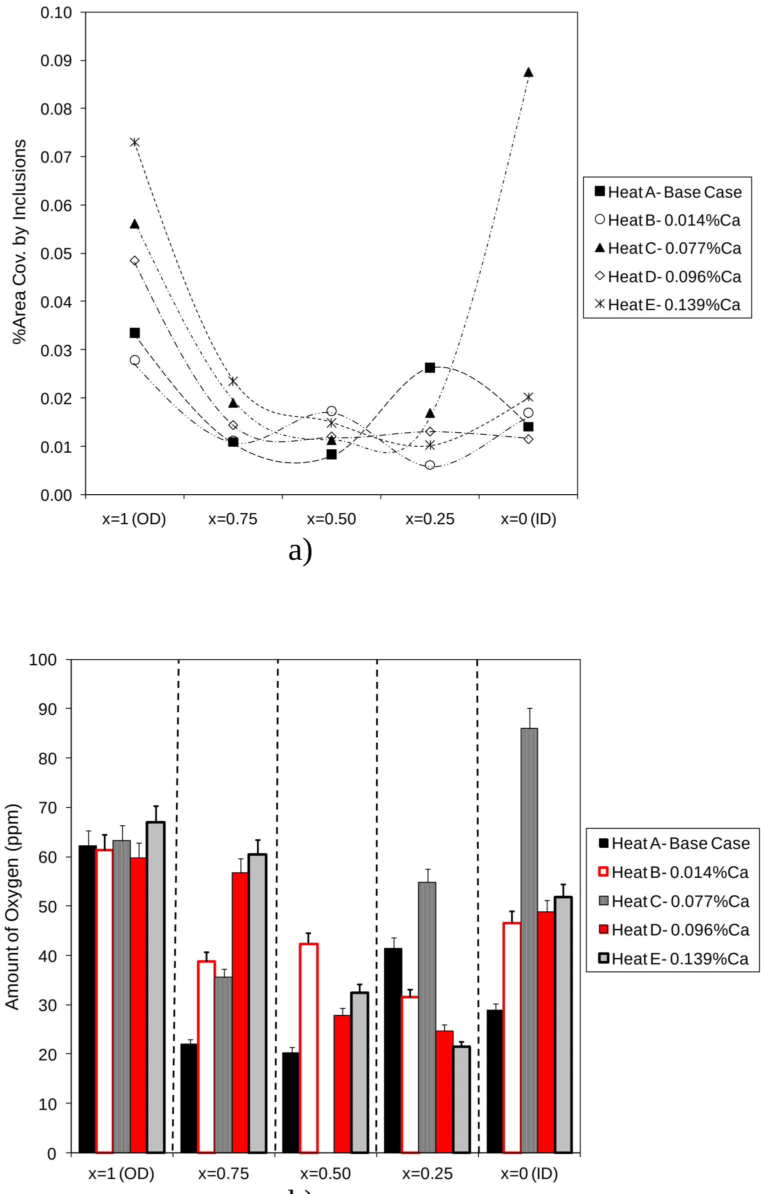

a)

b)

Figure 3.3. Average a) percentage area covered by inclusions and b) total oxygen from the OD to the ID of the centrifugally cast products for each experimental heat

3.2.1. Oxide and Sulfide Distribution in Centrifugally Cast Steel Products.

Figure 3.4 compares a) the average percentage area covered by oxides and sulfides and b) the average total oxygen for all centrifugally cast steel samples. The amount of oxide inclusions and total oxygen were the highest at the OD and almost as high at the ID. The OD results are higher than the ID because of the initial re-oxidation and rapid solidification entrapping inclusions before flotation from centrifugal forces. The oxides are concentrated at the ID due to centrifugal forces and direct contact with air. The amount of sulfide inclusions was relatively constant across the wall thickness of the centrifugally cast steel product, indicating that sulfides were formed near the liquidus temperature and inside the mushy zone, and therefore, eliminating the influence of the centrifugal forces during the dendrite solidification of the casting process.

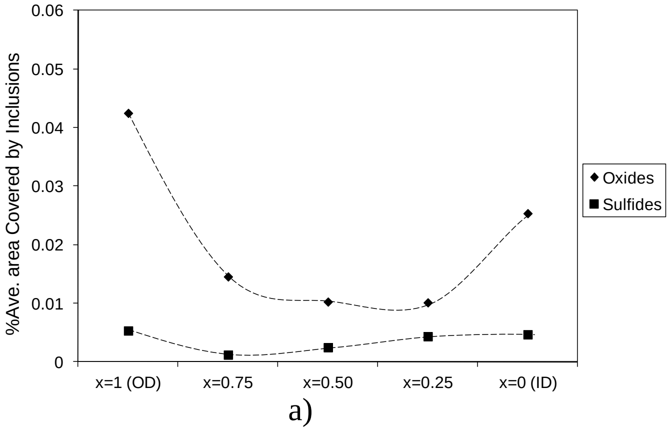

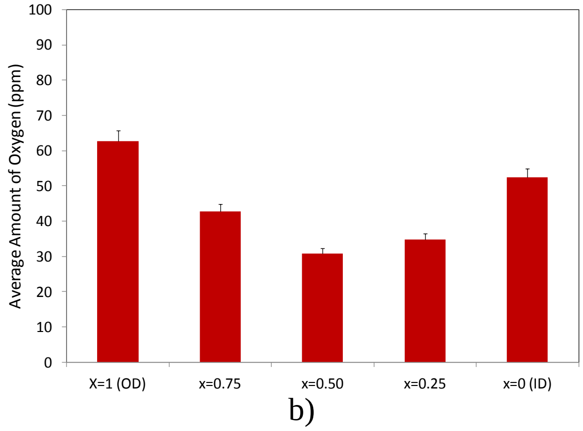

Figure 3.4. Average a) percentage area covered by oxides and sulfides and b) total oxygen from the OD to the ID of the centrifugally cast products for the five heats

Figure 3.5 shows that the inclusion size was less than 15μm regardless of the region in the centrifugally cast steel product. Figure 3.6a reveals that coarse inclusions were prone to be concentrated at the ID. This could be explained by the fact that intensive cooling occurred at the OD, producing a well defined solidification front, which captured smaller inclusions between dendrite arms and pushed larger inclusions into liquid. Large inclusions were forced through solidification and centrifugal forces towards the ID of the casting. Note that Figure 3.6b shows much larger inclusions in the base heat A with no calcium addition. Sulfides were smaller than oxides for the calcium treated heats. This shows some effectiveness of the calcium treatment in modifying and reducing the inclusion size in the centrifugally cast products.

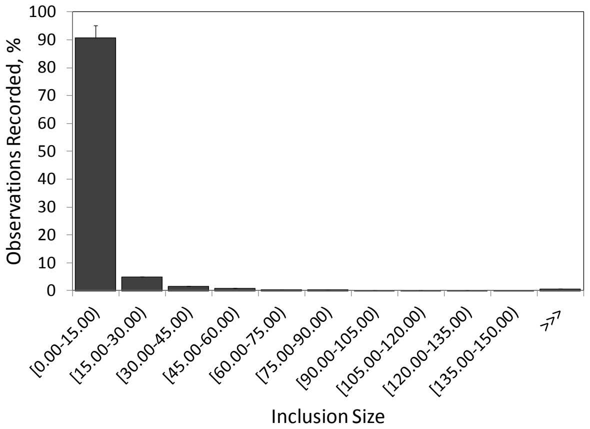

Figure 3.5. Average inclusion size distribution including the ID, OD and the final product for each experimental heat

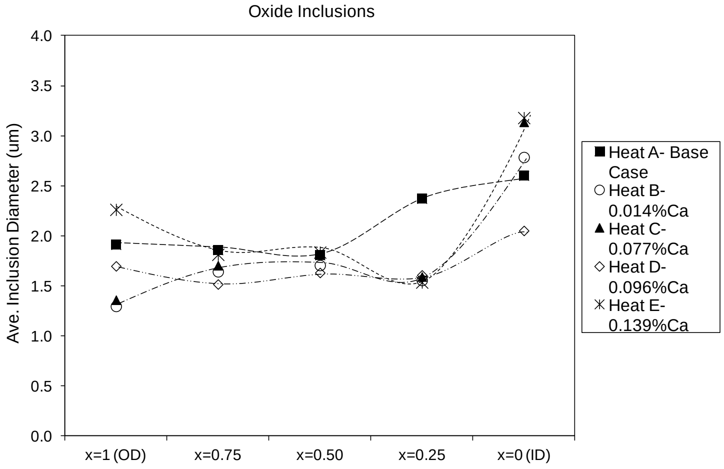

a)

Figure 3.6. Average inclusion diameter of a) oxides and b) sulfides in the centrifugally cast products for each experimental heat

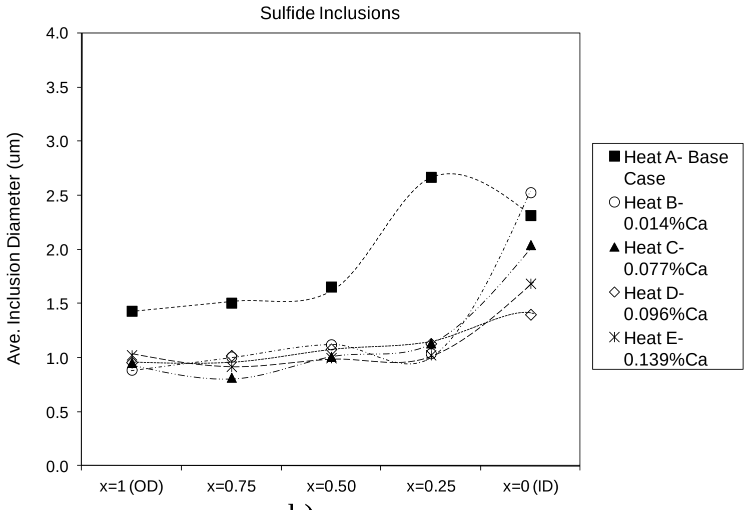

b)

Figure 3.6. Average inclusion diameter of a) oxides and b) sulfides in the centrifugally cast products for each experimental heat (cont.)

Figures 3.7 and 3.8 display the aspect ratio for each centrifugally cast steel product. The automated inclusion analyzer uses a rotating chord algorithm to find the center of an inclusion, drawing 16 chords through its center to determine the maximum and perpendicular diameter of each inclusion [9]. The aspect ratio is then calculated using the maximum diameter divided by the perpendicular diameter of each inclusion.

Figure 3.7 reveals that the inclusion shape of the Al_2O_3, *Mn-Al-O*, and *MnS* inclusions were fairly round throughout the wall thickness of the centrifugally cast product, but became more irregular towards the ID. The manganese silicate inclusions (*Mn-Si-O*) were far more irregular in shape at all locations, indicating more complexity. The inclusion shape for the *Ca-Al-O* became more round at the ID. The calcium addition in heats B, C, D and E would have helped in the inclusion modification of the centrifugally cast steel samples, but it was limited by the re-oxidation during pouring and transportation through the pouring basin. Furthermore, Figure 3.8 shows that the inclusion shape for heat C was less amorphous than the base heat A and calcium treated heats B, D and E, but the inclusion shape for the calcium treated D became more irregular than heat C towards the ID.

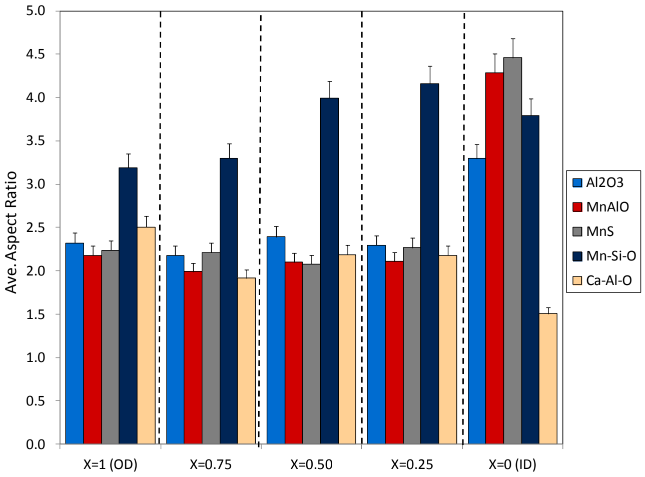

Figure 3.7. Average inclusion aspect ratio using different inclusion compositions from the OD towards the ID of the centrifugally cast products for each experimental heat

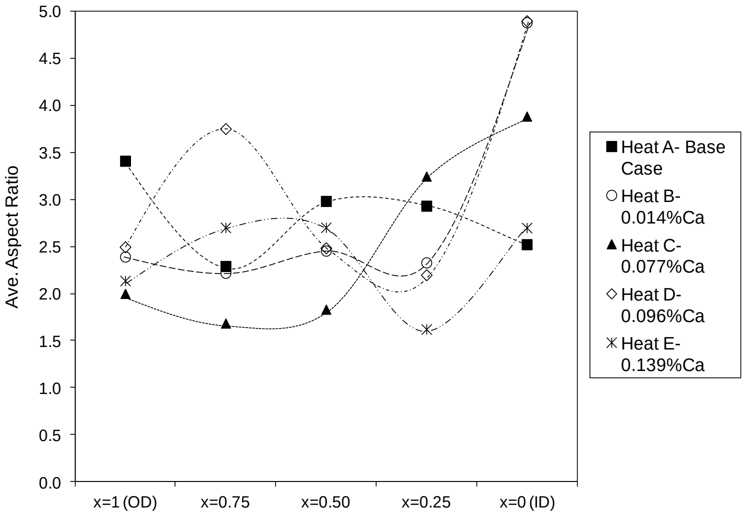

Figure 3.8. Average inclusion aspect ratio from the OD towards the ID of the centrifugally cast products for each experimental heat

3.2.2. Distribution of Inclusions Containing Nitrogen in Centrifugally Cast Steel Products. Figure 3.9 shows that the total nitrogen levels was significantly larger in the centrifugally cast products ($[N]_{Average}$= 141 ppm) than the total nitrogen content in the ladle (($[N]_{Average}$ = 80 ppm), indicating a 60 ppm nitrogen pickup from significant air contact during casting. The large amount of nitrogen pickup is due to the highly turbulent nature of the molten steel during casting and the constant air contact during solidification.

A high nitrogen level in steel raises the potential to precipitate nitrides, which are also important to the final mechanical properties.

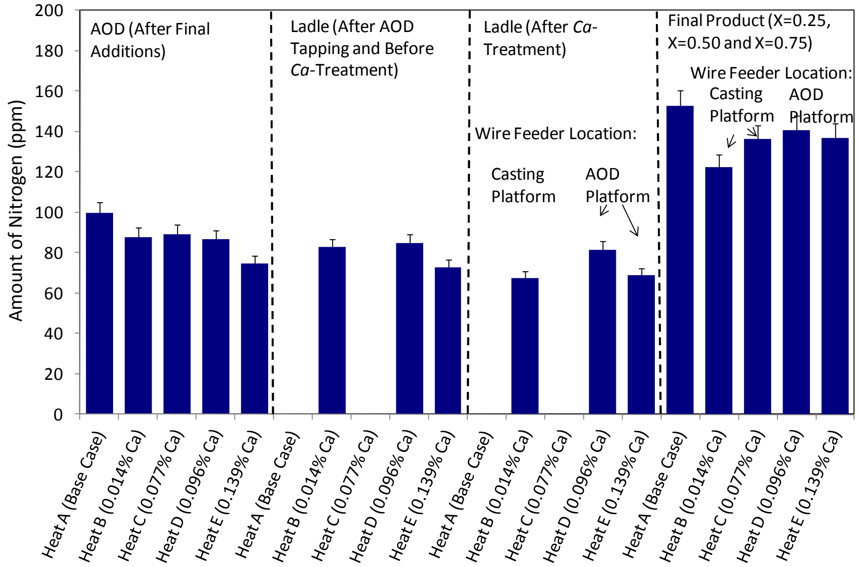

Figure 3.9. Total nitrogen measured in samples collected from the AOD to the final product for each experimental heat

Figure 3.10 exhibits a new series of inclusion analysis, which was completed for nitrides using an analyzed area of 0.819 mm^2 per specimen. A combination of complex oxides (MnO, Al_2O_3 OR Ca-Al-O) and aluminum nitrides, known as oxynitride inclusions, were found in the final product of the centrifugally cast steel products. The amount of oxinitrides for heats D and E (calcium fed just after AOD) was significantly larger than the base heat A and calcium treated heats B and C (calcium fed just prior to casting), which was not observed in the previous oxide and sulfide analysis. This means that the previous inclusion analysis might misclassify some oxynitrides as either oxide or sulfide inclusions, as well as it might neglect some oxynitrides in the final product.

Figure 3.11 shows that the oxynitride size regardless of calcium addition became larger towards the ID. Furthermore, the calcium wire ladle treatment did not modify the size of the oxynitride inclusions as compared to the oxides and sulfides in the centrifugally cast products.

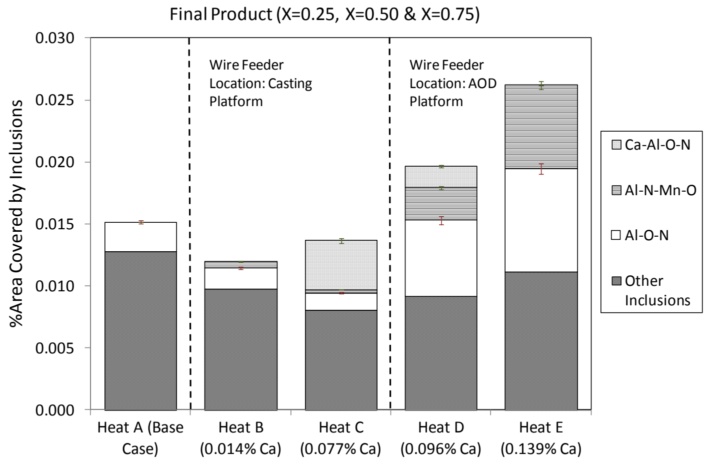

Figure 3.10. Percentage area covered by inclusions containing nitrogen and others in the final product of the centrifugally cast products for each experimental heat

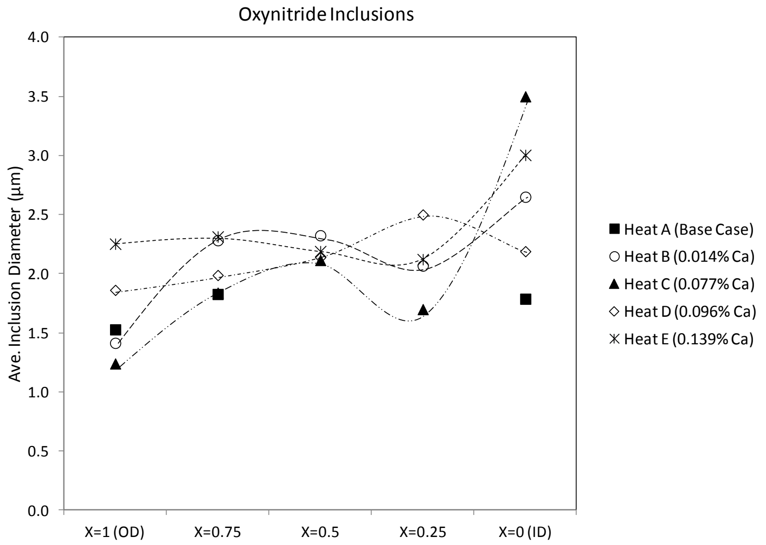

Figure 3.11. Average inclusion diameter of complex inclusions containing nitrogen (oxynitrides) in the centrifugally cast products for each experimental heat

3.3. NON-METALLIC INCLUSION SPACING IN CENTRIFUGALLY CAST STEEL PRODUCTS

Non-metallic inclusion spacing has a significant effect on the fracture toughness as shown in Eq. 2 in Section 1.2.1.The fracture toughness can be enhanced by increasing the inclusion spacing, minimizing the nucleation and growth of pre-existing cracks or void-like imperfections [8]. The inclusion spacing in the centrifugally cast steel products for each experimental heat was determined using the inclusion coordinates provided by the Aspex and a Visual Basic Code.

In previous research, the Visual Basic Editor in Microsoft Excel was used to create a program/ code to run a set of instructions in a specific order to calculate the inclusion spacing in castings. The Visual Basic code is given in Appendix A. A macro was then enabled in Excel to automatically calculate the inclusion distance to the closest neighbor and inclusion spacing using the inclusion coordinates exported from Aspex. The inclusion distance was averaged over all inclusions to calculate the average inclusion spacing for the centrifugally cast steel products.

Figure 3.12 shows that the inclusion spacing in the centrifugally cast steel products was fairly stable with a slight trend to increase from the OD to ID, except for heat C. Heat C exhibited more variation in the inclusion spacing, especially at the ID and x=0.75. Figure 3.13 compares a) the average percentage area covered by the inclusions and b) the average inclusion spacing for all heats. Generally, the area covered by inclusions was indirectly proportional to the spacing between inclusions, implying that the inclusions were closer to each other if the volume of inclusions increased in steel. For example, the OD had significantly closer spacing inclusion and was the dirtiest area, showing the highest percentage area covered by inclusions. Ideally, clean steel entails the least number of inclusions and the largest inclusion spacing in castings. However, the size of inclusions is generally larger at the ID, resulting in a larger spacing with relatively large amount of inclusions.

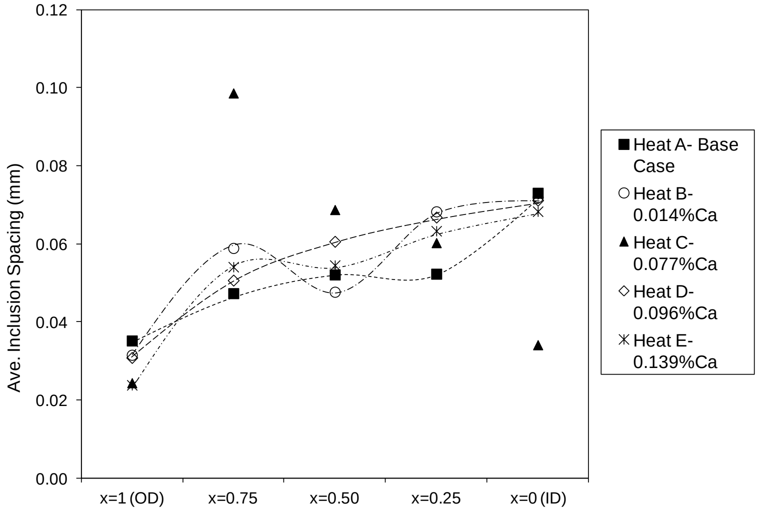

Figure 3.12. Average inclusion spacing in the centrifugally cast steel products for each experimental heat

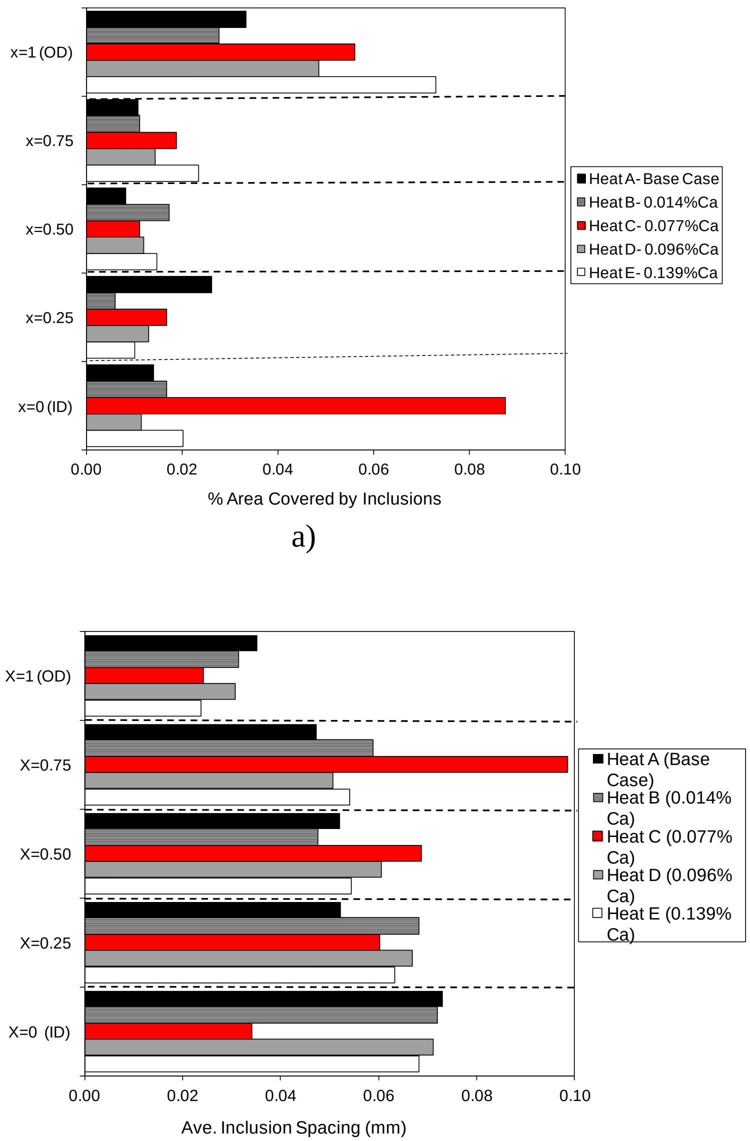

a)

b)

Figure 3.13. Comparison of a) the average percentage area covered by inclusions and b) the average inclusion spacing in the centrifugally cast steel products for each experimental heat

3.4. POROSITY IN CENTRIFUGALLY CAST STEEL SAMPLES

3.4.1 Interdendritic Porosity in Centrifugally Cast Steel Products. Figure 3.14 shows the typical morphology of porosity at x=0.25 in the final product of the casting, suggesting that this defect formed in the interdendritic residual liquid of the casting. Interdendritic porosity is produced when molten steel channels are formed between the dendrite arms during freezing, restricting its flow in the casting. The molten steel channels are small and extensive at the end of the network freezing, resulting in shrinkage in which the feeding of the molten steel through the interconnected network becomes difficult, and therefore, small pores appear near the roots of the dendrites arms [42].

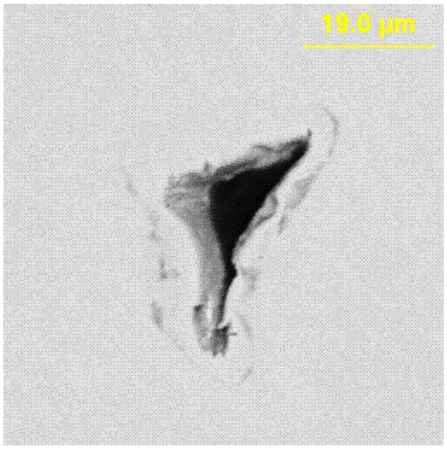

Figure 3.14. Aspex/ SEM image showing the typical morphology of porosity at x=0.25 in the final product of the centrifugally cast samples

Figure 3.15 shows that the average area covered by porosity regardless of calcium addition in the final product was significantly less than both the OD and ID. The large amount of porosity at the OD might be influenced by the combined effects of shrinkage and gas evolution in the casting. Theoretically, gas porosity involving hydrogen, oxygen, nitrogen or carbon monoxide in the centrifugally cast products may be influenced by the moisture retained in the mold coating, resulting in gas formation when the mold coating comes in contact with the hot metal [1]. The molten steel at the OD was then subjected to rapid solidification, resulting in a chill zone where equiaxed grains did not allow pushing of gasses in the interdendritic residual liquid of the casting.

Figure 3.16 shows the porosity diameter in the centrifugally cast steel products with a slight trend to increase from the OD to ID. The porosity size at the OD was the smallest, impeding the growth of the gas pores due to the small dendrite arm spacing (DAS) at high cooling rates in the chill zone [20]. The growth of the dendrites occurred towards the ID due to a slow solidification rate, resulting into wider dendrite arm spacing (DAS) during solidification.

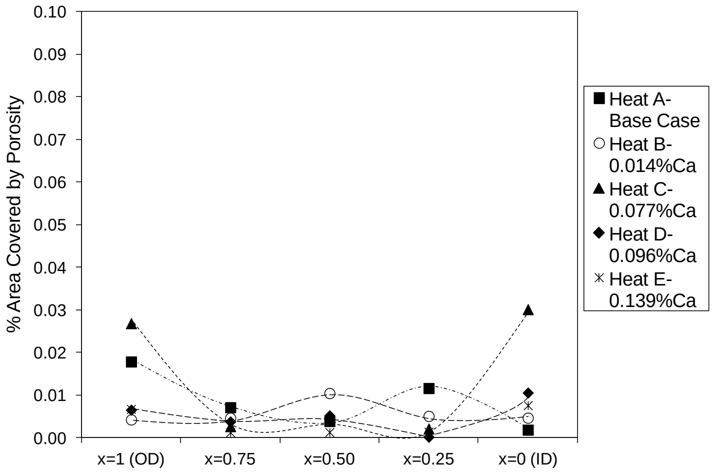

Figure 3.15. Average percentage area covered by porosity in the centrifugally cast products for each experimental heat

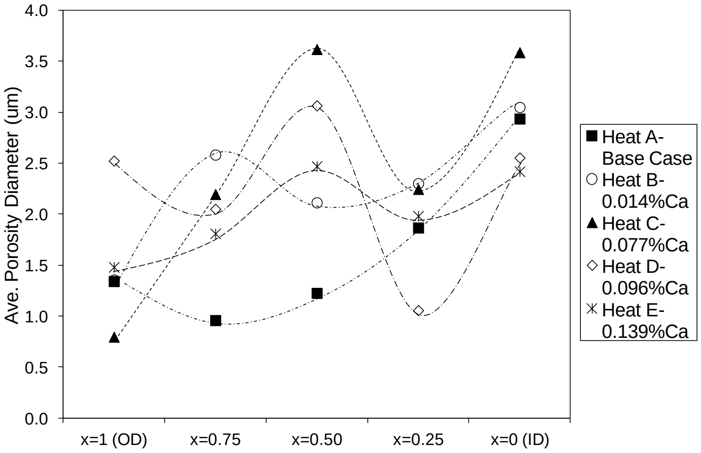

Figure 3.16. Average porosity diameter in the centrifugally cast products for each experimental heat

3.4.2. Shrinkage Porosity in Centrifugally Cast Steel Products. Figure 3.17 shows that porosity in the centrifugally cast products became more irregular towards the ID of the casting, indicating interdendritic porosity. In addition, visible porosity was detected only at the ID of the centrifugally cast steel products, which was examined using a stereoscope for low magnification purposes (Figure 3.18). In Figure 3.18, macro-porosity was observed, especially for heats B, D and E. Figures 3.19 and 3.20 reveal that this type of macro-porosity at the ID was related to shrinkage cavities, indicating that the ID solidified last and the molten steel was insufficient at this location. This means, the combined effects of high levels of gases and lower centrifugal forces to fill molten steel between dendrites produced shrinkage porosity at the ID. The high levels of gases at the ID is due to the reduced solubility of gasses as the molten steel freezes, producing regions of segregation of gaseous solutes in the casting. Dendritic segregation, or coring, was also identified surrounding the shrinkage porosity, demonstrating that alloying elements were rejected to the dendrite arms during solidification [43]. Theoretically, the depth of shrinkage porosity can be minimized by increasing the rotation speed during centrifugal casting [1], [21].

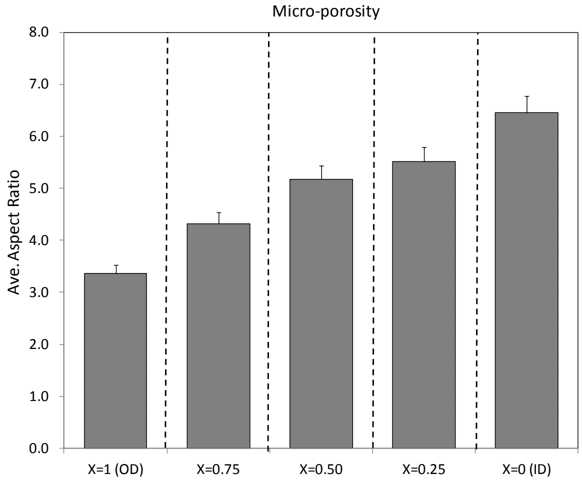

Figure 3.17. Average aspect ratio of porosity in the centrifugally cast products for each experimental heat

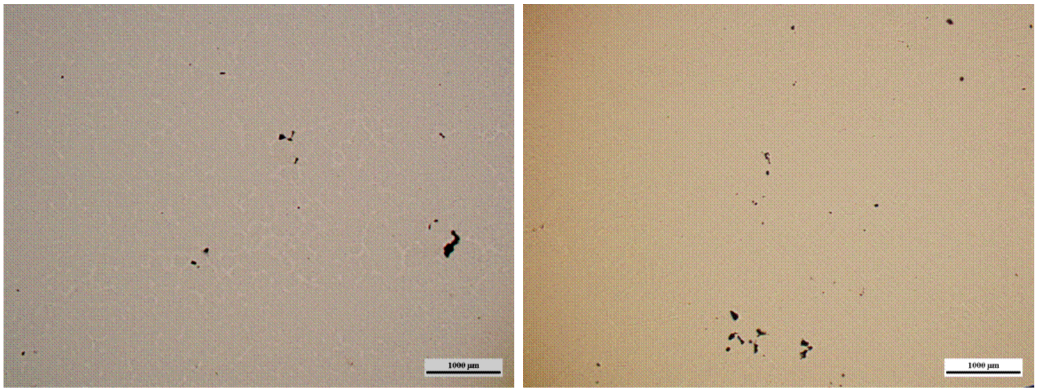

a) b)

Figure 3.18. Stereographs of the ID (X=0) of the centrifugally cast products showing visible porosity for a) the base heat A and calcium treated heats b) B, c) C, d) D and E in the un-etched condition

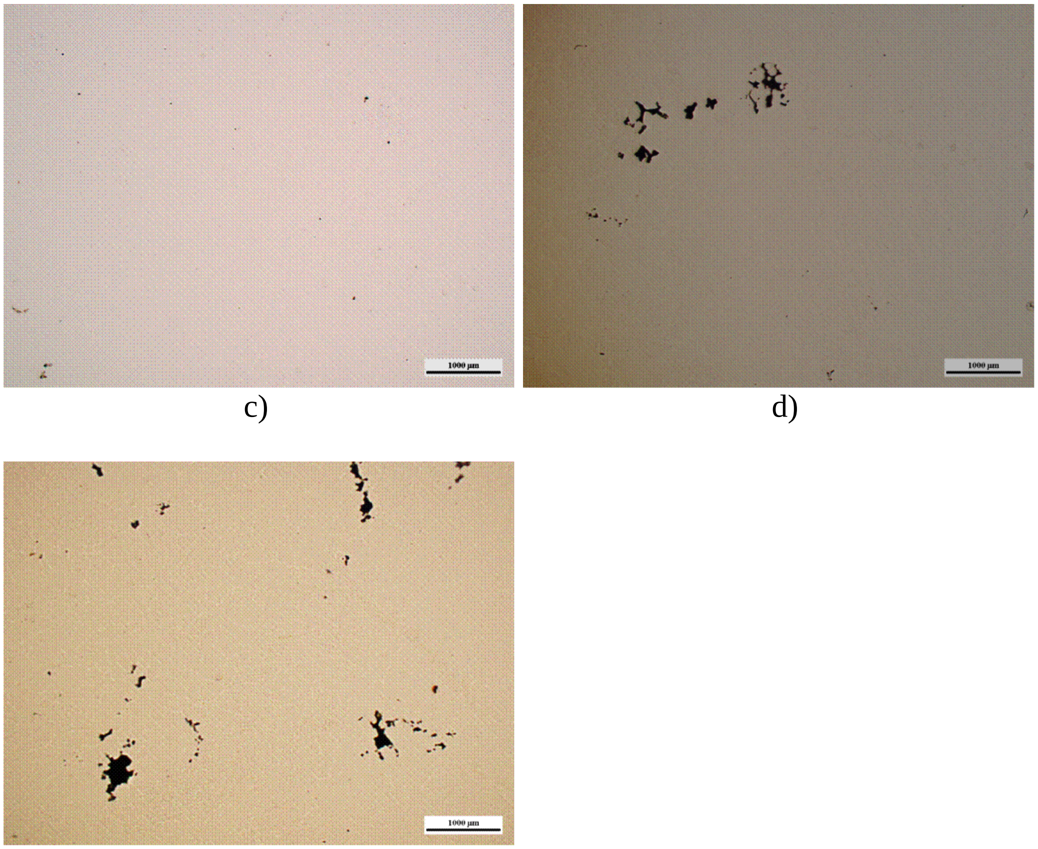

c) d)

e)

Figure 3.18. Stereographs of the ID (X=0) of the centrifugally cast products showing visible porosity for a) the base heat A and calcium treated heats b) B, c) C, d) D and E in the un-etched condition (cont.)

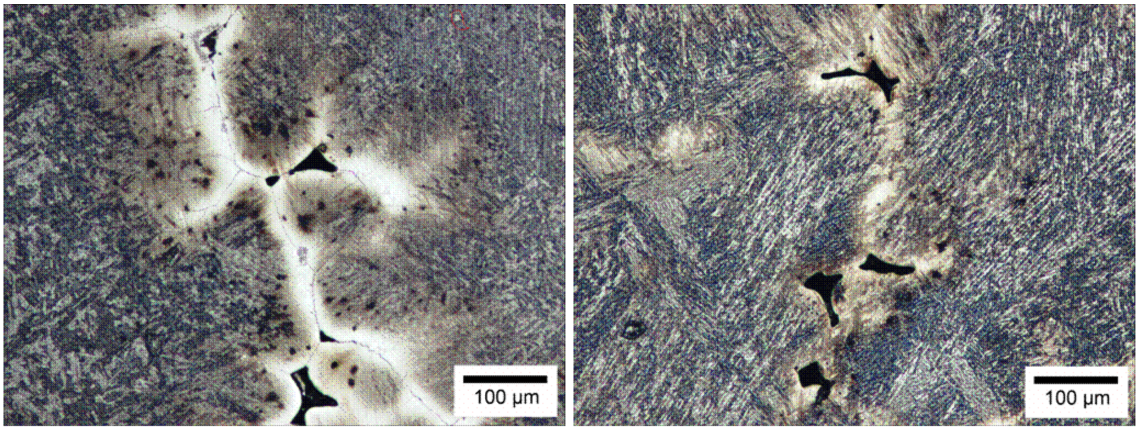

a) b)

Figure 3.19. Micrographs of the ID (X=0) in the centrifugally cast products showing visible porosity for the calcium treated heats a) D and b) E

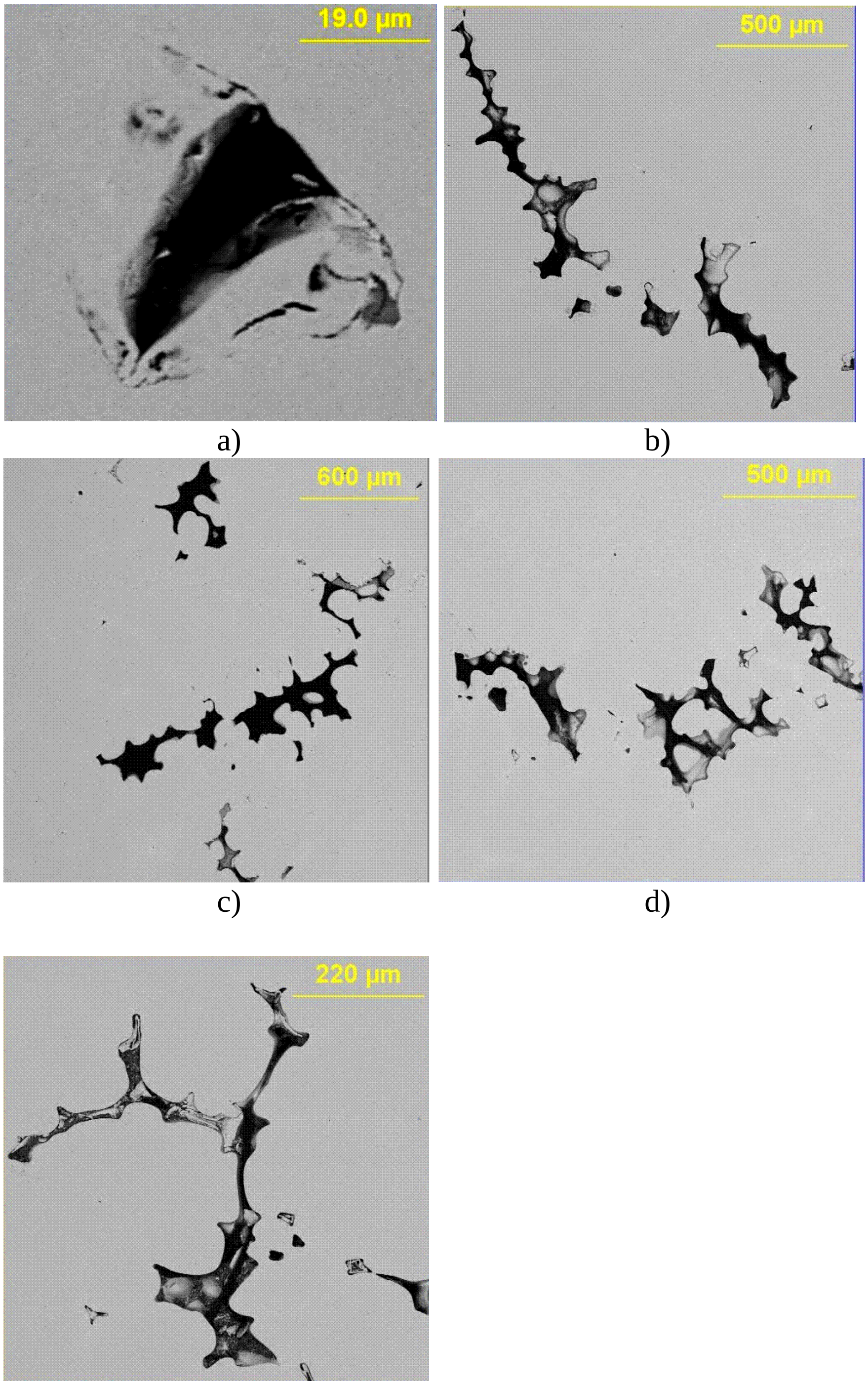
19.0 µm
500 µm
600 µm
500 µm
220 µm

a)
b)
c)
d)
e)

Figure 3.20. Aspex SEM image of the ID (X=0) in the centrifugally cast products revealing shrinkage porosity for a) the base heat A (2500X) and calcium treated heats b) B (100X), c) C (75X), d) D (100X) and e) E (220X)

3.5 MICROSTRUCTURES IN CENTRIFUGALLY CAST STEEL PRODUCTS

Figure 3.21 shows the typical microstructure of the centrifugally cast steel products, which consisted of lath martensite. Figure 3.22 displays the microstructure after the heat treatment based on ASTM A-487, showing tempered martensite in the final product.

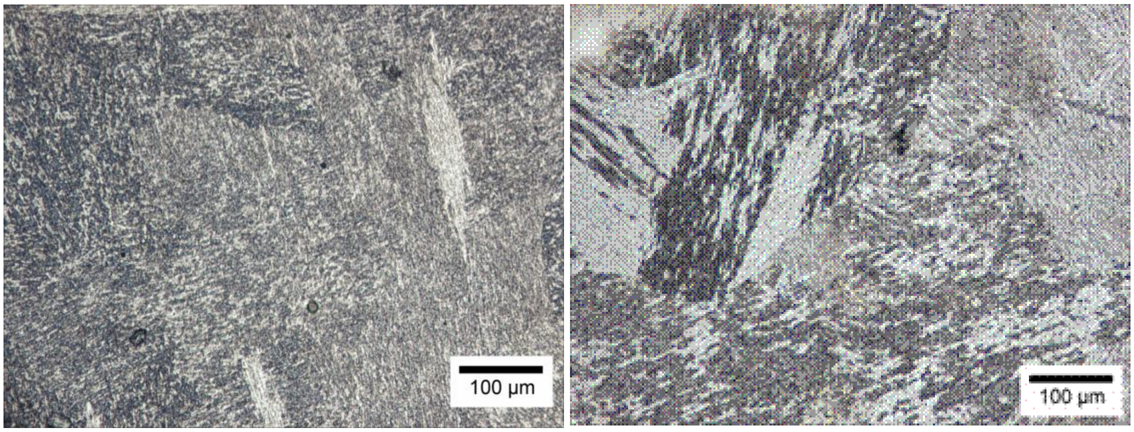

a) b)

Figure 3.21. Micrographs of the OD (X=1) in the centrifugally cast steel for heats a) B and b) C showing lath martensite

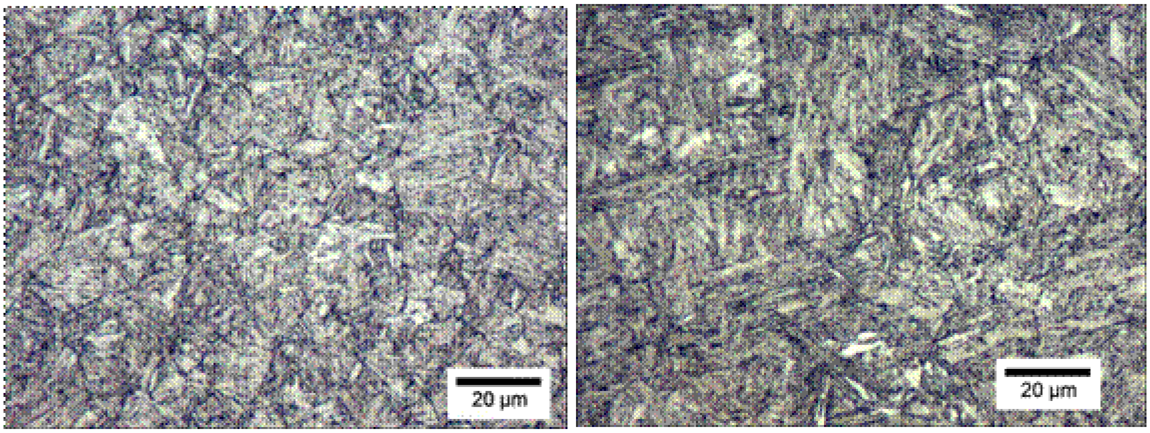

a) b)

Figure 3.22. Micrographs of the OD (X=1) in the centrifugally cast products for heats a) A and b) D showing tempered martensite after heat treatment

3.6. CHARPY IMPACT TESTING

Three Charpy V-notch specimens were sectioned from the final product of each experimental heat. Each Charpy specimen was tested at room temperature after heat treatment. Figure 3.23 shows that the Charpy values are all approximately the same at the upper shelf, indicating that the calcium wire ladle treatment did not significantly modify the inclusions containing aluminum, and therefore, the mechanical properties of the centrifugally cast steel samples were not improved either.

Oxynitrides inclusions may reduce the mechanical properties in the final product, but the toughness for the base heat A ([N] = 153 ppm) with the highest nitrogen level in the final product is similar to heats B and C ($[N]_{Average}$ = 130 ppm) and better than heats D and E ($[N]_{Average}$ = 139 ppm), implying that small differences in the volume of oxynitrides did not significantly influence on the mechanical properties of the centrifugally cast products. However, castings with a much lower nitrogen level with less oxynitrides could perform differently.

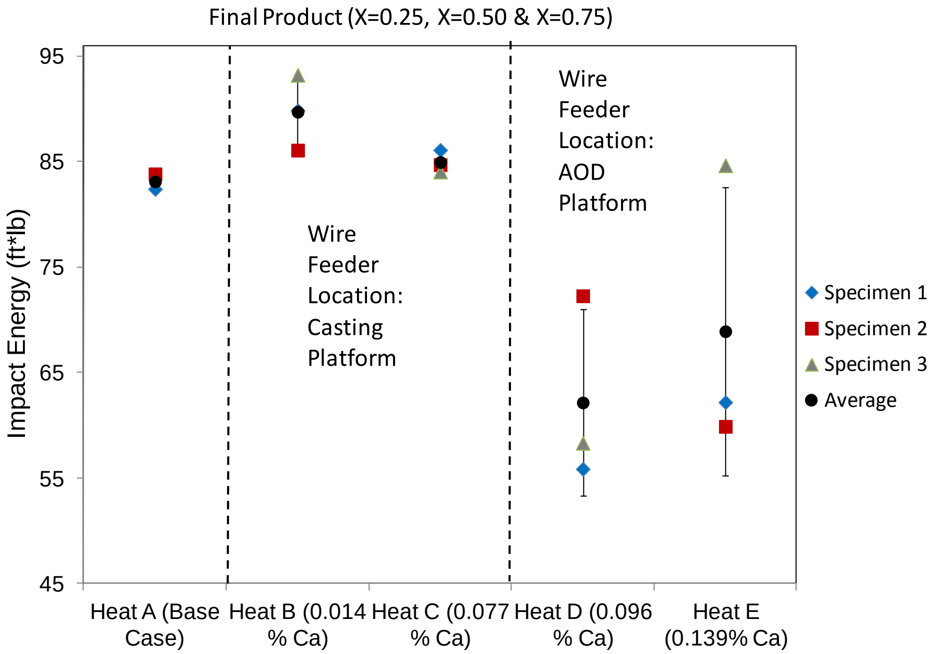

Figure 3.23. Charpy impact energy absorbed at room temperature for the base heat A and calcium treated heats B, C, D and E

3.7. FRACTOGRAPHY

Fractography was used to analyze the fracture mode and non-metallic inclusions, including their morphology and type, after impact testing. The fracture behavior for all heats was ductile with an accompanying degree of large plastic deformation. However, fracture surfaces of the final product at X=0.5 from heats B and E were examined because the impact values in the final product were the highest for heat B (86.1 ft*lb) and the lowest for heat E (59.9 ft*lb).

Fracture surfaces of the final product from heat B are shown in Figures 3.24 through 3.28. It was observed that most of the fracture mode in this alloy was ductile with few areas of intergranular fracture. The intergranular fracture in Figure 3.24 was due to the precipitation of complex γ-aluminum oxynitrides along the grain boundaries, causing high levels of stress concentration within the matrix under loading conditions. The volume of γ-aluminum oxynitrides may be reduced by lower nitrogen levels, resulting in better mechanical properties in castings. Figure 3.25 exhibits a cluster of alumina inclusions, which were most likely produced during re-oxidation of steel in pouring and transportation through the pouring basin [44]. Figures 3.26, 3.27 and 3.28 display non-metallic inclusions (MnO, Al_2O_3 and MnS) and porosity in a ductile dimple fracture. The inclusions and porosity in the steel dimples are prone to decohere within the matrix, promoting crack nucleation and propagation [8].

The inclusion type and morphology near the fracture surface of the final product from heat E are shown in Figures 3.29 through 3.33. Figures 3.29, 3.30 and 3.31 reveal inclusion clusters, in which the majority of the inclusions were alumina. The alumina inclusions contained traces of MgO and CaO, suggesting the alumina inclusions combined with the lining refractory and/ or ladle slag during the melting and/ or casting process. Figure 3.32 shows almost spherical holes or porosity that might be created due to the escape of gas bubbles, especially N_2 and CO, during the solidification process [44]. Figure 3.33 exhibits MgO-Al_2O_3 and Al_2O_3 inclusions along the boundaries of the former air bubbles, indicating that the Al_2O_3 may form with bubbles from oxidation of dissolved aluminum by oxygen with CO bubble.

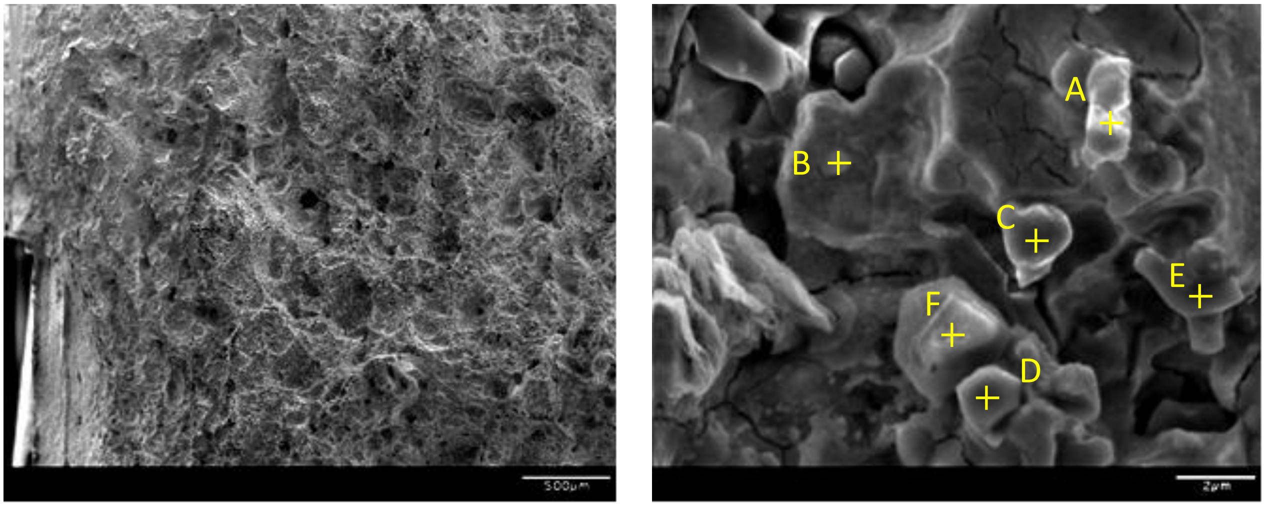

a) b)

Wt%	Al_2O_3	AlN	MnO	MgO	CaO
A	55.4	44.6	-.-	-.-	-.-
B	77.2	-.-	22.8	-.-	-.-
C	100	-.-	-.-	-.-	-.-
D	73.3	22.8	-.-	1.3	2.7
E	55.4	44.6	-.-	-.-	-.-
F	26.3	21.2	-.-	19.9	58.6

c)

Figure 3.24. Fracture surface of the final product (X=0.5) of the centrifugally cast steel tube from Heat B (0.014 %Ca) revealing that the fracture in this alloy occurs almost completely by microvoid coalescence, but close examination shows a few areas of intergranular fracture and complex inclusions (Al_2O_3-AlN, MnO-Al_2O_3, CaO-Al_2O_3-AlN) a) 45X b) 9500X

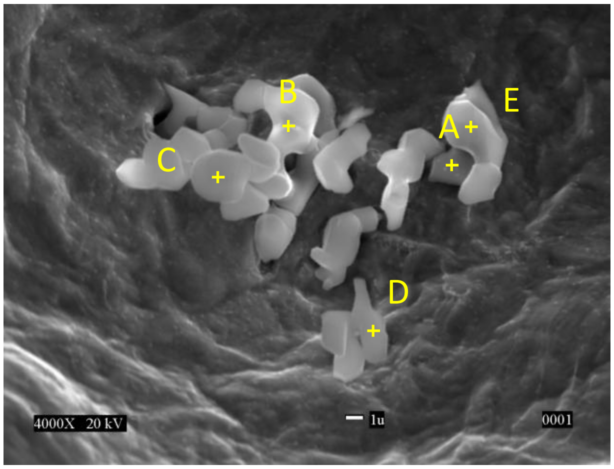

Wt%	Al_2O_3	MnS
A	27.9	72.1
B	71.4	7.3
C	100	-.-
D	100	-.-
E	93.2	6.8

a) b)

Figure 3.25. Fracture surface of the final product (X=0.5) of the centrifugally cast steel tube from Heat B (0.014 *%Ca*) showing Al_2O_3 and Al_2O_3-MnS clusters at 4000X

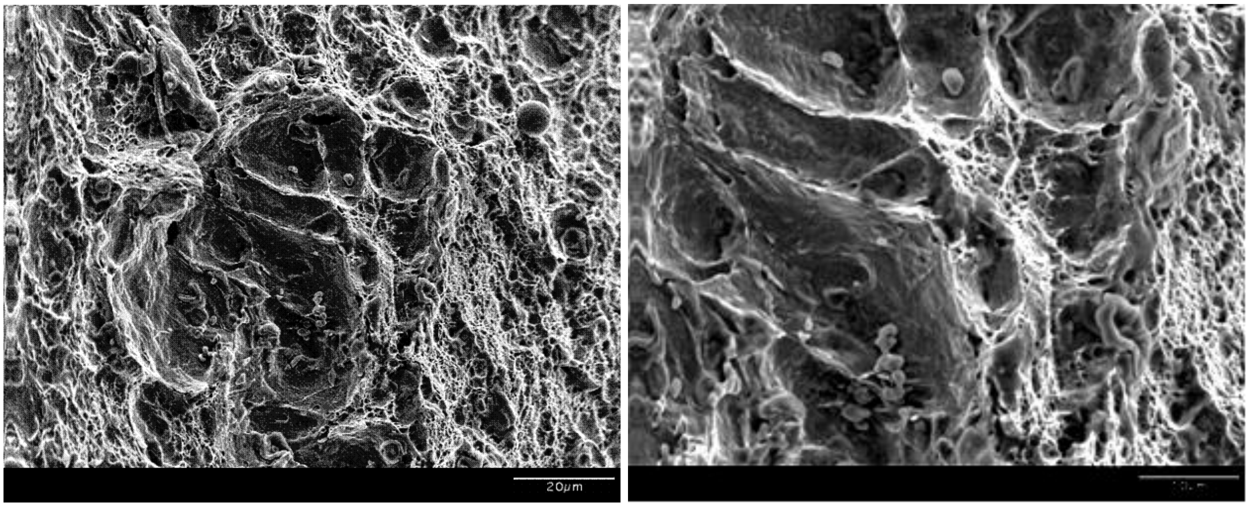

a) b)

Figure 3.26. Fracture surface of the final product (X=0.5) of the centrifugally cast steel tube from Heat B (0.014 *%Ca*) showing inclusions in a ductile dimple fracture a) 1500X b) 3000X

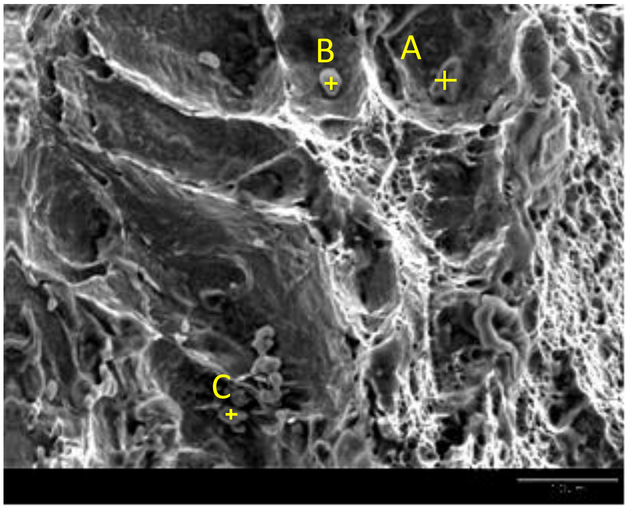

Wt%	MnO	MnS	Al_2O_3
A	100	-.-	-.-
B	-.-	100	-.-
C	-.-	-.-	100

a) b)

Figure 3.27. Fracture surface of the final product (X=0.5) of the centrifugally cast steel tube from Heat B (0.014 *%Ca*) revealing the chemical composition of inclusions (*MnO*, *MnS* and Al_2O_3) in a ductile dimple fracture at 3000X

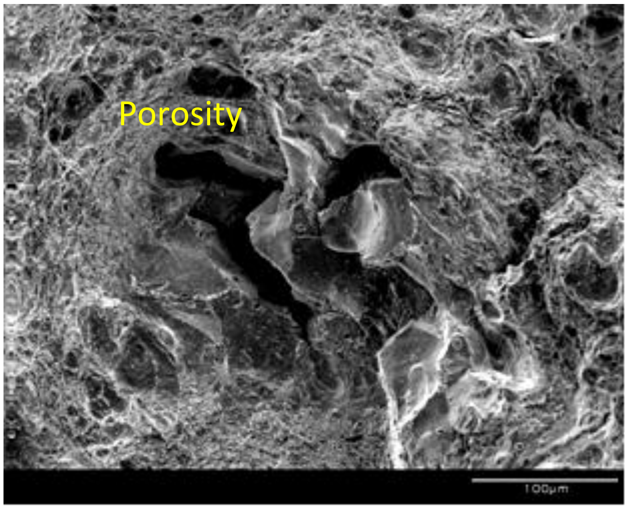

Figure 3.28. Fracture surface of the final product (X=0.5) of the centrifugally cast steel tube from Heat B (0.014 *%Ca*) exhibiting porosity and equiaxed dimples at 300X

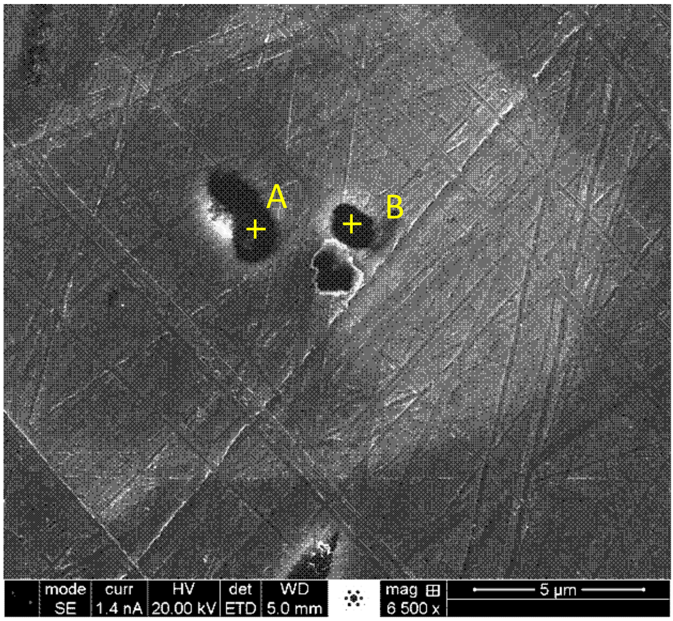
A
B
mode SE
curr 1.4 nA
HV 20.00 kV
det ETD
WD 5.0 mm
mag 6 500 x
5 µm

Wt%	Al_2O_3	CaO	MnS	MnO	MgO
A	68.7	9.0	19.9	-.-	2.4
B	94.6	3.0	- . -	-.-	2.4

a) b)

Figure 3.29. Centrifugally cast steel sample from the final product (X=0.5) of Heat E (0.139 *%Ca*) revealing the chemical composition of non-metallic inclusions (Al_2O_3-*MnS*, Al_2O_3) in a steel matrix

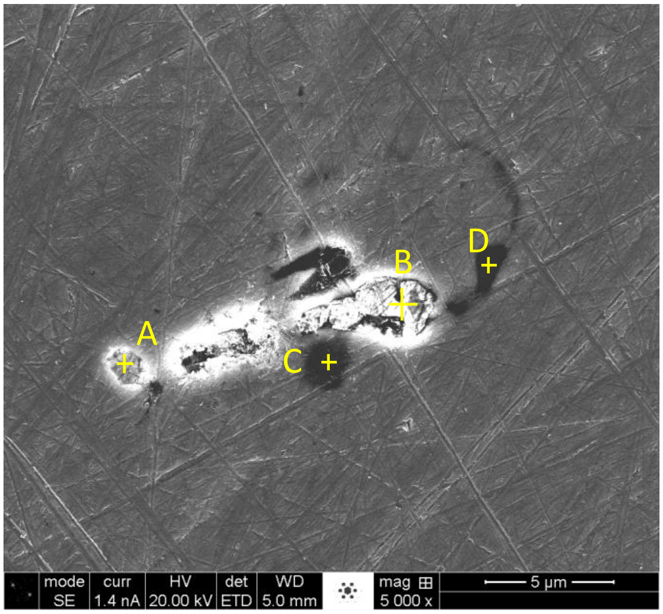
A
B
C
D
mode SE
curr 1.4 nA
HV 20.00 kV
det ETD
WD 5.0 mm
mag 5 000 x
5 µm

Wt%	Al_2O_3	MnS	MgO	MnO	TiO_2	SiO_2
A	78.0	-.-	20.6	1.4	-.-	-.-
B	98.1	-.-	1.2	0.7	-.-	-.-
C	97.4	-.-	-.-	1.4	1.2	-.-
D	22.3	72.7	-.-	-.-	-.-	2.8

a) b)

Figure 3.30. Centrifugally cast steel sample from the final product (X=0.5) of Heat E (0.139 *%Ca*) showing inclusion clusters in a steel matrix

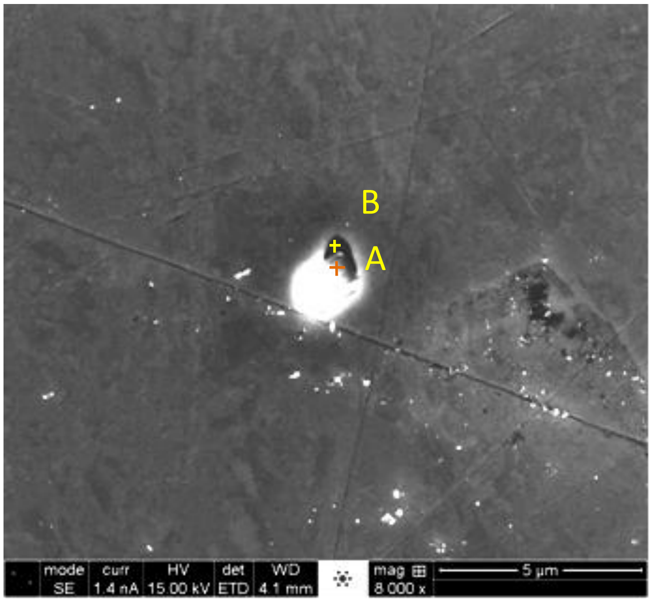
B
A
mode SE
curr 1.4 nA
HV 15.00 kV
det ETD
WD 4.1 mm
mag 8 000 x
5 μm

Wt%	Al_2O_3	MgO	MnS	CaO	SiO_2
A	85.0	11.9	1.2	1.8	-.-
B	35.3	2.7	51.5	5.7	4.7

a) b)

Figure 3.31. Centrifugally cast steel sample from the final product (X=0.5) of Heat E (0.139 *%Ca*) revealing *MgO-*Al_2O_3 and Al_2O_3*-MnS* inclusions in a steel matrix

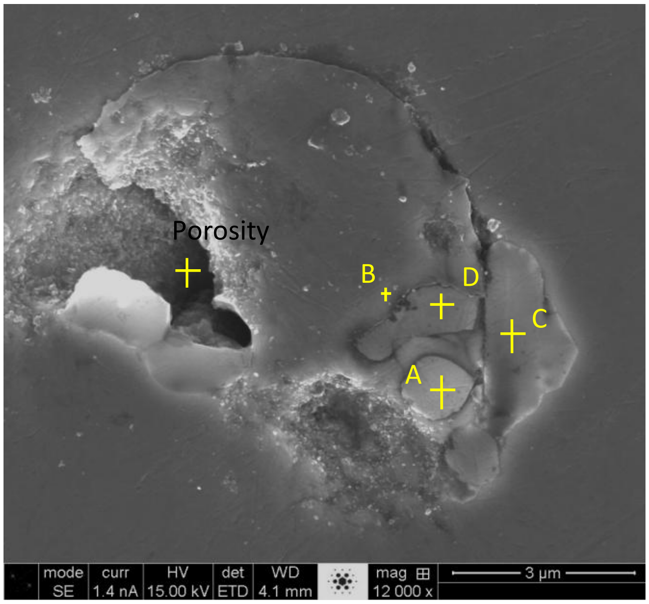
Porosity
B
D
C
A
mode SE
curr 1.4 nA
HV 15.00 kV
det ETD
WD 4.1 mm
mag 12 000 x
3 μm

Wt%	Al_2O_3	MgO	MnS	CaO	SiO_2
A	74.1	16.5	0.3	9.1	-.-
B	82.3	9.5	3.8	1.9	2.4
C	64.9	23.2	7.6	4.1	-.-
D	87.5	8.3	2.2	2.0	-.-

a) b)

Figure 3.32. Centrifugally cast steel sample from the final product (X=0.5) of Heat E (0.139 *%Ca*) exhibiting a ring of *MgO-*Al_2O_3 inclusions in the former boundary of a bubble-shaped cavity

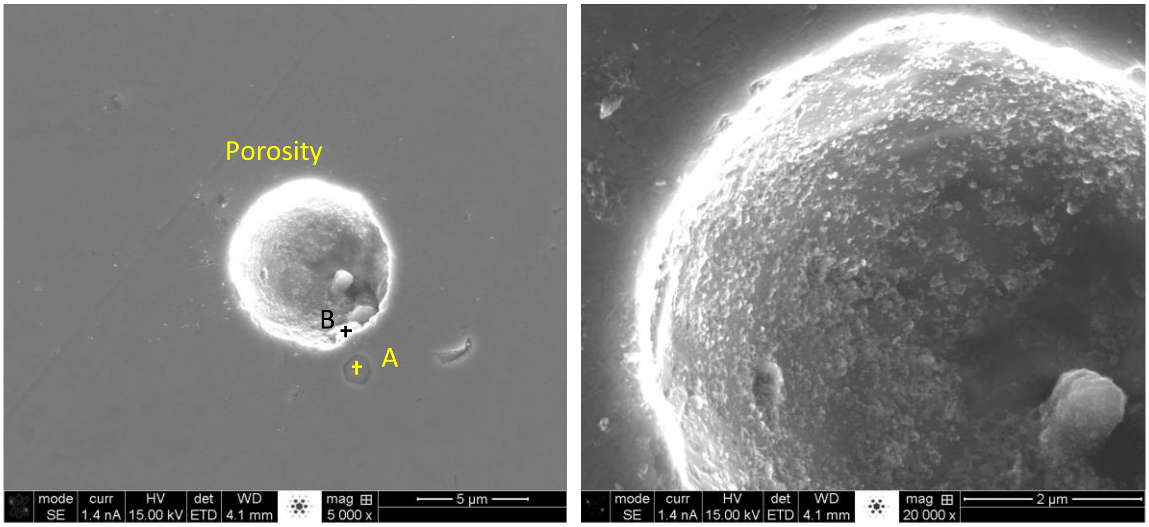
Porosity
B
A
mode SE
curr 1.4 nA
HV 15.00 kV
det ETD
WD 4.1 mm
mag 5 000 x
5 µm
mode SE
curr 1.4 nA
HV 15.00 kV
det ETD
WD 4.1 mm
mag 20 000 x
2 µm

a) b)

Wt%	Al_2O_3	MgO	SiO_2	CaO
A	85.3	14.0	0.7	-.-
B	99.0	-.-	-.-	1.0

c)

Figure 3.33. Centrifugally cast steel sample from the final product (X=0.5) of Heat E (0.139 *%Ca*) revealing *MgO-*Al_2O_3 and Al_2O_3 inclusions around the boundaries of a cavity in a steel matrix

4. DISCUSSION

The effectiveness of the calcium wire fed just prior to casting (heats A and B) and after AOD (heats D and E) was analyzed to determine its influence on inclusion removal in the centrifugally cast steel products. Non-metallic inclusions, like γ-aluminum oxynitrides (*Al-O-N*), were observed in the final product, in which their formation and stability were calculated using thermodynamics based on Dörner, Kaufman and Willems parameters. The inclusion flotation and entrapment in the centrifugally cast steel products were also evaluated using the Computational Fluid Dynamics (CFD) simulations, which were previously developed by several researchers at Missouri S&T.

4.1 EFFECTIVENESS OF CALCIUM RETENTION IN LIQUID STEEL

The effectiveness of calcium retention was calculated using the external pressure and vapor pressure of calcium in the liquid state. The external pressure of the molten steel surrounding the calcium wire is given by Eq. 22,

$$P = \rho g h + 101{,}325 \tag{22}$$

where, ρ is the density of the molten steel in kg/m^3 (7230 kg/m^3), g is gravity in m/s^2 and h is the calcium injection depth in m [9].

The external pressure is equal to the vapor pressure of the calcium wire at its boiling temperature [9]. The vapor pressure of calcium in the liquid state is described in Eq. 23,

$$\log P = 9.67 - \frac{8190}{T} \tag{23}$$

where, pressure (P) is in Pascal (Pa) and temperature (T) is in Kelvin (K) [45].

The boiling point of calcium is 2701 ºF (1483 ºC) at atmospheric pressure [45]. The metal depth in the ladle was around 66 in (1.7 m) for each experimental heat, as provided by the participating industry foundry. The calcium injection depth was around 20 in (0.5 m) based on the maximum calcium injection rate (17 ft/ min, 0.09 m/s) from the P.C. Campana micro wire-feeder and the total time to melt the calcium wire in the molten steel (5 s).

Figure 4.1 shows that the boiling point of the calcium wire is increased by a higher external pressure, allowing it to be injected deep in the ladle before the *Ca* begins to vaporize. In the industrial practice, the boiling point of calcium at an injection depth of 20 in was around 2791 °F (1533 °C) for each experimental heat. This implies that partial *Ca*-powder vaporization occurred at higher molten steel temperatures, especially for heats D and E. The molten steel temperatures in which the calcium was fed in the ladle after the final additions in AOD for heats D and E (2940 °F, 1616 °C) were higher than just prior to casting for heats B and C (2850 °F, 1566 °C). The calcium wire in Heats D and E should have been injected deeper in the ladle (63 in, 1.6 m), using a new cored wire feeder with a more efficient power supply to prevent *Ca* powder vaporization. The assumption of total *Ca*-powder vaporization was null because calcium aluminates were formed from the calcium remained in the molten steel (Figure 3.1 in Section 3.1).

The efficiency factor of calcium retention (E_r) in liquid steel is given by Eq. 24 (Table 4.1) [26],

$$E_r = \frac{w_{OS} + w_{sol}}{W} \tag{24}$$

where, w_{OS} entails the *%Ca* combined in non-metallic inclusions obtained from Aspex and the density of inclusions containing calcium (ρ), w_{sol} is the *%Ca* in the ladle after calcium treatment, and W is the *%Ca* injected in the ladle [26]. The ladle size for each experimental heat was also used to calculate w_{OS}, w_{sol} and W.

The efficiency factor of calcium retention in heats D and E ($E_{r,\ average}$= 0.01855) was lower than heat B (E_r= 0.0337) due to the difference of molten steel temperatures between the calcium treated heats, inducing partial *Ca*-powder vaporization in the ladle. The partial *Ca*-powder vaporization would have decreased the effectiveness of inclusion modification and removal in the molten steel. However, all the heats had very low recoveries of calcium, indicating high levels of re-oxidation during casting, minimizing the probability of calcium enhancement of steel quality.

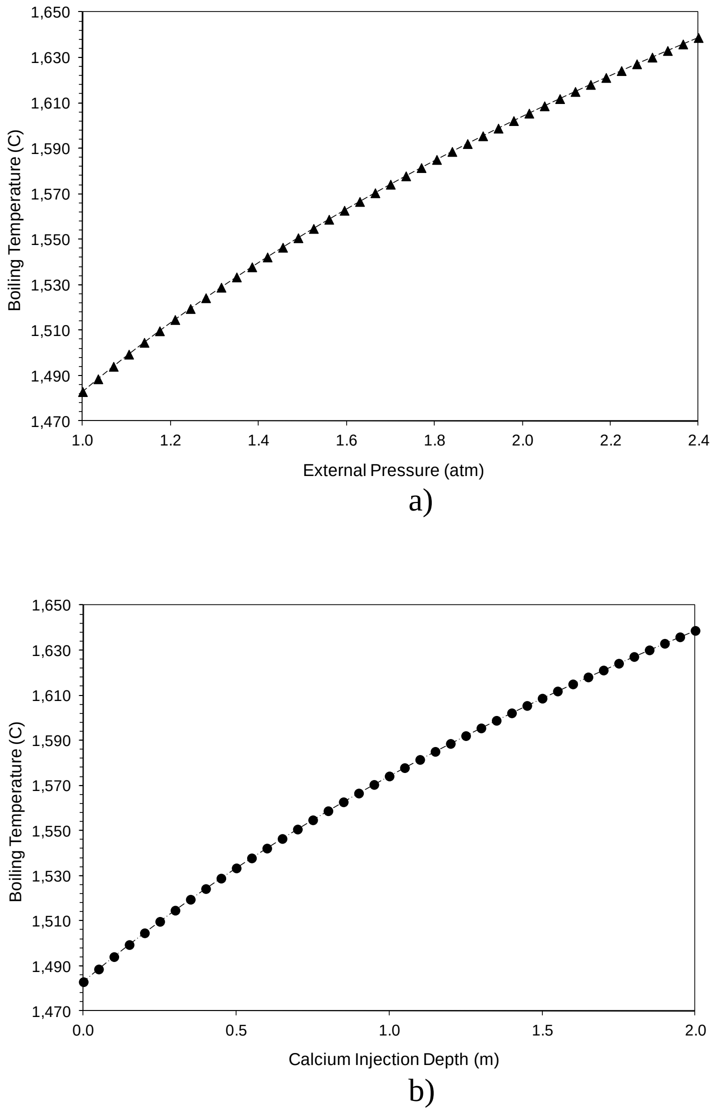

Figure 4.1. The variation of the boiling point of calcium with a) the external pressure and b) the depth of the wire in the molten steel

Table 4.1. Temperature prior to *Ca*-wire ladle treatment and efficiency factor (E_r) of calcium retention for each experimental heat

Heat	Aim %*Ca* added	Temperature Before *Ca* Wire (°F)	w_{os} (%*Ca* $_{inclusions}$ *Ladle Size/ $\rho_{inclusions}$)	w_{sol} (*%*Ca* * Ladle Size)	W (Aim %*Ca* added * Ladle Size)	$E_r = (w_{os} + w_{sol})/W$
B	0.014	2840	0.0002	0.04	1.1	0.034
C	0.077	2860	N/A	N/A	N/A	N/A
D	0.096	2914	0.0025	0.26	8.1	0.032
E	0.139	2965	0.0004	0.06	11.3	0.005

* The %*Ca* after calcium treatment was obtained in an industrial laboratory using an arc spectrometer

4.2 THERMODYNAMICS OF CALCIUM WIRE LADLE TREATMENT

The purpose of the calcium added to the ladle was to form low melting point calcium aluminates without the formation of high melting point CaO and CaS that could minimize the effectiveness of the calcium wire ladle treatment on the cleanliness of the molten steel. Figure 4.2 shows the transition from the low melting point calcium aluminates to the high melting point CaO and CaS inclusions at 2912 °F (1600 °C), using the commercial software FactSage. The thermodynamic simulations were based on the chemical composition for low alloy steels after the final additions in AOD; the dissolved $\%Al$ and Al_2O_3 were around 0.049% and 0.011%, respectively (Table 2.1 in Section 2.1). The dissolved $\%Ca$ was calculated using a variable amount of calcium, known as alpha <A>, which was between 0 and 0.06%. Two types of boundary conditions were considered: open top, allowing the reaction between the free radicals in the molten steel and the environment during ladle transfer operations; and partially isolated, assuming a uniform thick slag layer in the ladle.

The thermodynamic parameters entailed the Gibbs free energy of formation of calcium aluminate, [$\%Al$] and [$\%S$] given by Eqs. 25, 26 and 27 [46].

$$12CaS + 7(CaO\bullet 6Al_2O_3) \rightarrow 19(CaO\bullet 2Al_2O_3) + 8Al + 12S \tag{25}$$

$$3CaS + 4(CaO\bullet 2Al_2O_3) \rightarrow 7(CaO\bullet Al_2O_3) + 2Al + 3S \tag{26}$$

$$15CaS + 33(CaO\bullet 6Al_2O_3) \rightarrow 4(12CaO\bullet 7Al_2O_3) + 10Al + 15S \tag{27}$$

The thermodynamic calculations reveal that the dissolved calcium in the ladle for low alloy steels must be between 0.006 and 0.03% to form low melting point calcium aluminates. If the dissolved calcium in the ladle would have been above 0.03%, CaO and CaS inclusions would have formed in steel. The low sulfur content after final additions in AOD (0.001 $\%S$) significantly decreased the probability of CaS formation.

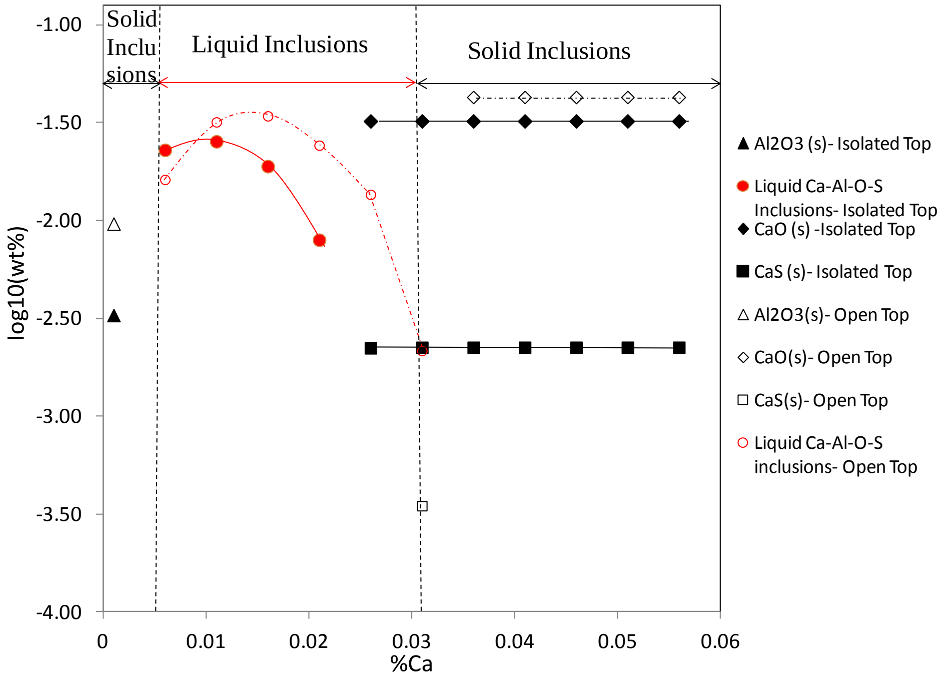

Figure 4.2. Thermodynamic analysis showing the relationship between the dissolved %*Ca* and the calcium-modified inclusions (Liquid *Ca-Al-O-S*, *CaO* and *CaS*) under different boundary conditions (open and isolated top) at 2912° F (1600° C)

4.3 THERMODYNAMICS OF γ-ALUMINUM OXYNITRIDE (Al_7O_9N AND $Al_{23}O_{27}N_5$)

The main types of inclusions containing nitrogen in the final product for all heats are *Al-O-N* or γ-aluminum oxynitride. The formation and stability of γ-aluminum oxynitride (Alon) are based on the thermodynamic parameters of aluminum oxide and aluminum nitride by Dörner et al. and Kauffman. Dörner et al. and Kauffman suggested that Alon was unstable below 1873 °K (1600 °C) and decomposed into $\alpha\text{-}Al_2O_3$ and *AlN*. The Alon system is described in Eq. 28 [47].

$$(3/17)Al_2O_3 + (1/17)AlN = (1/17)Al_7O_9N \tag{28}$$

The Gibbs free energy of Alon formation calculated by Dörner *et al.* and Kauffman are based on Eq. 29 [47].

$$\Delta G_f^o(Al_7O_9N) = \Delta G_r^o + 3\Delta G_f^o(Al_2O_3) + \Delta G_f^o(AlN) \tag{29}$$

The ΔG_f^o of formation of aluminum oxide and aluminum nitride used by Dörner et al. are given in Eqs. 30 and 31 [47].

$$\Delta\, G_f^o\, (Al_2O_3) = -1{,}673{,}913.8 + 318.94\, T \tag{30}$$

$$\Delta\, G_f^o\, (AlN) = -325{,}854.1 + 114.99\, T \tag{31}$$

Kauffman calculated the ΔG_r^o using the lattice stability, solution and compound phase parameters in Eq. 32 [47].

$$\Delta\, G_r^o = -515 - 0.259T \tag{32}$$

The results of $\Delta G_f^o\, (Al_7O_9N)$ and ΔG_r^o based on Dörner *et al*. and Kauffman calculations are given by Eq. 33 [47].

$$\Delta G_f^o\, (Al_7O_9N) = -5{,}356{,}902.8 + 1{,}070.58T \tag{33}$$

Willems et al. estimated the defect structure of Alon. The crystal structure of Alon is spinel (*Fd3m*) with vacancies on the octahedral sites of the lattice. McCauley proposed that $Al_{23}O_{27}N_5$ has eight aluminum ions on the tetrahedral sites and fifteen on the octahedral site of the lattice. The Gibbs free energy of the $Al_{23}O_{27}N_5$ formation based on the dissolved elements in the molten steel is described in Eqs. 34 and 35 [47].

$$23Al + 13.5O_2 + 2.5N_2 = Al_{23}O_{27}N_5 \tag{34}$$

$$\Delta G_f^o\, (Al_{23}O_{27}N_5) = -16{,}467{,}302 + 3{,}324.111T \tag{35}$$

Figure 4.3 compares the predictions of equilibrium solubility product and experimental results of [$\%Al$] and [$\%N$] for AlN and Alon formation at 1873 ºK (1600 ºC) based on Eqs. 33, 35 and 36. Eq. 36 entails the pure solid AlN formation in liquid iron based on the interaction parameters and log K_{AlN} measured by different authors in Table 4.2 [48], [49].

$$AlN(\mathrm{s}) = Al + N \tag{36}$$

The Alon formation in Figure 4.3 also displays the unsaturated conditions ($[O] < [O]_{\mathrm{eq.}}$) within the system. This means, the calcium fed in the ladle prior to casting (Heats B and C) and after AOD (Heats D and E) minimized the dissolved oxygen content due to reaction of calcium with Al_2O_3 to form low melting point calcium aluminates (Eq. 18 in Section 1.3.2).

Table 4.2. Thermodynamic parameters of aluminum and nitrogen in liquid iron at 1873 ºK [48], [49]

Authors	e^{Al}_{Al}	e^{Al}_{N}	**log** K_{AlN}	**Temp. Range (K)**
W. Y. Kim *et al*.	111/T-0.016	-332.2/T+0.194	-16,560/T+7.4	1873-1973
Evans *et al*.	0.043[5)]	828/T-0.471	-13,000/T+5.58	1873-2023
Wada *et al*.	0.043[5)]	744/T-0.421	-12,900/T+5.62	1823-1973

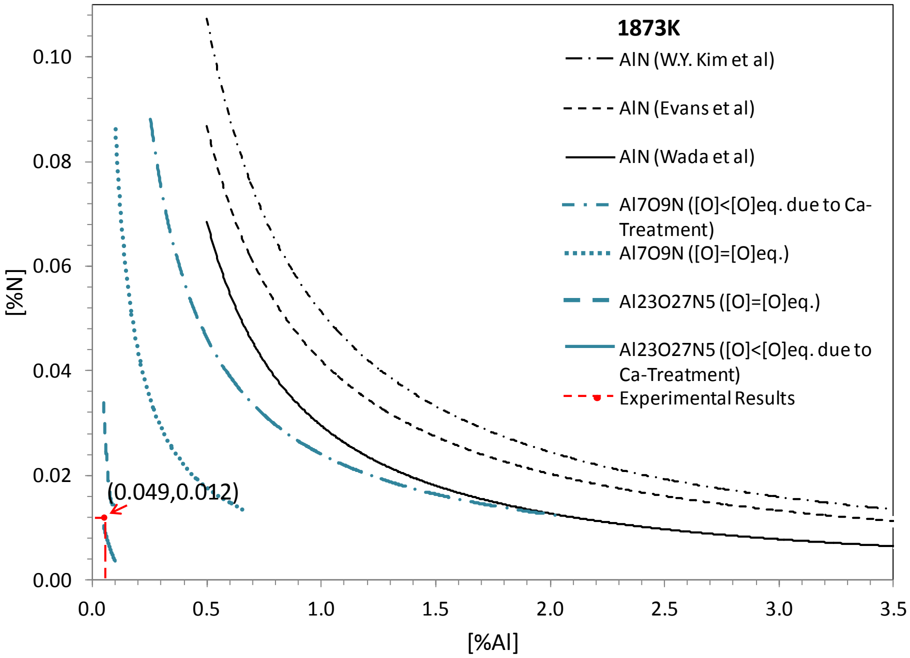

Figure 4.3. Equilibrium ([O]=[O]$_{eq.}$) and unsaturated ([O] < [O]$_{eq.}$) relations between [%Al] and [%N] at which AlN and Alon (Al_7O_9N and $Al_{23}O_{27}N_5$) are formed at 1873 ºK

The experimental results in Figure 4.3 are based on the average dissolved [%N] and [%Al] in the final product of the centrifugally cast steel samples. The dissolved [%N] and [%Al] were calculated using the total [%N] obtained from the Leco TC 500 oxygen-nitrogen analyzer and the total [%Al] measured by the arc spectrometer. The area covered by inclusions containing aluminum and nitrogen from the Aspex PICA 1020, as well as their elemental composition from the AFA data, were also used to determine the dissolved [%N] and [%Al] in the casting. The average dissolved [%Al] and [%N] in the final product of the centrifugally cast steel products are 0.049 and 0.012, respectively.

Figure 4.3 shows that the experimental results of the centrifugally cast steel products were in good agreement with the calculated Al_7O_9N under unsaturated conditions ($[O] < [O]_{eq.}$). $Al_{23}O_{27}N_5$ under both equilibrium ($[O] = [O]_{eq.}$) and unsaturated ($[O] < [O]_{eq.}$) conditions, as well as Al_7O_9N ($[O] < [O]_{eq.}$) under equilibrium conditions did not form due to the fact that a critical nitrogen content (0.015>[%N]) was required within the system (Figure 4.4). Similarly, a critical aluminum content in the liquid iron (0.5>[%Al]) must be exceeded to form aluminum nitrides in the centrifugally cast steel products [48].

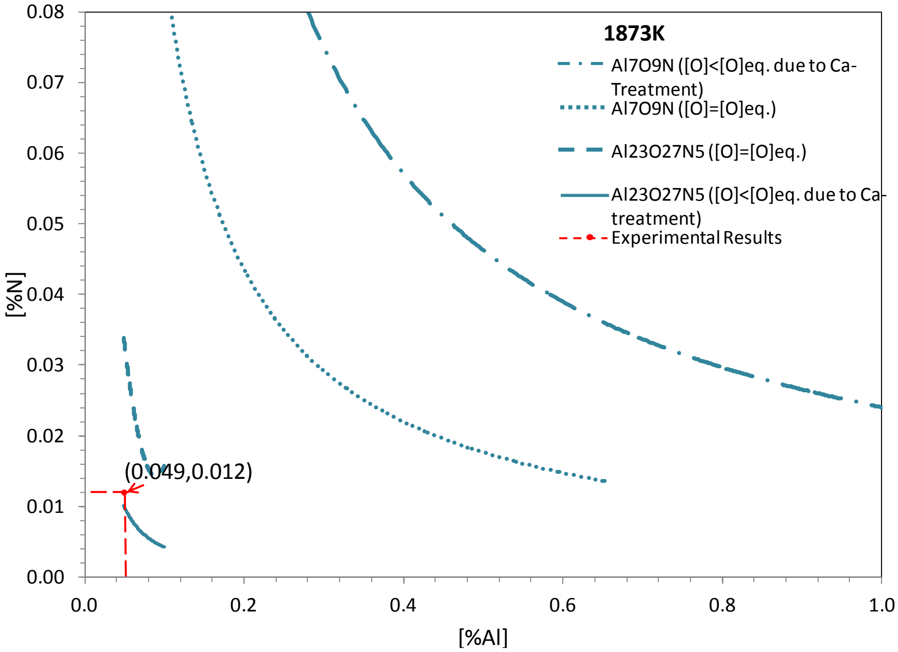

Figure 4.4. Equilibrium ($[O]=[O]_{eq.}$) and unsaturated ($[O] < [O]_{eq.}$) relations between [%Al] and [%N] at which Alon (Al_7O_9N and $Al_{23}O_{27}N_5$) is formed at 1873 ºK

4.4. NON-METALLIC INCLUSION FLOTATION AND ENTRAPMENT USING DIFFERENT MODELS FOR CENTRIFUGAL CASTING

Researchers from Missouri S&T developed different models to simulate the flotation and entrapment of non-metallic inclusions in centrifugal casting using two- and three-dimensional geometries in Computational Fluid Dynamics (CFD).

a) Model 1: S. Lekakh developed a two-dimensional CFD model to simulate the inclusion flotation throughout solidification kinetics and theoretical viscosity analysis on the centrifugally cast products. The CFD parameters included a steel wall thickness of 4 in (0.1 mm) and 1 in (0.03m) thick for both the steel mold and sand layer.

Figure 4.5 displays the relationship between solidification kinetics and the cooling time of the molten steel poured at 50 °C superheat. The solidification kinetics included the solidus (solid line) and liquidus (dashed line) regions, indicating unidirectional solidification from the OD with the development of a wide mushy zone in the casting. It was observed that the ID solidified last, which was in good agreement with the microstructural analysis due to the fact that shrinkage solidification was only found at this location for each experimental heat (Figure 3.20 in Section 3.4.1).

Figure 4.6 shows that the majority of inclusions could be removed from the main body of the casting if the steel temperature were above the liquidus. The inclusion removal was only possible for a short period of time. However, inclusion deceleration occurred due to a high viscosity in the mushy zone. The apparent viscosity of a heterogeneous system (μ_{ap}) relied on both the solid and liquid fraction in the mushy zone. If μ_{eff}>0.05 kg/m*s, a significant amount of non-metallic inclusions would not float to the ID. Instead, inclusion entrapment would occur in the main body of the casting and at the OD, which explained the large inclusion volume at the OD for the samples taken from the end of the finished tube for each experimental heat (Figure 3.4 in Section 3.2).

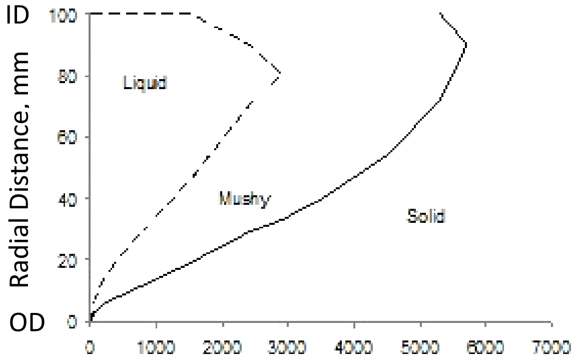

Figure 4.5. Solidification kinetics in a centrifugally cast tube using a wall thickness of 4 in (0.1 m)

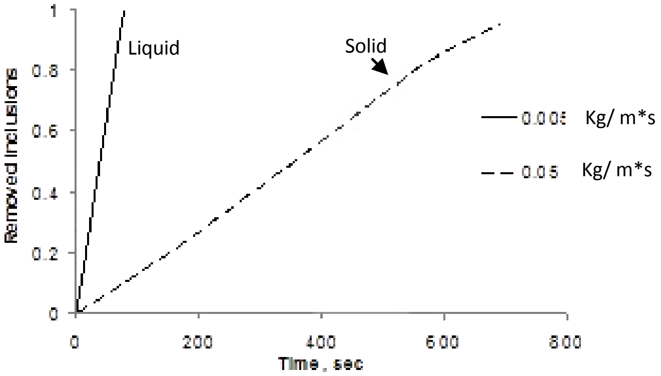

Figure 4.6. Effect of the apparent viscosity (μ=0.005 kg/m*s without solid fraction; μ_{ap}=0.05 kg/m*s with 25-30% solid fraction) on flotation dynamics using an inclusion diameter of 5μm at 100*G*

b) Model 2: L. Zhang simulated the inclusion entrapment under turbulent fluid flow using both the two- and three- dimensional CFD. The turbulent fluid is based on the continuity equation (Eq. 37) and the Navier-Stokes equations (Eqs. 38 and 39), which were previously validated in the submerged entry nozzle (SEN) and continuous casting simulations.

$$\frac{\partial(\rho u_j)}{\partial x_j} = 0 \tag{37}$$

$$\rho \frac{\partial(u_i u_j)}{\partial x_j} = -\frac{\partial p}{\partial x_i} + \frac{\partial}{\partial x_j}\left(\mu_{eff}\frac{\partial u_i}{\partial x_i}\right) + \frac{\partial}{\partial x_j}\left(\mu_{eff}\frac{\partial u_j}{\partial x_i}\right) + \rho g + \vec{F} \tag{38}$$

$$\mu_{eff} = \mu_o + \mu_t \tag{39}$$

where, ρ is density in Kg/m^3, u_j is the velocity of a component in the x_j direction in m/s, and x_j is the direction of a component along different axis in m. In the Navier-Stokes equations, p is pressure in Pascal, $\vec{F}$ is a momentum in N, and μ_{eff} is the turbulence-adjusted effective viscosity in Kg/m. The effective viscosity (μ_{eff}) entails the laminar fluid viscosity (μ_O) and the turbulent fluid viscosity (μ_t).

The three-dimensional volume of fluid (VOF) multiphase model was utilized to analyze the interaction between the molten steel and the air by simultaneously solving the heat transfer in the casting mold. The solidification front growth model simulated the liquid faction, β, in the mushy zone during the solidification process, which was assumed to be a porous zone in the model. In the porous zone, a momentum loss, S, was supposed to take place when the liquid phase became solid, and was given by Eq. 40,

$$S = \frac{(1-\beta)^2}{(\beta^3 + 0.001)} A_{mush} \bullet \phi \tag{40}$$

where, A_{mush} is the constant mushy zone and ϕ is a variable related to the fluid properties, like velocity and turbulence.

The user defined function (UDF) was employed for the liquid fraction, β, in the mushy zone. If β=1, steel was then fully in the liquid state. If β<1, x-velocity and y-velocity were then fixed using Eqs. 41 and 42,

$$v_x = -r\omega \sin\alpha \tag{41}$$

$$v_y = r\varpi \cos\alpha \tag{42}$$

where, r is the distance to any point within centrifugal casting, ω is the angular velocity, and α (alpha) is the coordinate direction angle.

The parameters and dimensions that were used in Zhang's model are shown in Table 4.3. The CFD parameters included the experimental data, consisting of a rotation speed of 850 rpm and a pouring/ initial temperature of 1853 °K (1580°C, 2876 °F). The computation quality was enhanced using a mesh with an entire domain of 663, 680 cells during the centrifugal casting simulations.

Table 4.3. Dimensions and parameters for CFD modeling

Parameter	**Value**	**Parameter**	**Value**
Mold length	16 m	Viscosity of liquid	0.0067
Mold radius	0.212m	Density of liquid steel	7020 kg/m^3
Mold inlet radius	6 cm	Thermal expansion coefficient	1×10^{-4} 1/K
Rotation speed	1000 rpm	Density of inclusion	5000 kg/m^3
Inlet velocity	1.915 m/min	Latent heat	270000 J/kg
Turbulent energy	0.00001	Initial temperature	1853 K
Dissipation rate	0.00001	Liquidus temperature	1803.15 K
Pouring time	10 s	Solidus temperature	1763.15 K
Latent heat	270000 J/kg	Thermal conductive	34 w/m·k
Rotation speed of the mold	**850 rpm**		

Figure 4.7 shows a) the air-steel interface during pouring and b) the temperature distribution at 19 s after pouring, using the three-dimensional VOF computation. It was observed that the lowest temperature distribution in the centrifugally cast product was located at the non-pouring end of the finished tube, showing a good agreement with both the experimental data and Mirzoyan and Pavperova results (Figure 1.10 in Section 1.2.1.3).

Figure 4.8 compares the inclusion entrapment using two separate CFD runs with different inclusion sizes: a) the first run included 5 μm inclusions; and b) the second run entailed 50 μm inclusions. These simulations were performed using a two-dimensional computation due to the fact that the three-dimensional simulation typically takes very long time (around two to three months) to achieve the final results. In the two dimensional computation, a total of 50,000 inclusions with a density of 5,000 kg/m^3 were randomly distributed in the liquid phase. As boundary conditions, inclusion entrapment was assumed to take place when the liquid fraction, β, was around 0.3. Larger inclusions (>50 μm) are prone to be closer to the ID due to the fact that the centrifugal forces acting on the larger inclusions are greater than those on the smaller inclusions (<5 μm). The smaller inclusions are more dispersed along the radial direction of the centrifugally cast product. Figure 4.8 also exhibits that the highest concentration of inclusions regardless of the inclusion size is at the ID. However, the CFD simulations differed from the experimental results due to the fact that the snapshots in Figure 4.8 were taken from the middle of the finished tube, while the experimental centrifugally cast products were taken from the opposite pouring end of the finished tube. This implies that the inclusion flotation could be enhanced at the middle of the casting because the steel temperature at the pouring end was significantly higher than the opposite pouring end of the finished tube, allowing inclusions to overcome the viscosity of the steel to float to the ID. In contrast, the lower steel temperatures at the non-pouring end produce rapid solidification of the casting, minimizing considerably the liquid fraction in the mushy zone in a short period of time. Inclusion entrapment is then observed, especially at the OD, reducing the effect of centrifugal forces on inclusion flotation in a fully developed solid fraction (β<0.3).

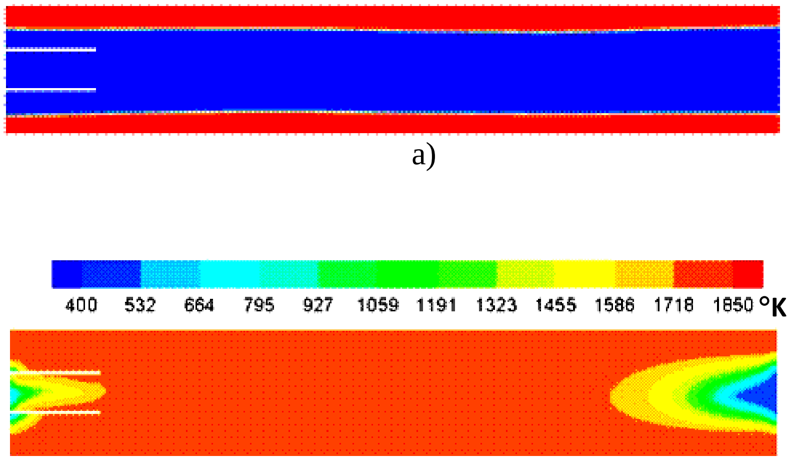

a)

b)

Figure 4.7. Comparison of a) the air-steel interface during pouring and b) the temperature distribution at 19 s after pouring, using the three-dimensional CFD computation

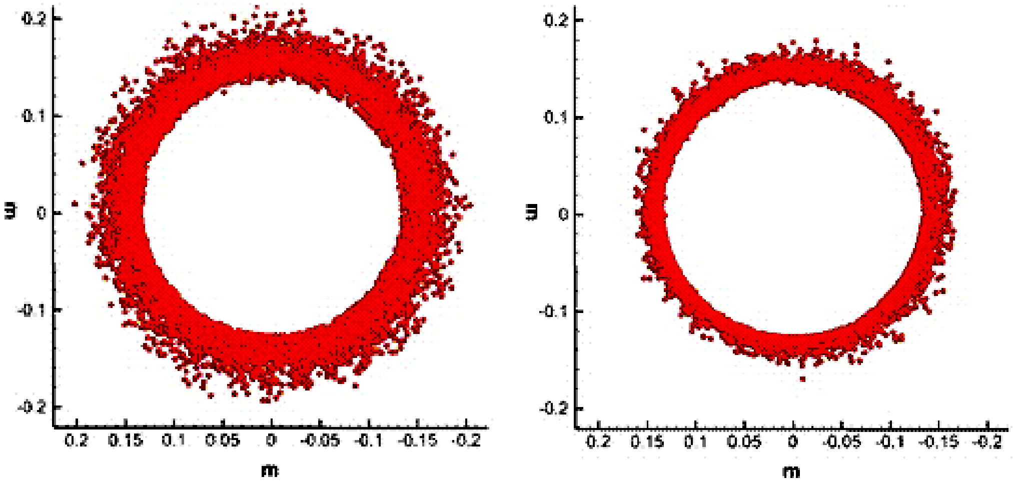

a) b)

Figure 4.8. Comparison of inclusion final entrapment using particle size diameters between a) 5 µm and b) 50 µm in the solidified centrifugal tube at a rotation speed of 850 rpm, using the two-dimensional CFD computation

4.5. COMPARISON OF NON-METALLIC INCLUSION DISTRIBUTION IN STATIC AND CENTRIFUGAL CASTING

The amount and spacing between inclusions, as well as porosity, in the regular melting practice and calcium treated heats in static casting were compared to the final product (average of the three samples at x=0.25, x=0.50 and x=0.75) of the centrifugally cast steel tubes. In previous research, static casting was used to analyze the effects of calcium treatment and *Ar*-stirring on inclusions in medium carbon steel (0.3 %*C*, 0.8 %*Mn*, 0.01 %*P*, 0.02 %*S*, 0.5 %*Si*, 0.05 %*Cr*, 0.2 %*Mo* and 0.09 %*Al*). Figure 4.9 reveals that the amount of non-metallic inclusions regardless of calcium addition in centrifugal casting was considerably less than that in static casting. Figure 4.10 shows that the inclusion spacing in the final product was significantly larger than static casting, implying that cleaner steel is produced in centrifugal casting rather than static casting. Note that the amount of inclusions in static casting decreased by higher calcium additions, but it was insufficient to overcome the benefits of large centrifugal forces in centrifugal casting.

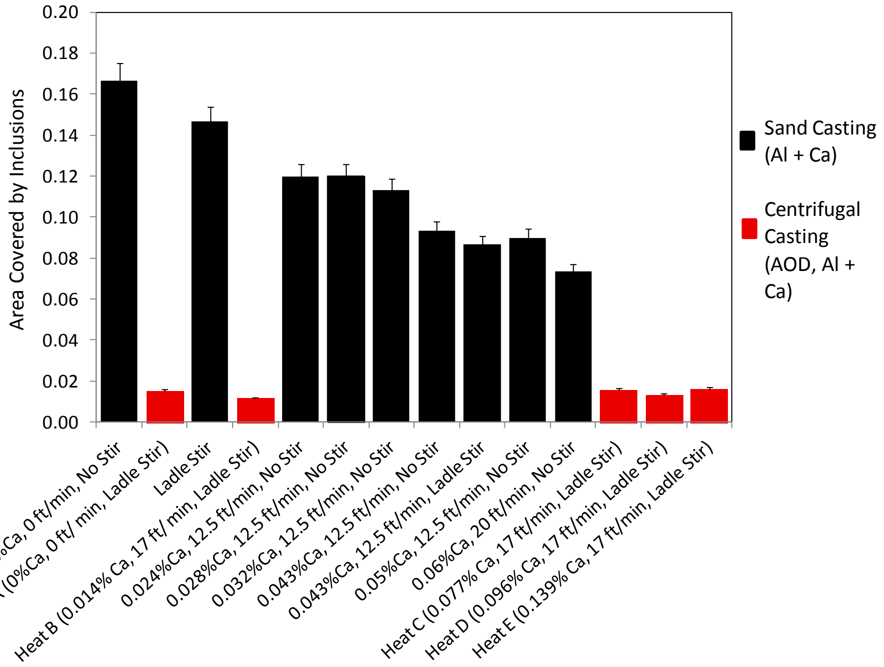

Figure 4.9. Comparison of the area covered by inclusions in samples taken from the cast keel blocks in sand casting and the final product of the centrifugally cast steel products with different amounts and speeds of calcium wire injection in the ladle

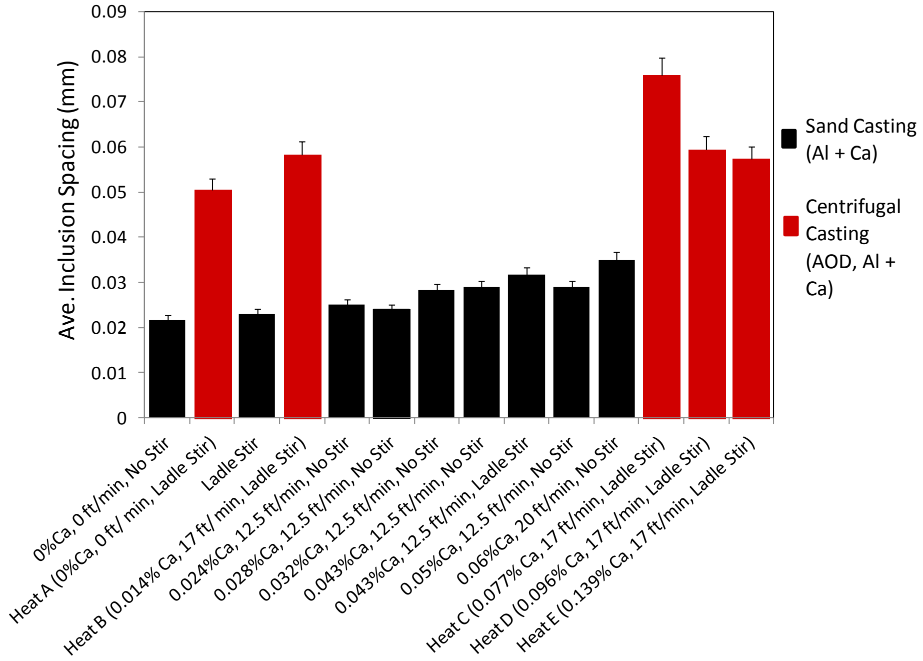

Figure 4.10. Comparison of the inclusion spacing in samples taken from the cast keel blocks in sand casting and the final product of the centrifugally cast steel products with different amounts and speeds of calcium wire injection in the ladle

Figure 4.11 compares the porosity in static casting using the cast and HIPed (Hot Isostatic Pressure) conditions of Eglin steel (ES-1: 0.3 %*C*, 0.7 %*Mn*, 1 %*Si*, 2.6 %*Cr*, 1.1 %*Ni*, 0.4 %*Mo*, 0.1 %*V* and 1 % *W*) to the final product of the centrifugally cast tubes. The porosity in static casting, which was not treated by HIP, was significantly larger than centrifugal casting. This means, that the large pressure in centrifugal casting minimizes the probability of gas pore formation in comparison to static casting. The porosity in static casting can be improved to be more similar to centrifugal casting by increasing the temperature and isostatic gas pressure in a high pressure vessel during the HIP process.

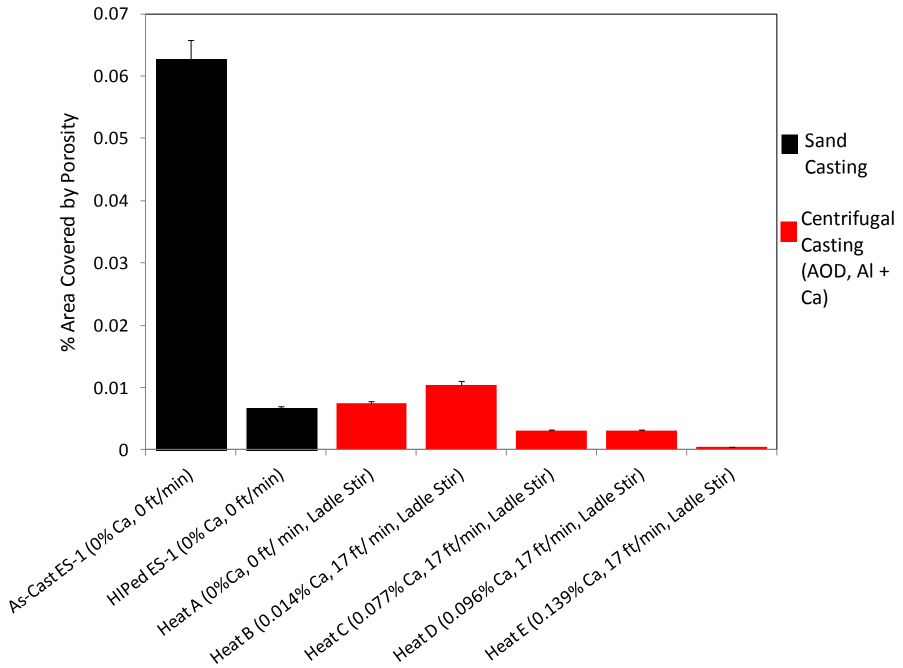

Figure 4.11. Comparison of porosity in samples taken from both the cast and HIPed Eglin steel (ES-1) in static casting, as well as the final product of the centrifugally cast steel products with different amounts and speeds of calcium wire injection in the ladle

5. CONCLUSIONS

Calcium wire fed just prior to casting and at earlier stages of the ladle treatment (just after AOD) did not significantly modify or reduce the number, size or shape of inclusions containing aluminum due to the amount of re-oxidation during pouring and the melt transport through the pouring basin. The amount and shape of inclusions containing sulfur were slightly reduced in the final product, but it was insufficient to improve the toughness of the centrifugally cast products. However, the centrifugal forces decrease the amount of non-metallic inclusions in the final product, enhancing its cleanliness by concentrating the majority of inclusions either at the ID (inclusion flotation) or OD (inclusion entrapment), which are typically removed through machining and not incorporated in the final product. This research reveals that cleaner steel, which consists of the least number of inclusions and the largest inclusion spacing, is produced in centrifugal casting versus static casting. In centrifugal casting, porosity is also minimized when compared to static casting without HIP (Hot Isostatic Pressing).

The porosity and cleanliness of the centrifugal cast steel can be further improved by modifying some casting techniques, such as the pouring temperature. Excessive pouring temperatures produce slow solidification from the OD to the ID, providing the worst conditions for the formation of deep shrinkage cavities. The turbulence in the pouring basin can be reduced by pouring the molten steel slowly, minimizing the interaction of the molten steel with the environment. Hot Isostatic Pressing (HIP) can be used to reduce porosity and improve the mechanical properties of the centrifugally cast steel products.

APPENDIX

VISUAL BASIC CODE FOR CALCULATING PARTICLE SPACING

```
Sub MinDist()                                               'Find the average minimum distance between particles
        Sheets(1).Activate 'activate sheet 1
        Cells(1, 1).Activate 'activate cell A1

        counter = 0

        Totalmin = 0

        Do 'change between particles
            If ActiveCell.Offset(1 + counter, 2) = "" Then                          'read particle location
                Exit Do                                               'if the next cell is empty stop the loop
             Else

                x = ActiveCell.Offset(1 + counter, 3).Value
                y = ActiveCell.Offset(1 + counter, 4).Value

            End If

            comparecounter = 0 'reset the compare counter
            mindistance = 0 'reset the minimum distance
            Do                                                         'change between compared particles
                If ActiveCell.Offset(1 + comparecounter, 2) = "" Then           'read compared particle location
                      Exit Do                                         'if the next cell is empty stop the loop
                Else

                      xC = ActiveCell.Offset(1 + comparecounter, 3).Value
                      yC = ActiveCell.Offset(1 + comparecounter, 4).Value

                End If
                 compareddistance = (((x - xC) ^ 2 + (y - yC) ^ 2)) ^ 0.5        'calculate distance between particles

                If mindistance = 0 Then                                  'the first distance must be the smallest
                      mindistance = compareddistance
                      minparticle = comparecounter + 1

                 ElseIf compareddistance = 0 Then        'the distance between a particle and itself should not be counted
                 ElseIf compareddistance < mindistance Then      'if the new distance is smaller it   becomes the min distance
                      mindistance = compareddistance
                      minparticle = comparecounter + 1

                End If
                 ActiveCell.Offset(1 + counter, 5).Value = minparticle                 'print the closest particle

                 ActiveCell.Offset(1 + counter, 6).Value = mindistance       'print the distance of the closest particle
                comparecounter = comparecounter + 1                                   'compare the next particle

            Loop
            Totalmin = (Totalmin + mindistance)                              'add all of the total of all min distances
            ActiveCell.Offset(0, 1).Value = Totalmin / (comparecounter)             'print the average min distance
            counter = counter + 1                                                         'move to next particle
        Loop
End Sub
```

BIBLIOGRAPHY

[1] N. Janco, "Centrifugal casting," American Foundry Society, 1988

[2] P.S. Siva-Raju and S.P. Mehrotra, "Mathematical modeling of centrifugal casting of metal matrix composites," Materials transactions, *JIM,* Vol. 41, No. 12, pp. 1626-1635, 2000

[3] T.S. Piwonka, "Casting," In J.R. Davis (Ed.) Metals handbook, ASM International, pp. 749-750, 1998

[4] V. Jiman, I. Ciobanu and S.I. Munteanu, "Particularities of the mathematical modeling of centrifugally cast part solidification," Metallurgia International, Vol. 14, No. 10, pp. 80-84, 2009

[5] H. Fu, Q. Xiao and J. Xing, "A study on the crack control of a high speed steel roll fabricated by a centrifugal casting technique," Materials science and engineering, 474, pp. 82-87, 2008

[6] K.S. Keerthiprasad, M.S. Murali, P.G. Mukunda and S. Majumdar, "Numerical simulation and cold modeling experiments on centrifugal casting," Metallurgical and materials transactions B, Vol. 42B, pp. 144- 155, 2011

[7] N. Song, S. Wu, X. Kang and D. Li, "Hydraulic experiments of mold filling process in horizontal centrifugal casting," Advanced materials research, Vols. 154-155, 2011

[8] ASM Handbook, "Failure analysis and prevention," Vol. 11, ASM International: Materials Park, OH, 2007

[9] V. Singh, "Inclusion modification in steel castings using automated inclusion analysis," M.S Thesis, Missouri University of Science and Technology, 2009

[10] H. Fu, Q. Xiao and J Xing, "A study of segregation mechanism in centrifugal cast high speed steel rolls," Materials science and engineering, 479, pp. 253-260, 2008

[11] A. Velhinho and L.A. Rocha, "Longitudinal centrifugal casting of metal-matrix functionally grades composites: an assessment of modeling issues," Journal of Materials Science, Vol. 46, 2011

[12] L. Zhang, J. Aoki and B.G. Thomas, "Inclusion removal by bubble flotation in a continuous casting mold," Metallurgical and Materials Transactions B, Vol. 37B, PP. 361-379, 2006

[13] Y.A. Cengel and R.H. Turner, "Fundamentals of thermal-fluid sciences," 2nd ed., McGraw Hill, 2005

[14] E.Y. Martinez, K.D. Peaslee and S.N. Lekakh, “Calcium wire ladle treatment to improve cleanliness of centrifugally cast steel,” *AFS* Transactions, Vol. 119, paper 11-037, 2011

[15] L. Zhang and B. G. Thomas, “State of the art in control of inclusions during steel ingot casting,” Metallurgical and Materials Transactions B, Vol. 37B, pp. 733-761, 2006

[16] J. Campbell, “Castings,” 2nd ed., Elsevier Butterworth-Heinemann, 2003

[17] B. Katavić and Z. Odanović, “Analysis of non-metallic inclusions distribution and microstructure in centrifugally cast steel pipes,” 3rd International conference deformation processing and structure of materials, Belgrade, Serbia, 2007

[18] G.S. Mirzoyan and I.A. Pavperova, “Non-metallic inclusion distribution in centrifugal semi-finished tubes,” Central scientific-research institute for mechanical engineering scientific and production union, No. 2, pp. 59-60, 1988

[19] J.H. Spurk, “Fluid mechanics: problems and solutions,” Springer- Verlag Berlin Heidelberg, 1997

[20] G. Lesoult, “Microporosity in cast alloys: simple considerations on its formation,” International journal of cast metals research, Vol. 22, pp. 2-7, 2009

[21] T.K. Vaidyanathan, A. Schulman, J.P. Nielsen and S. Shalita, “Correlation between macrosccopic porosity location and liquid metal pressure in centrifugal casting technique,” SAGE, pp. 59-66, 1981

[22] E. Spetzler and J. Wendorff, “Injecting alkaline earth into steel melts and its effect on steel products,” 58th National open hearth and basic oxygen steel conference proceedings, pp. 358-377, 1975

[23] E.J. Dunn Jr., “Calcium treatment of steel: from tap stream to wire to log,” Electric furnace conference proceedings, pp. 125-137, 1988

[24] D. W. P. Lynch and J.W. Robison, Jr., “Calcium wire ladle treatment: Cleanliness and ductility improvement of foundry steel,” pp. 303-311, 1983

[25] E. Vachiery, “Welcoming address: advent of cored wire injection for in-ladle metallurgy,” Calcium treatment symposium, The Institute of Metals, pp. 1-2, 1988

[26] E.T Turkdogan, “Metallurgical consequences of calcium retention in liquid and solid steel,” Proceedings of the first international calcium treatment symposium, The Institute of Metals: pp. 3-13, 1988

[27] E. Pellicani, B. Durand and A. Gueussier, “Guidelines for calcium treatment of steel and sate of calcium retained,” The institute of metals: proceedings of the first international calcium treatment symposium, pp. 15-22, 1988

[28] D.A. Dyudkin, and V.V. Kisilenko, “Modern technology for treating steel outside the furnace with cored wire,” Metallurgist, Vol. 51, No. 3, pp. 61-65, 2007

[29] V. Singh, S. Lekakh and K. Peaslee, “Using automated inclusion analysis for casting process improvements,” SFSA, pp. 1-18, 2008

[30] H. Suito and H. Ohta, “Characteristics of particle size distribution in early stage of deoxidation,” ISIJ International, Vol. 46, No. 1, pp. 33-41, 2006

[31] M. Jiang, X. Wang, B. Chen and W. Wang, “Laboratory study on evolution mechanisms of non-metallic inclusions in high strength alloyed steel refined by high basicity steel,” ISIJ International, Vol. 50, No. 1, pp. 95-104, 2010

[32] V. Singh, S. Lekakh and K. Peaslee, “Optimization of calcium treatment to improve cleanliness of cast steel,” Materials Science and Technology, pp. 1-12, 2009

[33] P. Degryse and J. Elsen, “Industrial minerals, resources, characteristics and applications,” Leuven University Press, 2003

[34] S.K. Choudhary and A. Ghosh, “Thermodynamic evaluation of formation of oxide-sulfide duplex inclusions in steel,” ISIJ International, Vol. 48, No. 11, pp. 1552-1559, 2008

[35] S.K. Choudhary and A. Ghosh, “Mathematical model for prediction of composition of inclusions formed during solidification of liquid steel,” ISIJ International, Vol. 49, No. 12, pp. 1819-1827, 2009

[36] J. Finardi, “Effect of calcium treatment of steel for castings,” *AFS* Transactions, Vol. 108, paper 00-09, pp. 409-417, 2000

[37] C. Blais, G. L’Esperance, H. LeHuy, and C. Forget, “Development of an integrated method for fully characterizing multiphase inclusions and its application to calcium-treated steels,” Elsevier, 38, pp. 25-37, 1997

[38] A. Binyam, “Principles and implementations of automated analysis,” Aspex Corporation, pp. 1-11, 2003

[39] Aspex, “Perception suite user documentation,” Aspex, LLC, Vol. 1.3, pp. 5

[40] L. E. Creasy, "A critical evaluation of line overlap corrections in x-ray spectrometry," JCPDS-International Centre for Diffraction Data, Vol. 44, pp. 361-367, 2001

[41] Z. Zhang, A. Tilliander, A. Karasev and P.G. Jonsson, "Simulation of the steel sampling process," ISIJ International, Vol. 50, No. 12, 2010

[42] R. E. Reed-Hill and R. Abbaschian, "Physical metallurgy principles," 3rd ed., PWS Publishing Company, 1994

[43] ASM Handbook, "Metallography and microstructures," Vol. 9, ASM International: Materials Park, OH, 1995

[44] L. Zhang, B. Rietow, B.G. Thomas and K. Eakin, "Large inclusions in plain-carbon steel ingots cast by bottom teeming," ISIJ International, Vol. 46, No. 5, pp. 670-679, 2006

[45] ASM Handbook, "*Properties of pure metals*," Properties and selection: non-ferrous alloys and special-purpose materials, 10th ed., Vol. 2, ASM International, pp. 1099-1201, 1990

[46] K. Larsen and R.J Fruehan, "Calcium modification of oxide inclusions," Trans. ISS, Iron and Steelmaker, Vol. 17, pp. 45-52, 1990

[47] H.X. Willems, M.M.R.M. Hendrix, R. Metselaar and G. de Width, "Thermodynamics of Alon I: Stability at lower temperatures," Journal of the European ceramic society, Vol. 10, pp. 327-337, 1992

[48] W.Y. Kim, J.G Kang, D.H. Park, J.B. Lee and J.J Pak, "Thermodynamics of aluminum, nitrogen and AlN formation in liquid iron," ISIJ International, Vol. 47, No. 7, pp. 945-954, 2007

[49] Y. Kang, M. Thunman, D. Sichen, T. Morohoshi, K. Mizukami and K. Morita, "Aluminum deoxidation equilibrium of molten iron- Aluminum alloy with wide aluminum composition range at 1873 ºK," ISIJ International, Vol. 49, No. 10, pp. 1483-1489, 2009

VITA

Edith Yolanda Martinez Silva received her primary and secondary education in Mexico. In May of 2008, she received her Bachelor’s degree in Materials and Metallurgical Engineering from the University of Texas at El Paso (UTEP). In December 2011, she received her Master’s of Science in Metallurgical Engineering from Missouri University of Science and Technology (Missouri S&T).